



Universiteit
Leiden
The Netherlands

Cavities for light and sound: a cavity-enhanced platform for quantum acoustics

Fisicaro, M.

Citation

Fisicaro, M. (2024, October 29). *Cavities for light and sound: a cavity-enhanced platform for quantum acoustics*. Retrieved from <https://hdl.handle.net/1887/4106853>

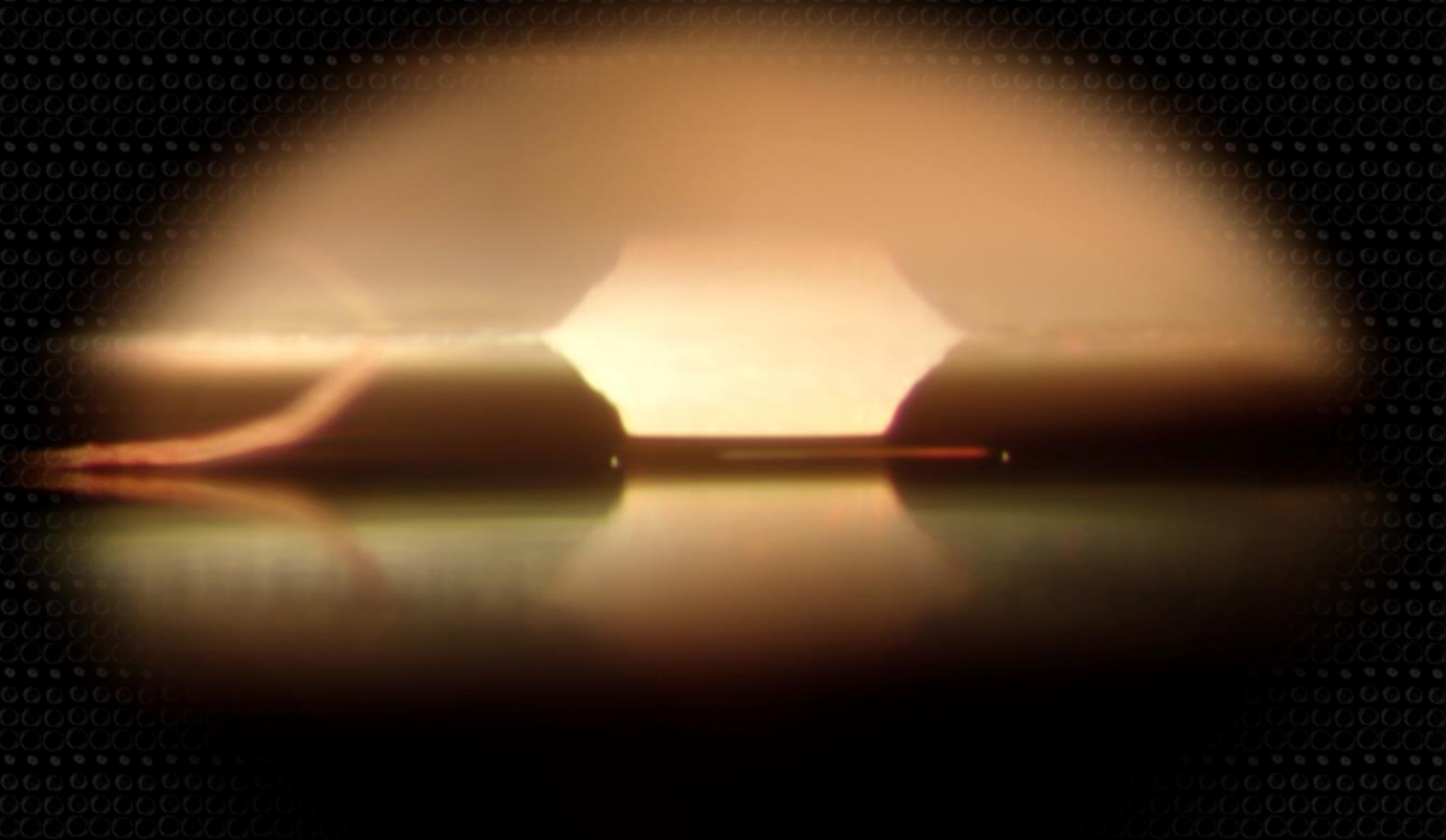
Version: Publisher's Version

License: [Licence agreement concerning inclusion of doctoral thesis in the Institutional Repository of the University of Leiden](#)

Downloaded from: <https://hdl.handle.net/1887/4106853>

Note: To cite this publication please use the final published version (if applicable).

Cavities for light and sound



A cavity-enhanced platform
for quantum acoustics

Matteo Fisicaro

**Cavities for light and sound:
A cavity-enhanced platform for quantum acoustics**

Proefschrift

ter verkrijging van
de graad van doctor aan de Universiteit Leiden,
op gezag van rector magnificus prof.dr.ir. H. Bijl,
volgens besluit van het college voor promoties
te verdedigen op dinsdag 29 oktober 2024
klokke 11:30 uur

door

Matteo Fiscaro

geboren te Villafranca di Verona (VR), Italië
in 1994

Promotor: Prof. dr. D. Bouwmeester

Co-promotor: Dr. W. Löffler

Promotiecommissie: Prof. dr. H. Krenner (Universität Münster, Germany)

Prof. dr. S. Groeblacher (Technische Universiteit Delft, Netherlands)

Dr. S.E. Henkes

Dr.ir. B.J. Hensen

Prof.dr. M.P. van Exter

Prof.dr.ir. S.J. van der Molen

An electronic version of this thesis can be found at <https://scholarlypublications.universiteitleiden.nl/>

The research project described in this thesis was conducted at the Leiden Institute of Physics, Leiden University. The project received funding from the European Union's Horizon 2020 research and innovation programme under grant agreement No. 862035 (QLUSTER) and by the Netherlands Organisation for Scientific Research (NWO/OCW), as part of the Frontiers of Nanoscience program (NanoFront), QUAKE (project number 680.92.18.04) and the Quantum Software Consortium (project number 024.003.037 / 3368).



Universiteit Leiden



Copyright © 2024 by Matteo Fiscaro

The front cover shows a side view of the open-access optical microcavity. At the top is the plinth that houses the concave micromirror array, and at the bottom is its reflection on the flat GaAs mirror. The rainbow line in the middle is caused by light diffracted from the metal grating of the surface acoustic wave cavity, which is fabricated on the flat GaAs mirror. The back cover shows an optical micrograph of the surface acoustic wave cavity, where the yellow color results from diffraction of white light off the metal grating of the acoustic mirrors.

Contents

1	Introduction	1
1.0.1	Generation of surface acoustic waves	2
1.0.2	Acoustic cavities and phonon confinement	3
1.0.3	QD interaction: optical microcavities	5
1.0.4	Thesis outline	6
2	Imaging transverse modes in surface acoustic wave cavities	9
2.1	Introduction	10
2.2	Experimental setup	11
2.2.1	SAW device	11
2.2.2	Fiber-based scanning Michelson interferometer	11
2.2.3	Heterodyne circuit	13
2.2.4	Voltage-displacement calibration	13
2.3	Imaging of transverse modes in a planar SAW cavity	14
2.4	Conclusions and outlook	19
2.5	Appendix	20
2.5.1	Effects of the beam spot size on the measured interferometric signal	20
2.5.2	Beam spot size measurement	23
3	Investigation of spurious bulk acoustic waves in surface acoustic wave devices by acoustic fringe analysis	25
3.1	Introduction	26
3.2	Interference of surface and bulk waves	27
3.3	Acoustic fringe analysis	29
3.3.1	Long SAW cavity	30
3.3.2	Short SAW cavity	32
3.3.3	Discussion	33
3.4	Conclusions and outlook	36
4	Observation of the optical Talbot effect from a surface acoustic wave dynamic grating	37
4.1	Introduction	38
4.2	Experimental setup	39
4.3	Amplitude and phase modulation	40
4.3.1	Complex collection ratio	41
4.3.2	Single-beam experiment: amplitude modulation	42
4.3.3	Two-beams experiment: phase modulation	42
4.3.4	Comparison to experiments	43
4.3.5	Explaining the periodicity: the Talbot effect	45
4.4	Conclusions and outlook	48
4.5	Appendix	49
4.5.1	The complex collection ratio	49

4.5.2	The Talbot effect	51
4.5.2.1	Existence and positions of the self images	53
5	Active stabilization of an open-access optical microcavity for low-noise operation in a standard closed-cycle cryostat	55
5.1	Introduction	56
5.2	Device design	56
5.3	Device characterization: feedback loop and mechanical resonances	59
5.3.1	Optical setup:	59
5.3.2	Cavity stabilization feedback loop	60
5.3.3	Identification of mechanical resonances	61
5.4	Stability at room temperature	62
5.5	Stability in a closed-cycle cryostat at 4 K	64
5.6	Conclusions and outlook	65
5.7	Appendix	66
5.7.1	Comparison of cryocooler in low- and high-power mode	66
5.7.2	Calibration of the photodiode signal	67
	Bibliography	69
	Summary	81
	Samenvatting	83
	Curriculum Vitae	85
	List of publications	87
	Acknowledgements	89

1 Introduction

Surface acoustic waves (SAWs) are a particular type of mechanical waves that are confined to the surface of a material. These waves occur in nature during earthquakes, and they are responsible for most of the destruction associated with them. In contrast to these catastrophic events, well-controlled miniature versions of these *earthquakes* play an essential role in modern technologies such as telecommunication devices. If you own a smartphone, it's very likely that several miniature earthquakes are generated right now inside your pocket.

Unlike large-scale earthquakes, where surface acoustic waves typically have sub-Hertz frequencies, kilometer-sized wavelengths, and displacement amplitudes reaching meters, the surface acoustic waves generated in your smartphone have GHz frequencies, micrometer-sized wavelengths, and sub-nanometer displacement amplitudes. To put the difference in perspective, the disparity in the amplitudes of these two types of waves is comparable to the difference in size between a human and an atom. In this thesis, we will focus on the second kind, and in particular on Rayleigh waves, which is a type of surface wave whose existence was predicted by Lord Rayleigh in 1885 [1].

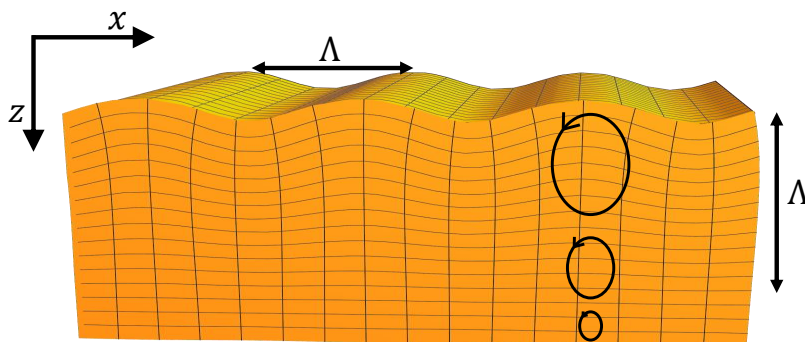


Figure 1.1: A Rayleigh wave of wavelength Λ decays with penetration into the material.

These waves are confined to the surface of the host medium, with a displacement amplitude that decays exponentially with the penetration into the material, vanishing at a distance of about one acoustic wavelength from the surface. In particular, the surface displacement has two components, one perpendicular to the surface, and one along the propagation direction of the waves, with a phase difference between the two that results in an elliptical motion of a volume element, as shown in Fig. 1.1.

Besides the surface confinement, which allows these waves to propagate over long distances, they have other characteristics that make them widely employed in modern technologies. They can be easily excited on piezoelectric materials by using interdigitated comb-shaped metal electrodes called interdigital transducers (IDTs), which are easy to fabricate with standard lithographic processes such as e-beam lithography. Due to the low speed of sound in solids compared to the speed of light, these waves have micrometer wavelengths at gigahertz frequencies, which makes them suitable for miniaturization

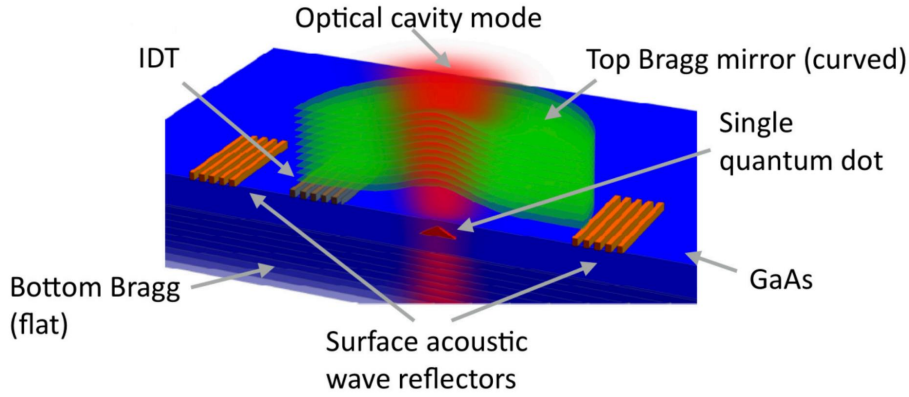


Figure 1.2: Conceptual illustration of a platform that allows confined SAWs on GaAs to interact with InGaAs quantum dots, which can be optically read out.

of electronic devices such as filters, delay lines, oscillators, and other signal-processing devices [2–8]. Due to their surface propagation, these waves can strongly interact with molecules, particles, and cells in contact with the free surface, enabling the sensing and manipulation of chemical substances and biological matter [6, 9–14].

Over the past two decades, SAWs have also started to be employed in quantum technologies and research due to their ability to interact with a variety of different quantum systems such as semiconductor quantum dots (QDs) [15–21], superconducting qubits [22–25], and defect centers [26–28]. Due to this range of interactions, SAWs have been proposed for a universal quantum transducer [29], and can be used in hybrid quantum systems [30, 31] to enable quantum transduction, for example, between microwave and optical photons [32–37]. The intrinsic surface confinement allows SAWs to propagate long distances with little dissipation, also enabling quantum protocols relying on propagating phonons [38–40].

This PhD project is intended to be the starting point to expand the research conducted at Leiden University into the field of quantum acoustics. For this purpose, this project primarily focuses on developing a platform where SAWs on GaAs interact with InGaAs quantum dots, which in turn can be optically read out. This can be achieved by confining the SAWs within an acoustic microcavity, and the quantum dots within an open-access optical microcavity, as shown in Fig. 1.2. In the rest of this introduction we will break down the individual components that constitute this platform.

1.0.1 Generation of surface acoustic waves

SAWs can be efficiently excited on a piezoelectric material using an interdigital transducer (IDT). Invented in 1965 by White and Voltmer [41], this transducer consists of two comb-shaped metal electrodes patterned on a piezoelectric material and allows the conversion of electrical energy into mechanical waves through the inverse piezoelectric effect. The same transducer can also detect surface waves via the direct piezoelectric effect, which converts mechanical energy back into an electrical signal.

The simplest IDT geometry is illustrated in Fig. 1.3, where two adjacent fingers belonging to the different metal combs form the unit cell of the IDT. This unit cell is characterized by the width of the electrodes d which, in this case, is equal to half the pitch p (center-to-center distance between two adjacent fingers), the length L of the fingers, and the acoustic aperture W , which corresponds to the overlap between the fingers

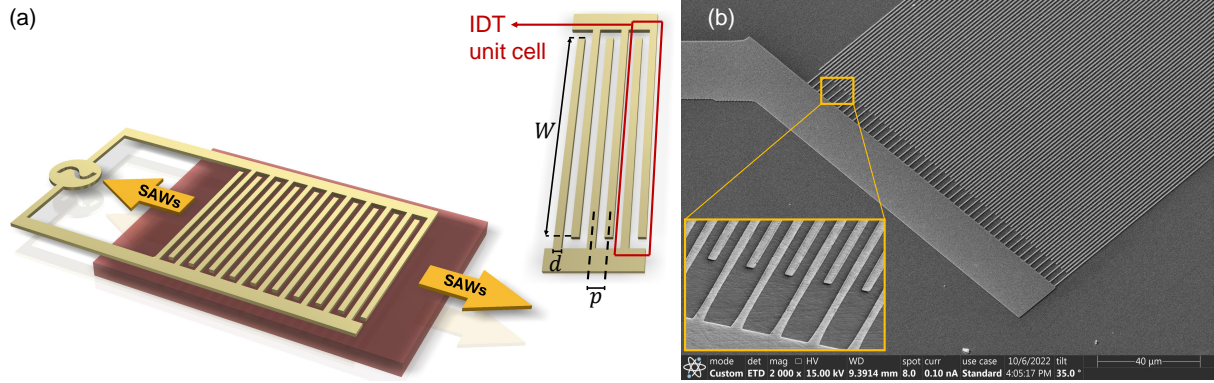


Figure 1.3: Interdigital transducer (IDT). (a) Sketch of a bidirectional interdigital transducer. (b) Scanning electron microscope picture of an IDT fabricated on GaAs by metal deposition of aluminium, with $d = 700$ nm, $p = 1.4$ μm for a design wavelength $\Lambda = 2.8$ μm .

in the transverse direction of the IDT.

The repetition of this unit cell forms the complete IDT, where N_f is the total number of finger pairs. The fingers on the same comb are connected via metal bus bars, to the signal and ground electrodes. The pitch p , together with the phase velocity of SAWs v_{SAW} , defines the central (or synchronous) frequency of the IDT $f_0 = v_{SAW}/2p$. Applying a voltage signal at this frequency results in constructive interference between the waves generated by individual unit cells of the IDT, thereby generating stronger SAWs. The amplitude of the generated SAWs is approximately proportional to the number of finger pairs in the IDT N_f . While increasing the number of finger pairs might seem advantageous, it also affects the frequency bandwidth of the IDT. The 3 dB frequency bandwidth is $\Delta f \simeq f_0 \times 0.885/N_f$ [42].

The IDTs described in this thesis, are aluminium IDTs with $N_f = 10$, fabricated on (001)-cut GaAs, and oriented along the [110] direction, for which the phase velocity of SAWs is $v_{SAW} = 2865$ m/s [43]. The pitch is $p = 1.4$ μm , resulting in a synchronous frequency $f_0 \simeq 1.02$ GHz and a 3 dB frequency bandwidth of $\Delta f \simeq 90$ MHz. The width of the fingers is $d = 700$ nm, the finger length $L = 313$ μm , and the acoustic aperture $W = 304$ μm , resulting in low beam diffraction [8]. The thickness of the aluminium is kept below 100 nm for the devices presented in this work.

The IDT described above is the simplest realization of a SAW transducer, and corresponds to a bidirectional transducer, since it equally excites surface acoustic waves traveling in both directions. In this thesis, we use this configuration, although other geometries, such as unidirectional transducers [44, 45], or focusing IDTs [46, 47], are also possible.

1.0.2 Acoustic cavities and phonon confinement

Acoustic mirrors can be arranged to form an acoustic Fabry-Perot cavity, providing additional in-plane confinement to the SAWs. These mirrors are realized by periodically modulating the mechanical impedance of the surface on which the waves travel akin to a *distributed Bragg reflector* (DBR), either with grooves etched in the piezoelectric material or with metal gratings equivalent to short-circuited IDTs [29]. In our case, we use metal gratings with fingers having the same parameters as the IDTs. In this configuration, the

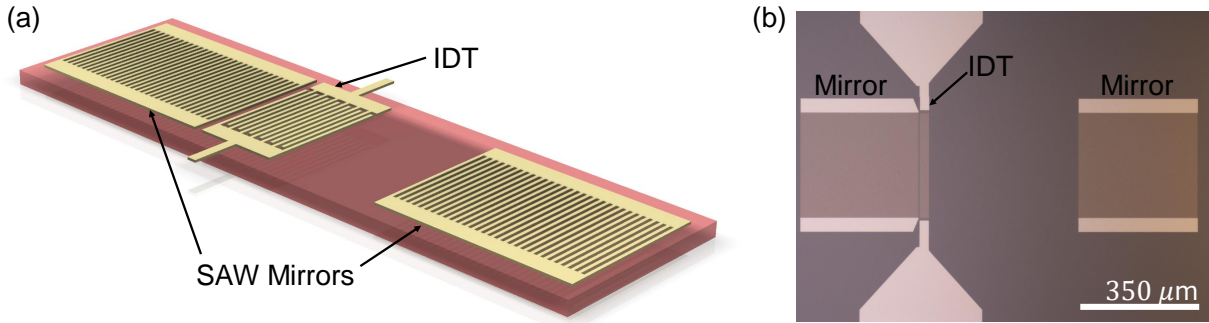


Figure 1.4: (a) Illustration of a SAW acoustic cavity with embedded IDT (1-port resonator). (b) Optical microscope image of a SAW cavity on GaAs.

center frequency of the SAW mirror is given by $f_0 = v_{SAW}/2p$, where p is the grating pitch and v_{SAW} is the phase velocity of SAWs in the mirror. The excitation of SAWs is provided by an IDT, typically embedded in the cavity. The same IDT can be also used for detecting SAWs, and in this case, the device is called a 1-port resonator, as illustrated in Fig. 1.4.

The total reflectivity of the mirror depends both on the reflectivity of a single finger r_s and on the total number of fingers in the mirror N_m . While the geometrical cavity length L_c is given by the separation between the two mirrors, the effective cavity length is larger, due to the exponential decay of the acoustic field in the mirrors $L_{eff} = L_c + 2L_p$, where L_p is the penetration depth inside the mirrors. The cavity can then be modeled as two thin reflectors separated by a distance L_{eff} .

The interaction between a single phonon and other quantum systems depends on the displacement associated with the single phonon. This is given by the zero-point mechanical motion $U_0 = \sqrt{\hbar/(2m_{eff}f_0)}$, where \hbar is the reduced Planck constant, m_{eff} is the effective mass of the mechanical mode, and f_0 is its frequency. An approximation of m_{eff} for surface acoustic waves can be given in terms of material density ρ and mode volume V . Assuming that the penetration depth of SAWs into the material is approximately one acoustic wavelength Λ we obtain

$$U_0 \simeq \sqrt{\frac{\hbar}{2\rho v_{SAW} A}}, \quad (1.1)$$

where A is the surface area on which the phonon is confined. Taking into account the mode shape and material properties, the estimate for GaAs is $U_0 = 1.9 \text{ fm}/\sqrt{A[\mu\text{m}^2]}$ [29], where A is the area of the cavity, expressed in μm^2 .

From this, it is clear that to achieve high coupling of phonons with other quantum systems, a SAW cavity should not only have high quality factor Q , but also a low mode volume. In principle, we can reduce the mode volume by employing gratings with higher metal thickness h , which increases the single finger reflectivity r_s and, with this, reduces the penetration depth of the acoustic field inside the mirrors.

For a highly reflective mirror, the penetration depth is indeed related to the single finger reflectivity by $L_p \simeq \Lambda/(4|r_s|)$ [29, 48], where Λ is the acoustic wavelength and $|r_s| = C_1(h/\Lambda) \sin(\pi d/p) + C_2(h/\Lambda)^2 \cos(\pi d/p)$, with $C_{1,2}$ being material-dependent prefactors [49]. However, increasing the metal thickness also increases losses in the mirrors via scattering of surface waves into bulk waves (bulk losses) proportional to $(h/\Lambda)^2$ [50], so

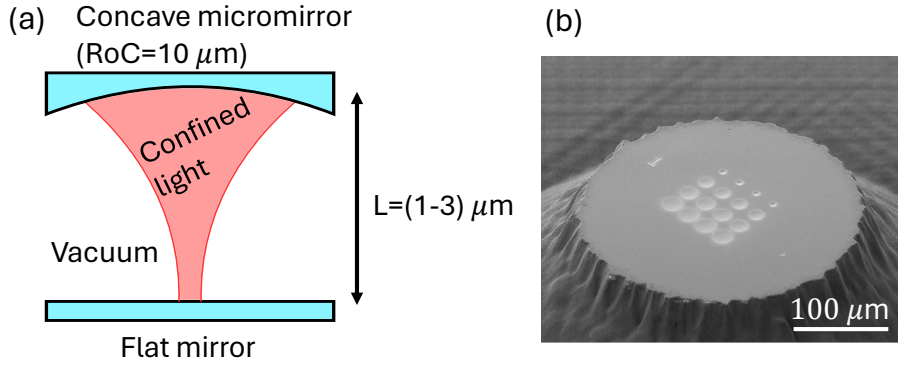


Figure 1.5: (a) Sketch of the open-access optical microcavity, with plano-concave mirrors configuration. (b) Scanning electron microscope image of the micromirror array used for our cavity. The concave mirrors have radii of curvature (RoC) ranging from 100 to 10 μm .

a compromise must be found to achieve high-quality factors while maintaining low mode volume.

Finally, we note that there are other contributions to losses in the acoustic cavity, such as radiation through the mirrors, diffraction, and material losses [29, 49]. The contribution of the bulk losses is negligible at room temperature, due to much higher material losses, but it becomes problematic at cryogenic temperatures where material losses have been minimized.

Planar cavities at GHz frequencies with quality factors of $Q \sim 10^5$ have been achieved on GaAs at mK temperatures, but only with a cavity length of several hundred micrometers [51]. For shorter effective cavity lengths of $L_{eff} \sim 40\lambda$, quality factors of $Q \sim 10^3$ are achievable [29]. To achieve an even smaller cavity surface area A , different cavity geometries are needed to provide confinement also in the transverse direction. With concave cavities, for example, it is possible to achieve $A \simeq (40 - 200) \mu\text{m}^2$, corresponding to single phonon displacements $U_0 \simeq (0.1 - 0.3) \text{fm}$ [15, 20, 29, 52].

1.0.3 QD interaction: optical microcavities

As seen in the previous section, the coupling between SAW phonons and other quantum systems depends on the displacement associated with a single phonon. In a piezoelectric material, SAWs have an associated strain and electric field that allow them to interact with semiconductor quantum dots, if they are located close to the surface. In future experiments, we aim to couple SAWs with InGaAs quantum dots (QDs) in a GaAs substrate, which is possible via the modulation of the energy levels of the QDs induced both by the deformation potential (SAW strain) and by the quantum-confined Stark effect (SAW electric field) [19].

To enable applications such as single phonon detection and microwave-to-optical quantum transduction, it is desirable to place the interacting QD-SAW system in an optical microcavity, to boost the optical readout and enhance the spontaneous emission of the QD into the optical cavity modes [53–56].

Due to the free-surface requirement needed to generate SAWs, a suitable type of optical microcavity are open-access microcavities, a miniaturized version of Fabry-Perot optical cavities. Here two mirrors, where at least one has a micrometer-scale curvature, are

separated by an air or vacuum gap and can be positioned with very high precision at a micrometer distance, to form a cavity as shown in Fig. 1.5.

Despite the high tunability provided by these cavities, which allows to be used them in high-efficiency single-photon sources [56,57], these cavities do not have a high mechanical stability, as the two mirrors are not integrated in the same monolithic structure and can move with respect to each other in the presence of external mechanical vibrations. While this is not a significant problem in helium bath cryostats, which can be made mechanically quiet, resulting in very high mechanical stability of the cavity with root mean square (rms) fluctuation of the cavity length down to 4.3 pm [58], it hinders the operation in closed-cycle cryostats.

To circumvent this problem, low-pass mechanical filters have been employed in these cryostats, to allow the operation of fiber-based open-access microcavities with cavity length fluctuations of 15 pm rms in non-contact mode, down to 0.8 pm rms when the two mirrors are in direct contact [59]. However, this design is not easily compatible with free-space optical coupling to the cavity, since the presence of a mechanical low-pass filter in the cryostat gives rise to time-dependent fluctuations of the optical power coupled to the cavity.

In chapter 5, we focus on the development of a highly stable open-access microcavity for operation in a standard closed-cycle cryostat with free-space optical coupling. In particular, we demonstrate the operation of an open-access microcavity with high mechanical stability, by using standard active feedback stabilization, without the use of a dedicated mechanical low-pass filter [60]. This is an important step towards the commercialization of quantum technologies since closed-cycle cryostats are turnkey systems that require minimal maintenance and have high portability.

1.0.4 Thesis outline

The project presented in this thesis aims to develop a platform for quantum acoustics experiments where surface acoustic wave (SAW) phonons interact with InGaAs quantum dots (QDs). To enhance the phonon-QD interaction, GHz acoustic cavities were nanofabricated on a GaAs substrate, which will also host the quantum dots in future experiments. Additionally, to enhance the photon-QD interaction, and to improve the optical readout of the quantum dot, an open-access optical microcavity with high mechanical stability was constructed within a closed-cycle cryostat.

While the nanofabrication of the planar SAW cavities is in principle a straightforward process, their characterization is found to be more intricate. The conventional approach involves using the interdigital transducer (IDT) for both excitation and detection of the SAWs, measuring the microwave reflectance spectrum with a vector network analyzer (VNA), and providing information on the position of the resonance frequencies. However, due to the transverse extension of the IDT across the entire cavity, this method does not offer insights into the acoustic field distribution within the cavity. Although adequate for ideal systems with frequency and spatially separated resonances, this approach complicates the interpretation of results in real cavities. For this reason, our focus shifted towards the development of an imaging system capable of measuring the spatial distribution of GHz surface acoustic waves both in amplitude and phase.

In **Chapter 2** we introduce this system: a fiber-based scanning Michelson interferometer for imaging GHz surface acoustic waves. Specifically, we demonstrate the accurate measurement of out-of-plane surface displacement using a focused laser beam with a beam

spot size matching the surface acoustic wavelength. With this setup, we investigate a 1-port GHz SAW resonator on GaAs and compare the results with VNA measurements. We show that by imaging the amplitude and phase of the surface displacement, we can distinguish between frequency and spatially overlapping transverse modes. Understanding the distribution of the acoustic field inside the cavity is crucial for future interaction with localized quantum dots.

In **Chapter 3** we employ the scanning Michelson interferometer to analyze interference fringes in GHz surface acoustic wave cavities. In particular, we investigate the presence of spurious bulk acoustic waves (BAWs) in SAW cavities, using two-dimensional spatial Fourier analysis. While BAWs can be readily detected by imaging the amplitude and phase of the acoustic field distribution, we demonstrate that this is also achievable with amplitude-only measurements, due to the interference between bulk and surface waves. This method can be valuable for optimizing SAW cavities, as the scattering of surface waves into bulk waves constitutes a loss mechanism.

In **Chapter 4** we demonstrate the optical Talbot effect by diffraction of light from standing surface acoustic waves, which behave as a dynamical diffraction grating.

In **Chapter 5** we present the realization of an open-access optical microcavity with high mechanical stability in a standard closed-cycle cryostat. Our setup features free-space optical coupling and is carefully designed to allow cavity-length stabilization using conventional feedback techniques, removing the need for a dedicated mechanical low-pass filter in the cryostat.

2 Imaging transverse modes in surface acoustic wave cavities

Full characterization of surface acoustic wave (SAW) devices requires imaging the spatial distribution of the acoustic field, which is not possible with standard all-electrical measurements. This can be done, for example, with optical probes employing a strongly focused laser beam, ideally much smaller than the acoustic wavelength. This condition breaks down for GHz-frequencies SAWs, where the acoustic wavelength is of the order of the optical wavelength. Here we analyze this regime and we show that even when the focused laser beam is slightly bigger than the acoustic wavelength, it is still possible to accurately measure SAW displacements, and to perform high-resolution imaging of the standing SAWs. We demonstrate this in a fiber-based scanning Michelson interferometer, where we characterize a SAW cavity by using a strongly focused laser beam with a spotsize $2w_0$ equal to the acoustic wavelength $\Lambda = 2.8 \mu\text{m}$. By frequency- and spatially-resolved displacement measurements we reveal the presence of frequency-overlapping transverse modes and their superpositions. These are not resolved in standard all-electrical measurements performed with a vector network analyzer, and we show that this can cause wrong estimation of the cavity parameters. The combination of simultaneous spatially- and frequency-resolved measurements can have wide applications in the characterization of SAW devices, and can be especially useful in sensing and quantum acoustics, where the interaction between the acoustic field and a quantum system is strongly localized in space, or where multiple acoustic modes are employed.

This chapter is based on: M. Fisicaro, T. A. Steenbergen, Y. C. Doedes, K. Heeck and W. Löffler, Imaging transverse modes in a GHz surface acoustic wave cavity, under review, arXiv:2408.11630 (submitted).

2.1 Introduction

Surface acoustic waves (SAWs) are mechanical waves that travel along the surface of a material. Among these waves is a special type known as Rayleigh waves, which are characterized by an elliptical motion of the surface elements. These waves find many applications in SAW devices, due to the ease of excitation on piezoelectric substrates via interdigital transducers (IDTs [6, 41, 61]).

SAWs are interesting for a number of applications: their surface confinement makes them useful in chemical and biological sensing, where a compound placed on the free surface of the piezoelectric material interacts with the propagating waves [14, 62–64], and manipulation of biological matter such as cells [11, 65, 66]. The small acoustic wavelength at GHz frequencies allows for miniaturization of electronic filters, finding applications in telecommunications [8, 67, 68]. Due to their long coherence times, and to the ability of interacting with many different quantum systems, SAWs find many applications also in quantum physics research where they can couple to a variety of two-level systems, such as superconducting qubits [22–25], NV centers and quantum dots [20, 21, 29, 69, 70]. Many of these applications require spatial confinement of the SAWs, and this can be achieved by patterning periodic gratings (Bragg mirrors) on the surface of the material [52, 71–73].

A typical configuration is a 1-port resonator, consisting of an acoustic cavity made with two SAW mirrors enclosing an IDT, which can be simultaneously used for SAW excitation and detection. The characterization of SAW devices is typically done with an all-electrical measurement using a Vector Network analyzer (VNA) to measure the reflectance spectrum of the IDT: at a cavity resonance, the electromechanical coupling of the piezoelectric material changes the electrical properties of the IDT, allowing to identify the resonance frequencies of the cavity modes [74]. While simple, this approach only provides limited information such as the acoustic resonance spectrum of the cavity, and can not provide any spatial information on the acoustic field distribution inside the cavity. Imaging the SAW displacement is therefore important for the understanding and optimization of SAW devices, and it has been done with a few different techniques such as atomic force microscopy (AFM) [75], X-ray diffraction [76–78], and optical probes [79–84]. Among these, interferometric optical probes stand out for their simple implementation and high sensitivity in displacement measurements [85–89]. However, this method is not often employed with GHz SAW devices, as in this regime the acoustic wavelength Λ is comparable in size with the focused laser beam spot, typically in the micrometer range.

Here we focus on this regime, and we present a fiber-based scanning Michelson interferometer with a heterodyne circuit for imaging 1 GHz SAWs ($\Lambda = 2.8 \mu\text{m}$), with a focused laser beam having a spot size of $2w_0 = 2.8 \mu\text{m}$. We analytically calculate the effects of the beam spot size in the detected interferometric signal, and show that it is still possible to image SAWs, even when the beam spot size is comparable in size or slightly bigger than the SAW wavelength Λ , only resulting in a reduction of the detected interferometric signal, that can be taken into account to retrieve an absolute value of the measured SAW displacement.

We investigate a planar-mirror SAW cavity device with integrated IDT. We measure frequency-resolved spatial displacement maps resolving both amplitude and phase of the SAW displacement. Despite the large spot size, we are able to resolve small features of standing SAWs, as predicted by our model. We show the presence of frequency-overlapping transverse modes and their mode-superpositions, which give rise to unconventional transverse mode profiles. Finally, by comparison with an all-electrical VNA measurement, we

show how this latter method is not able to resolve the transverse modes, which can lead to an incorrect estimation of the width and center frequency of the resonances in the SAW cavity.

2.2 Experimental setup

2.2.1 SAW device

The device investigated in this paper is a planar SAW cavity, as shown in Fig. 2.1 (b). This device has been nanofabricated via e-beam lithography and e-beam evaporation of aluminum on a (001)-cut GaAs substrate. It consists of an IDT with 10 metal finger pairs, placed inside a cavity formed by two planar mirrors, each one made of 250 metal fingers. The metal thickness of the IDT and the mirrors is $h = 50$ nm, the centre-to-centre finger spacing is $p = 1.4 \mu\text{m}$ and the finger width is $d = 700$ nm. The two mirrors are placed at a distance of $L_{\text{cav}} = 470 \mu\text{m}$ from each other, and the length of the fingers on the transverse direction is $L_y = 308 \mu\text{m}$. The device is oriented along the [110] direction, for which the speed of the Rayleigh wave is $v_{\text{SAW}} \simeq 2860$ m/s, resulting in a wavelength $\Lambda \simeq 2.8 \mu\text{m}$ at the frequency $f_{\text{SAW}} = 1.022$ GHz.

2.2.2 Fiber-based scanning Michelson interferometer

The optical setup shown in Fig. 2.1 (a) is a scanning Michelson interferometer implemented with a polarization-maintaining single-mode fiber coupler as the beam splitter (PM BS). Light from a narrow-linewidth fiber-coupled laser (TOPTICA DL PRO) with $\lambda = 980$ nm enters the fiber coupler through port A, and is split into the sample (port D) and reference arm (port C). In the reference arm, the light is focused onto a mirror by a single aspheric lens L_1 , and back reflected into the fiber. In the sample arm, light from port D is first collimated by an aspheric lens (L_2), and then strongly focused onto the GaAs-based SAW device by an aspheric lens with 0.55 NA (L_3), resulting in a spot size of $2w_0 = 2.8 \mu\text{m}$, where w_0 is the beam waist radius.

Due to Fresnel reflection, at $\lambda = 980$ nm, the GaAs surface acts as a partial mirror with reflectivity $R \simeq 0.3$, and the reflected light is coupled back into the fiber coupler through the same port D. The reflected light from the reference and sample arm of the interferometer is then recombined through the same fiber coupler, and exits through port B. After port B, the recombined light is split again by a fiber splitter (30:70 splitting ratio). The weaker part is sent to a slow photodiode (Thorlabs PDA36-EC), the other to a radio frequency photodiode (New Focus 1514). The slow photodiode (slow PD) is used to generate the error signal used for stabilization of the interferometer (side-of-fringe lock). This signal is first sent to a PID controller, and then to a piezo driver used to actuate the piezo element on which the mirror in the reference arm of the interferometer is attached.

The GHz signal detected with the radio frequency photodiode (RF PD) is down-converted to an intermediate frequency signal in the range 1 – 40 MHz by the heterodyne circuit, and then measured with a lock-in amplifier (Zurich Instruments HF2LI, 50 MHz bandwidth). The origin of the 1 GHz fluctuations in the optical power lies in the interference between the light from the reference arm, and the light from the sample arm of the interferometer, which is phase-modulated at 1 GHz due to the surface displacement

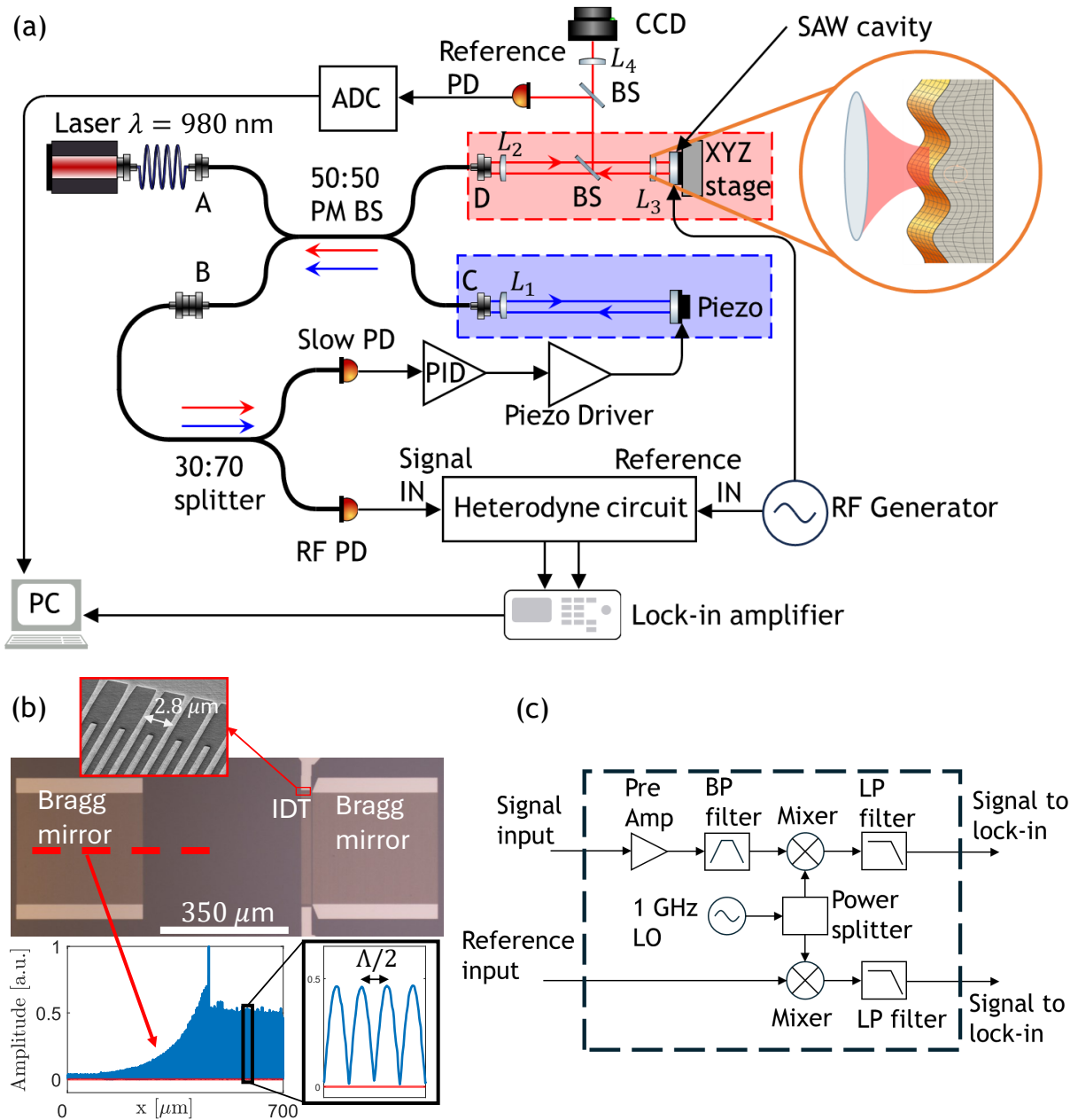


Figure 2.1: (a) Schematic of the fiber-based scanning optical interferometer. (b) Optical microscope image of the SAW cavity device, and an electron microscope picture of the IDT metal fingers (top inset). In the bottom panel we show an example of the displacement field, measured with the optical interferometer at the position indicated by the red dashed line. The exponential decay of the field inside the Bragg mirrors is visible, as well as the nodes and antinodes of the standing waves (bottom right). (c) Schematic of the custom-built 1 GHz heterodyne circuit used to convert the 1 GHz SAW signal from the RF photodiode into an intermediate-frequency signal in the range of 1 – 48 MHz.

associated to the SAWs. In the sample arm of the interferometer, two pellicle beam splitters redirect part of the back reflected light to a CCD, used to image and align the SAW device, and to a reference photodiode (reference PD), which is used to record simultaneously a reflectivity image of the SAW device to correlate the displacement maps to the device structure.

Finally, the SAW devices is mounted on a 3-axes nanopositioning stage, where translation along the optical (z) axis allows us to adjust the focus of the laser beam, while the x and y axes allow us to scan the laser focus over the SAW device. The imaging of the SAW displacement field is done line-by-line with continuous scanning of the x axis of the nanopositioner, simultaneously recording the lock-in signal and the encoder signal of the x translation stage, allowing fast scans with a maximum resolution of ~ 7 nm. An example of such measurement is shown in the bottom panel of Fig. 2.1 (b), where we show the amplitude of the standing SAWs over a line in the middle of the transverse direction of the SAW cavity, resulting in a spatial x – periodicity of half the acoustic wavelength $\Lambda/2$, as expected for standing waves.

2.2.3 Heterodyne circuit

In order to perform heterodyne measurements, we need to compare the signal at the output of the photodiode to a reference signal. For this we use a power splitter to split the signal generated by the RF generator shown in Fig. 2.1 (a), one part is used to drive the IDT in the SAW cavity at a frequency $f_{SAW} \sim 1$ GHz, and the other part is used as the reference signal in the heterodyne circuit. In the heterodyne circuit shown in Fig. 2.1 (c), a local GHz oscillator is used to generate a signal at the frequency $f_{LO} = f_{SAW} - f_{IF}$, where f_{IF} is the intermediate frequency at which we want to downconvert the RF photodiode signal.

The signal generated by the local oscillator is split in two by a power splitter in order to be mixed with the reference and input signal. The reference signal is first mixed with the local oscillator, and then low-pass filtered, obtaining at the output a reference signal at the intermediate frequency f_{IF} . On the other hand, the low-amplitude input signal is pre-amplified, band-pass filtered, mixed with the local oscillator and finally low-pass filtered, obtaining at the output a signal at the intermediate frequency f_{IF} .

These two outputs are then fed into the lock-in amplifier: the output from the reference port is used as an external oscillator in the lock-in amplifier, to demodulate the output coming from the signal port. As a result, the lock-in amplifier can measure amplitude and phase of the SAW displacement at the intermediate frequency f_{IF} .

When we want to change the drive frequency of the IDT f_{SAW} , we change accordingly also the frequency of the local oscillator f_{LO} , such that the intermediate frequency is kept constant at the arbitrary value of $f_{IF} = 22$ MHz. Due to the bandwidth of the band-pass filter, f_{SAW} is limited to 900 – 1370 MHz.

2.2.4 Voltage-displacement calibration

The voltage signal measured by the lock-in amplifier is converted into the displacement associated to the SAWs by considering the overall gain of the interferometer:

$$\zeta = \frac{\lambda}{4\pi P_{half}} \frac{1}{C_{RF} \times G_{LI} \times r} \times 10^6 \left[\frac{\text{pm}}{\mu\text{V}} \right], \quad (2.1)$$

where the first term $4\pi P_{half}/\lambda$ gives the change in the optical power caused by a given flat-surface displacement for an interferometer locked at the side of the fringe. λ is the optical wavelength, $P_{half} = 170 \mu\text{W}$ is the optical power at which we side-of-the-fringe lock the interferometer, measured at the RF photodiode, $C_{RF} = 700 \text{V/W}$ is the conversion factor between input optical power and voltage at the output of the RF photodiode, $G_{LI} = 20.6$ is the total voltage gain provided by the heterodyne circuit, and $r = r(w_0, \Lambda)$ is a reduction factor caused by the finite size of the beam waist radius w_0 compared to the acoustic wavelength Λ .

As discussed in Appendix 2.5.1, the analytical calculation of the reduction factor leads to

$$r(w_0, \Lambda) = \exp\left(-\frac{\pi^2 w_0^2}{2\Lambda^2}\right), \quad (2.2)$$

showing an exponential dependence on w_0^2 . An accurate measurement of the beam waist is therefore essential for a proper calibration, and we measure it by using a variation of the well known knife-edge technique [90,91], where the focused Gaussian beam is scanned over the boundary between free GaAs surface, and the aluminium contact pad of the IDT.

Due to the two different reflectivities of aluminium and GaAs, in reflection we can measure a transition over this region in the reflected optical power recorded by the reference photodiode, resulting in a measured beam waist radius $w_0 = 1.4 \mu\text{m}$, as shown in appendix 2.5.2. In our experiment, the SAW wavelength is $\Lambda = 2.8 \mu\text{m}$, resulting in a reduction factor $r = 0.29$, and a total gain of the interferometer equal to $\zeta = 0.154 \text{pm}/\mu\text{V rms}$.

2.3 Imaging of transverse modes in a planar SAW cavity

Here we investigate the planar SAW Fabry-Perot cavity shown in Fig. 2.1 (b): first we characterize the cavity by means of an all-electrical measurement done with a vector network analyzer (VNA), then with the interferometric optical setup, and we show how the latter approach allows for a better understanding of the cavity modes and a better estimation of the cavity parameters. The all-electrical VNA measurement is performed by driving the IDT in the cavity with a vector network analyzer (NANO VNA), and measuring the reflected electrical power. At a resonance of the cavity there is conversion between electrical energy and mechanical energy, therefore we expect to observe a dip in the measured reflected power. By performing this measurement at different frequencies, we obtain the microwave reflectance spectrum of the SAW cavity ($|S_{11}|^2$), showed in Fig. 2.2.

The device shows several resonance frequencies around 1 GHz, with a free spectral range $\Delta f_{FSR} = 2.7 \text{MHz}$. In the rest of this chapter, we will focus on the third reflection dip, which has a resonance frequency measured by the VNA of $f_c^{VNA} = 1.02197 \text{GHz}$, and shows an asymmetric behavior on the high-frequency side, visible in the right panel in Fig. 2.2. This asymmetry in the reflection dip is attributed to the excitation of frequency-overlapping transverse modes, but there is no clear structure corresponding to the individual peaks of these modes.

This is because the IDT can not distinguish the modes spatially, due to its transverse spatial extension. In fact, at a particular excitation frequency close to the resonance of the fundamental mode, we have superposition of different cavity modes, each one with a different transverse spatial profile, different amplitude and different phase. This leads

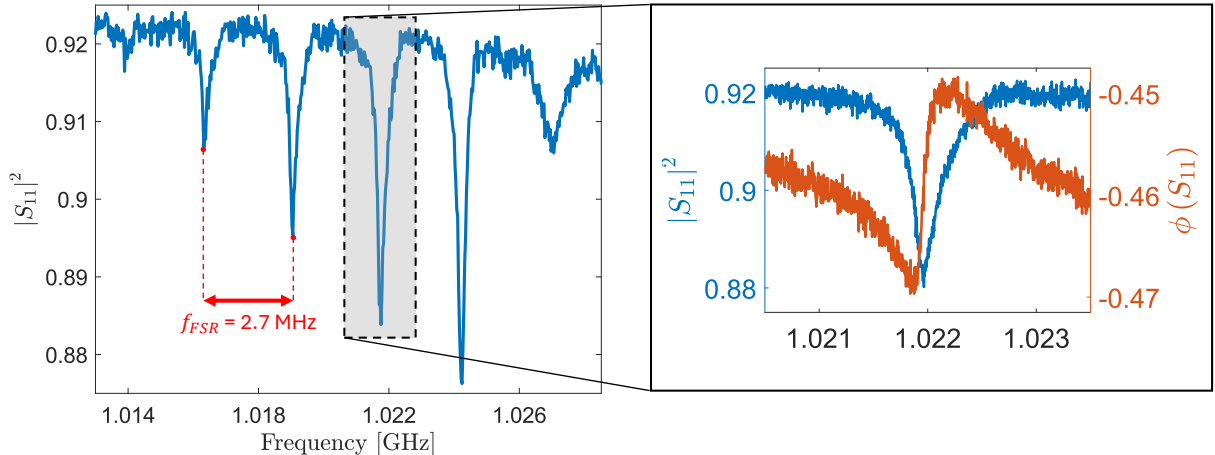


Figure 2.2: Microwave reflectance spectrum of the SAW cavity ($|S_{11}|^2$), measured with a vector network analyzer. The spectrum shows multiple longitudinal modes separated by a free spectral range $f_{FSR} = 2.7$ MHz, corresponding to an effective cavity length $L_{eff} = 530 \mu\text{m}$. By comparison with the geometrical cavity length $L_{cav} = 470 \mu\text{m}$, we obtain a penetration depth into the Bragg mirror of $L_p \simeq 30 \mu\text{m}$. In the right panel we show the cavity resonance that is investigated with the optical setup, where the red curve corresponds to the phase of the S_{11} parameter. The measured resonance frequency is $f_c^{VNA} = 1.02197$ GHz, and the full width half maximum is measured to be $f_{FWHM} = 265$ kHz.

to a complex frequency- and spatially-dependent mode superposition, and since the IDT is extended along the full transverse length of the cavity $L_y = 308 \mu\text{m}$, it measures a spatial average of this mode superposition, which in our case does not show a multi-peak structure.

In order to separate these transverse modes in the frequency domain, we measure the SAW cavity with the scanning Michelson interferometer. Since this setup uses a focused laser beam as a small localized probe, we expect the optically measured frequency spectrum to be dependent on the position at which it is measured. Due to placement of the IDT centered to the SAW cavity axis, we expect only symmetric transverse modes ([92]). We drive the IDT with a RF power of 15 dBm, and spatially scan a few periods of the standing waves across the longitudinal z direction of the cavity, recording the peak value of the measured displacement amplitude. The procedure is repeated for different frequencies, allowing us to reconstruct the frequency spectrum of the intracavity field in the middle of the cavity, as shown in Fig. 2.3 (b). In this frequency spectrum we now recognize several distinct peaks, which correspond to different transverse modes as we show now.

For this, we use the Michelson interferometer to image the spatial acoustic field distribution inside the SAW cavity for the four peak frequencies $f_0 - f_3$, and we calibrate the measured displacement using Eq. 2.1. In particular, we image a region inside the SAW cavity of $5.6 \mu\text{m}$ in the longitudinal direction, and $400 \mu\text{m}$ in the transverse direction. This is shown in Fig. 2.3 (c) - (f), where we plot both amplitude (left) and phase (right), and we show the corresponding cross sections with a white curve. For the amplitude maps, the cross section is taken at the position of an antinode, while for the phase maps the

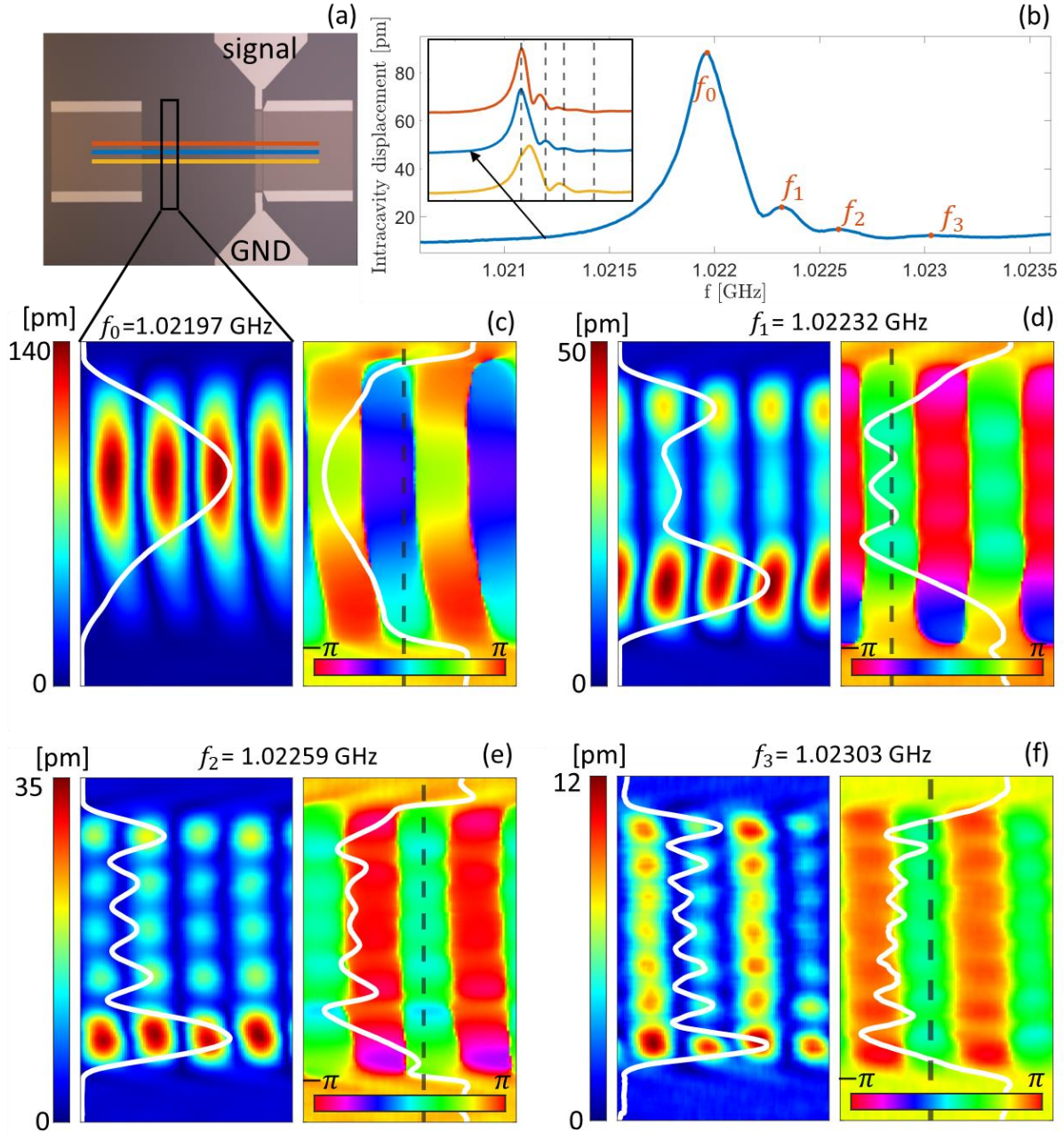


Figure 2.3: Optical measurements of the transverse modes. (a) Optical microscope image of the planar cavity. The red, blue and yellow lines indicate the transverse positions at which we optically measure the resonance spectra shown in (b). (b) Intracavity displacement as a function of frequency, measured in the middle of the transverse direction of the cavity. In the inset three resonance spectra measured at slightly different transverse position are shown, demonstrating significant peak shifting and broadening. (c) - (f): amplitude (left panels) and phase (right panels) of the transverse modes, measured at the indicated peak frequencies, in the area indicated by the black box in (a). The different transverse modes are axially symmetric, showing respectively 1, 3, 5 and 7 lobes on the transverse direction. The white lines show the cross section of the mode profile measured at the position of an antinode as indicated by the dashed lines in the phase plots.

cross section is taken at the longitudinal position indicated by the black dashed line.

These maps show transverse field profiles with an odd number of lobes, in our case 1, 3, 5 and 7, corresponding to axially-symmetric transverse modes. Moreover, by looking at the amplitude distribution of the acoustic field, it is clear that there is an asymmetry with respect to the center of the transverse direction: not only the field distribution is shifted towards the upper side of the cavity, which is visible especially in (c), but for multi-lobe modes, the lobe on the bottom side of the cavity has a higher displacement than the one on the top side. We do not know the origin of this shift and asymmetry, but we hypothesize that it is related to the placement of the signal and ground ports of the IDT.

As mentioned above, due to the presence of the transverse modes which overlap both in frequency and in space, the optically measured acoustic resonance spectrum depends significantly on the transverse position at which it is measured. This is shown in the inset of Fig. 2.3 (b), where we measure the acoustic resonance spectrum at different transverse positions indicated by the colored lines in Fig. 2.3 (a). From this measurement it is clear that, due to mode superposition, the resonance spectrum of the displacement shows peaks with different frequency and shape, depending on the transverse position at which is measured. This makes very hard, if not impossible, to determine accurately the exact resonance frequencies of the different transverse modes, and therefore the acoustic resonance spectrum shown in Fig. 2.3 (b) only gives an estimate of these resonance frequencies.

Another consequence of the mode superposition is that the mode profiles shown in Fig. 2.3 (c) - (f) do not correspond to transverse eigenmodes, but are a superposition of multiple modes at the specific frequency at which they are measured. To show this effect, and to show how we can retrieve the *real* mode profile, we consider the fundamental mode M_0 , and the first transverse mode M_1 . Resonant modes in a cavity are enhanced, with respect to the input field, and the ratio between the enhanced field and the input field is referred to as susceptibility, described by a complex Lorentzian [93]

$$\chi(f) = \frac{1}{1 - 2i \frac{f-f_c}{\Delta f_{FWHM}}} . \quad (2.3)$$

Here, f_c is the mode frequency, and Δf_{FWHM} its width. In particular the susceptibility is characterized by a π phase-shift, as shown in Fig. 2.4 (a), where we plot the intracavity field enhancement for two cavity modes.

Let us now consider what happens when we optically measure the acoustic field distribution at the frequency f_0 . There, the amplitude of the fundamental mode M_0 is maximum, while the amplitude of the first transverse mode M_1 is strongly reduced due to the detuning from its resonance frequency of f_1 . The phase difference between M_0 and M_1 is $\Delta\varphi \sim \pi/2$, so that the modes are almost orthogonal. This means that in principle we should be able to decompose the measured mode profile into the normal modes M_0 and M_1 , by analyzing the X and Y quadratures measured with the lock-in amplifier. To do this, we take the amplitude and phase of the acoustic field distribution measured at f_0 in Fig. 2.3 (c), we apply a phase rotation of $\theta = 1.15$ rad, needed to align the complex acoustic field along the X and Y quadratures, and then we take the real and imaginary part of this complex field, corresponding to the X and Y quadratures.

The result is shown in Fig. 2.4 (b), where now we can better see the transverse profile of the M_0 and M_1 modes. Another interesting phenomenon caused by mode superposition is the destructive interference of modes M_0 and M_1 , visible when we optically measure

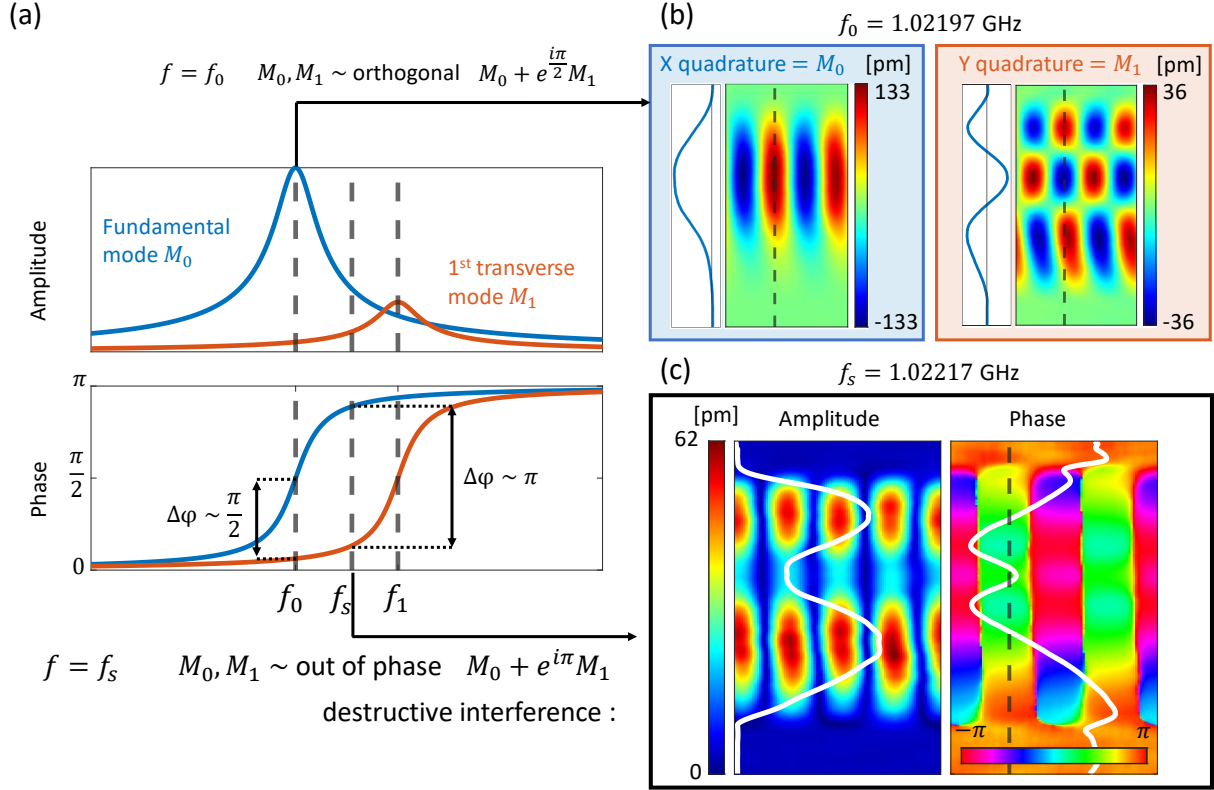


Figure 2.4: Mode superpositions. In (a) we show the amplitude and phase of two frequency-overlapping cavity modes M_0 and M_1 . At the resonance frequency f_0 of the fundamental mode M_0 , the phase difference is $\Delta\varphi \simeq \pi/2$, and the two modes are almost orthogonal, allowing mode decomposition by quadrature analysis shown in (b). At the frequency f_s in between f_0 and f_1 , the phase difference is $\Delta\varphi \simeq \pi$ and the two modes are almost out of phase with a comparable amplitude, leading to destructive interference and a two-lobe structure (c).

the acoustic field distribution at the frequency $f_s = 1.02217$ GHz. Since this frequency is in between f_0 and f_1 , the phase difference between M_0 and M_1 is now $\Delta\varphi \sim \pi$, causing destructive interference between the two. The result is shown in Fig. 2.4 (c), where the amplitude of the acoustic field distribution shows a two-lobe structure. While in principle this could correspond to an antisymmetric transverse mode, the symmetry observed in the phase is proof that this is indeed a mode superposition between symmetric modes, in our case M_0 and M_1 .

Finally, as a demonstration of the accuracy of our measurements, we estimate the surface displacement that we expect for the fundamental mode of the planar SAW cavity. First we calculate the steady-state phonon number \bar{n} starting from the definition of cavity quality factor that takes into account the stored energy:

$$Q = 2\pi f_0 \times \frac{E_s}{P_{loss}}. \quad (2.4)$$

where E_s is the energy stored in the cavity, and P_{loss} is the power loss. At steady state, the stored energy is $E_s = \bar{n} \times h f_0$, where h is the Planck constant, and the power loss must be equal to the input power in the cavity $P_{in} = \eta \times P_{\mu wave}$, where η is the fraction of power

coupled to the cavity, and $P_{\mu wave}$ is the RF power sent to the IDT. The quality factor can also be described in term of linewidth of the resonator $Q = f_0/f_{FWHM}$, where f_{FWHM} is the width at half maximum of the cavity resonance. By comparing this definition to Eq. 2.4, we can obtain the steady-state phonon number

$$\bar{n} = \frac{\eta \times P_{\mu wave}}{hf_0} \frac{1}{2\pi f_{FWHM}}. \quad (2.5)$$

From the microwave reflectance spectrum $|S_{11}|^2$, we estimate $\eta = 0.04$, and $f_{FWHM} = 265$ kHz. The RF microwave power sent to the IDT is $P_{\mu wave} = 15$ dBm, obtaining $\bar{n} = 1.1 \times 10^{15}$. We can convert the steady-state phonon number into a SAW displacement, by using the relation $u = u_{zpm} \times \sqrt{\bar{n}}$, where u_{zpm} is the zero-point motion, and for SAWs on GaAs it has been numerically estimated to be $u_{zpm} \simeq 1.9 \text{ fm}/\sqrt{A[\mu\text{m}^2]}$ [29], where A is the surface area on which the mode is confined, expressed in μm^2 . We estimate $A = L_{eff} \times L_{FWHM} \simeq 9 \times 10^4 \mu\text{m}^2$, where $L_{eff} = v_{SAW}/(2f_{FSR}) = 530 \mu\text{m}$ is the effective cavity length corresponding to the free spectral range $f_{FSR} = 2.7$ MHz of our cavity as measured in Fig. 2.2, and $L_{FWHM} = 170 \mu\text{m}$ is the FWHM of the SAW field profile along the transverse direction in Fig. 2.3 (c).

With these cavity parameters, we obtain an estimate of the SAW peak displacement of $u \simeq 210$ pm, which is of the same order of magnitude as the optically measured value $u_{meas} = 140$ pm in Fig. 2.3 (c). We note that the estimated SAW peak displacement is an overestimation of the real value, since we assumed that all the input power P_{in} dissipated in the IDT goes into excitation of the acoustic waves, whereas in reality there are also Ohmic losses due to the finite resistance of the IDT, metal bus bars and wirebonds.

2.4 Conclusions and outlook

We presented a novel fiber-based interferometric setup capable of imaging SAWs even with a relatively large laser beam spotsize, compared to the acoustic wavelength. We showed that even in this regime, we are able to image SAWs and the high resolution features associated with standing SAWs, and we provided means to quantitatively measure the absolute out-of-plane SAW displacement. Finally we used the optical setup to investigate transverse modes in a 1-port SAW cavity. First we compared a VNA measurement of the resonance spectrum of the cavity, with optical measurements, revealing in this way the transverse modes. Second we imaged these transverse modes, showing how only symmetric modes are excited in the cavity, due to the geometry, and how these modes overlap in frequency and space, modifying both the acoustic resonance spectrum of the cavity, and the spatial transverse profile of the modes. The combination of frequency measurements and spatial imaging enable a more complete characterization of the SAW cavity, and of SAWs devices in general, and can play a crucial role in optimization of SAW devices.

2.5 Appendix

2.5.1 Effects of the beam spot size on the measured interferometric signal

We discuss here the effects of the optical beam spot size on the measured interferometric signal, for which we need to keep in mind the optical interferometer sketched in Fig. 2.1 (a). The gain of the interferometer provided in Eq. 2.1 has been calculated by taking into account the change in the optical power at the photodiode, caused by the displacement of a reflective flat surface in the sample arm of the interferometer. The effect of the beam spot size is incorporated into the reduction factor $r(w_0, \Lambda)$.

We can calculate this reduction factor by comparing the fluctuations in the optical power at the photodiode, caused by reflection from an oscillating flat surface (P_{flat}^Ω), to the fluctuations caused by reflection from the oscillating SAW surface (P_{SAW}^Ω), where Ω is the angular frequency of oscillation. Since the heterodyne detection system detects the rms values of the optical power fluctuations, we introduce P_{flat}^{rms} and P_{SAW}^{rms} , and define the reduction factor as

$$r = \frac{P_{SAW}^{rms}}{P_{flat}^{rms}}, \quad (2.6)$$

where P_{SAW}^{rms} and P_{flat}^{rms} denote the rms value of P_{SAW}^Ω and P_{flat}^Ω respectively.

We now proceed to calculate these two fluctuations in the optical power: looking at Fig. 2.1 (a), first we calculate the electric field coupled back into the fiber both in the reference and sample arm of the interferometer, where the field in the sample arm is modulated in phase by the oscillating surface, then we let the two fields interfere and we keep only the Ω component in the optical power fluctuation. Starting from the reference arm, since the interferometer is locked at half of the interference fringe, we define a reference field with unitary amplitude and constant phase $E_{ref} = \exp(i\pi/2)$.

In the sample arm of the interferometer, we want to calculate the field back-reflected into port D of the fiber coupler for the two cases of SAW oscillations and oscillations of a flat surface. This field is given by the overlap integral between the field supported by the optical fiber, and the field reflected by the oscillating reflective surface. Since optical propagation is unitary, we can calculate this integral at any plane in the sample arm of the interferometer, and for simplicity we choose the plane of the reflecting surface. Here the overlap integral is calculated between the image of the field supported by the fiber E_{fiber} and the reflected fields E_{flat} and E_{SAW} . In the interferometer we can achieve close-to-unity coupling back to the fiber, therefore we can assume that E_{fiber} has the same beam waist of the focused laser beam on the surface, leading to $E_{fiber} = \exp[-(x^2 + y^2)/w_0^2]$. The reflected fields can be expressed as a generic Gaussian beam with an additional phase term picked upon reflection from the oscillating surface:

$$\begin{aligned} E &= \frac{2}{\pi w_0^2} \exp\left(-\frac{x^2 + y^2}{w^2(z)}\right) \times \exp\left[-i\left(2k(z + \Delta z) + k\frac{x^2 + y^2}{2R(z)} - \psi(z)\right)\right] \\ &\simeq \frac{2}{\pi w_0^2} \exp\left(-\frac{x^2 + y^2}{w_0^2}\right) \times \exp(-2ik\Delta z), \end{aligned} \quad (2.7)$$

where we drop the constant propagating phase z , and the phase terms corresponding to the Gouy phase $\psi(z)$ and to the radius of curvature $R(z)$. This approximation is

valid for small surface displacements close to the focus. We can then write $E_{flat} = E_{fiber} \times \exp(-2ik\Delta z_{flat})$ and $E_{SAW} = E_{fiber} \times \exp(-2ik\Delta z_{SAW})$. Let us first consider the flat case, for which the surface displacement is given by $\Delta z_{flat} = A_0 \cos(\Omega t)$, where A_0 is the peak surface displacement, and Ω is the angular frequency of the surface oscillation. The field coupled back to port D of the fiber coupler is given by:

$$\begin{aligned} E'_{flat} &= \iint E_{fiber}^* \times E_{flat} dx dy \\ &= \frac{2}{\pi w_0^2} \iint \exp\left(-2\frac{x^2 + y^2}{w_0^2}\right) \times \exp[-2ik\Delta z_{flat}] dx dy \\ &= \exp(-2ik\Delta z_{flat}) . \end{aligned} \quad (2.8)$$

The total power at the photodiode is given by the interference of E'_{flat} with E_{ref} :

$$\begin{aligned} P_{flat} &= |E'_{flat} + E_{ref}|^2 = \left| \exp\left(i\frac{\pi}{2}\right) + \exp(-2ikA_0 \cos(\Omega t)) \right|^2 \\ &\simeq 2 + 4kA_0 \cos(\Omega t) + 4k^2A_0^2 \cos^2(\Omega t) \end{aligned} \quad (2.9)$$

where we expanded for small displacements A_0 . Keeping in mind that the rms value of a time signal is defined as:

$$P_{rms} = \sqrt{\frac{1}{T} \int_0^T P^2(t) dt} , \quad (2.10)$$

we obtain the rms value of the Ω component $P_{flat}^{rms} = 4kA_0/\sqrt{2}$.

We now repeat the same calculations for E_{SAW} , i.e. not assuming a flat reflecting surface. In this case, the position-dependent surface displacement is given by

$$\Delta z_{SAW} = A_C \cos(\Omega t) \cos[K(x - x_0)] + A_S \sin(\Omega t) \sin[K(x - x_0)] , \quad (2.11)$$

which is the sum of two time-shifted standing waves, with peak displacement A_C and A_S respectively. The surface displacement written in this form is a superposition of traveling and standing waves along the x direction, depending on the amplitudes A_C and A_S . $K = 2\pi/\Lambda$ is the SAW wave number, Ω the angular frequency, and x_0 is the transverse position of the laser beam on the SAW device. We now carry out the calculations by considering this generic displacement, and in the end we can separate between the case of purely traveling waves by imposing $A_C = A_S = A_0$, and purely standing waves by imposing $A_S = 0$ and $A_C = A_0$. In this way, the standing waves are defined such that at position $x_0 = 0$, the laser beam is focused on an antinode, and where A_0 is the peak surface displacement. The field that couples back to the fiber is now given by

$$\begin{aligned} E'_{SAW} &= \iint E_{fiber}^* \times E_{SAW} dx dy \\ &= \iint E_{fiber}^2 \times \exp(-2ik\Delta z_{SAW}) . \end{aligned} \quad (2.12)$$

Due to the small SAW displacement, we can expand the exponential containing Δz_{SAW} , and we can ignore all terms containing $\sin(Kx)$ since they are even functions and their

integration is zero. The overlap integral therefore becomes

$$E'_{SAW} = \frac{2}{\pi w_0^2} \int \exp\left(-\frac{2y^2}{w_0^2}\right) dy \times \quad (2.13)$$

$$\times \int \exp\left(-\frac{2x^2}{w_0^2}\right) [1 - 2ik\gamma \cos(Kx)] dx ,$$

where $\gamma = A_c \cos(\Omega t) \cos(Kx_0) - A_s \sin(\Omega t) \sin(Kx_0)$. The integral can be solved by expanding the cosine term $\cos(Kx) = [\exp(iKx) + \exp(-iKx)]/2$, and using the standard integral:

$$\int_{-\infty}^{+\infty} \exp(-ax^2 + ibx) dx = \sqrt{\frac{\pi}{a}} \exp\left(-\frac{b^2}{4a}\right) . \quad (2.14)$$

The result is given by:

$$E'_{SAW} \simeq 1 + 2ik\gamma e^{-B} , \quad (2.15)$$

where $B = -K^2 w_0^2/8$. Similarly to what we did in Eq. 2.9, we calculate the total power at the photodiode, resulting in the interference of E'_{SAW} and E_{ref} :

$$P_{SAW} = 2 - 4\gamma e^{-B} + 4k^2 \gamma^2 e^{-2B} . \quad (2.16)$$

The Ω component of the optical power at the photodiode for a SAW displacement is given by

$$P_{SAW}^{\Omega} = 4k\gamma e^{-B} . \quad (2.17)$$

Now, before we calculate the rms value, we need to separate the case of traveling and standing waves: for traveling waves we impose $A_C = A_S = A_0$, which results in $\gamma = A_0[\cos(\Omega t) \cos(Kx_0) - \sin(\Omega t) \sin(Kx_0)]$. We then obtain $P_{tSAW}^{rms} = 4kA_0 \exp(-B)/\sqrt{2}$, where the subscript t stands for traveling. For the case of standing SAW waves, we impose $A_S = 0$ and $A_C = A_0$, obtaining $\gamma = A_0 \cos(\Omega t) \cos(Kx_0)$, and the rms change in the optical power is given by $P_{sSAW}^{rms} = P_{tSAW}^{rms} \times |\cos(Kx_0)|$, where the subscript s stands for standing wave. The measured rms change in the Ω component of the optical power caused by traveling SAWs is therefore equivalent to the one caused by standing SAWs, measured when the laser is on an antinode ($x_0 = 0$). By comparing this result with the rms change in the optical power caused by the displacement of a flat surface, we obtain the wanted reduction factor r :

$$r = \frac{P_{SAW}^{rms}}{P_{flat}^{rms}} = \exp\left(-\frac{K^2 w_0^2}{8}\right) \quad (2.18)$$

In our case $\Lambda = 2.8 \mu\text{m}$ and $w_0 = 1.4 \mu\text{m}$, resulting in $r = 0.29$, as shown in Fig. 2.5 where we plot the reduction factor and we show our experimental conditions. The total gain of the interferometer in Eq. 2.1 is therefore $\zeta = 0.154 \text{ pm}/\mu\text{V}$ rms.

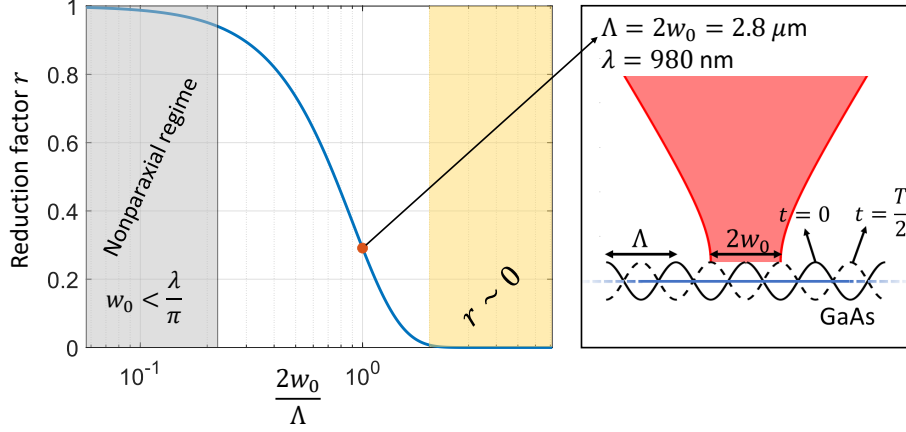


Figure 2.5: Reduction factor. The blue curve is the reduction factor from Eq. 2.2, as a function of the ratio between laser beam spot $2w_0$, and the acoustic wavelength Λ of SAWs. The red dot indicates our experimental conditions with $\Lambda = 2w_0 = 2.8 \mu\text{m}$, and optical wavelength $\lambda = 980 \text{ nm}$. The gray shaded area on the left with $w_0 < \lambda/\pi$ corresponds to the nonparaxial regime, where our calculation of the reduction factor is not valid. The yellow shaded area on the right with $2w_0/\Lambda > 2$, corresponds to a region where $r \sim 0$. In the right panel we show a sketch of the experiment. We show the surface profile at time $t = 0$ and $t = T/2$, corresponding to half the oscillation period of the standing waves.

2.5.2 Beam spot size measurement

As discussed in the main text, the sine-like shape of the displacement generated by a SAW affects the reduction factor $r = \exp(-K^2 w_0^2/8)$. Due to the exponential dependence on the beam waist radius, an accurate measurement of w_0 is crucial for a proper calibration of the measured voltage into a displacement.

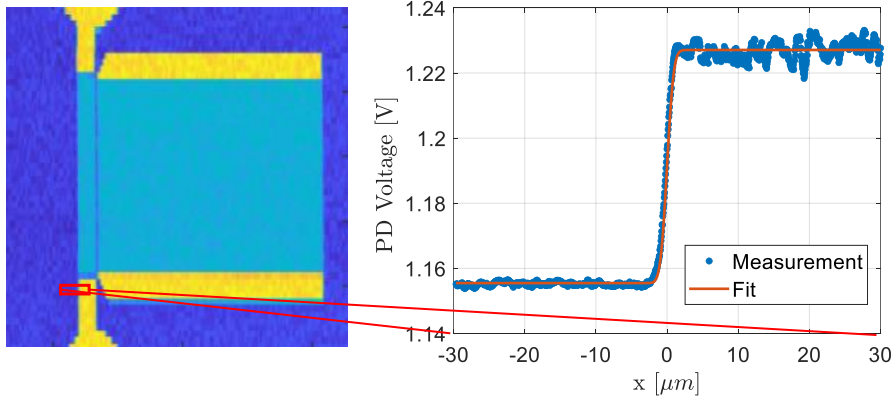


Figure 2.6: Measurement of the beam spot size with a variation of the knife-edge technique. Left panel: image of the IDT and Bragg mirror metal structure, obtained with the reference photodiode in Fig. 2.1 (b). Right panel: photodiode voltage (blue) as a function of x position, and fitted function (red), according to Eq. 2.19

We perform this measurement in-situ, using a variation of the knife-edge technique,

where we use as a knife edge the boundary between GaAs substrate and the metal contact pad of the SAW cavity IDT, since GaAs and aluminium have different reflectivities. We shine a focused laser beam on the sample, we move the sample along the x direction, and using the reference photodiode in Fig. 2.1 (a), we measure the reflected power over the boundary between GaAs and Al. An example of such measurement is shown in Fig. 2.6 In a reference frame where the boundary coincides with the origin of the x axis, the reflected power is

$$P = P_0[r_2 + r_1 + (r_2 - r_1) \times \text{erf}\left(\frac{x\sqrt{2}}{w_0}\right)], \quad (2.19)$$

where P_0 is the the optical power of the incident beam (in arbitrary units), r_1 is the reflection coefficient for GaAs, r_2 is the reflection coefficient for Al, and w_0 is the beam waist radius. In figure 2.6 is shown the region over which such measurement has been performed, the measured data and the fitting function. The fitted parameters are $P_0 = 1.75$, $w_0 = 1.4 \mu\text{m}$, $r_1 = 0.30$. The expected reflection coefficient of GaAs at $\lambda \simeq 1 \mu\text{m}$ is $r_{GaAs} = 0.3097$, which is in very good agreement with the fitted r_1 .

3 Investigation of spurious bulk acoustic waves in surface acoustic wave devices by acoustic fringe analysis

Full characterization of surface acoustic wave (SAW) devices is not trivial. We use an optical Michelson interferometer with spatial scanning capabilities, to characterize GHz SAW cavities on GaAs, and we analyze the acoustic field maps by 2-dimensional Fourier analysis of the acoustic interference fringes. While our experimental setup allows for simultaneous measurement of the amplitude and phase of the acoustic field, we show that amplitude-only measurements are sufficient to detect secondary effects such as the presence of spurious bulk acoustic waves. This is possible due to the interference of bulk waves with the surface waves, which leads to an acoustic-wavelength spatial periodicity in the amplitude of the acoustic field, distinct from the half-wavelength spatial periodicity of standing SAWs. By spatial Fourier filtering the images of the acoustic field, we are able to separate the distribution of surface and bulk waves across the SAW cavities, and to detect imperfections and impurities on the surface of the device.

This chapter is in preparation for submission: M. Fisicaro, T. A. Steenbergen, Y.C. Doedes and W. Löffler, Investigation of spurious bulk acoustic waves in surface acoustic wave devices by acoustic fringe analysis.

3.1 Introduction

High-frequency acoustic waves in solids are widely used in modern technologies: with a phase velocity 10^5 times smaller than the electromagnetic counterpart, acoustic waves have a shorter wavelength, in the order of μm at GHz frequencies, enabling miniaturization of signal-processing devices such as RF electronic filters [7, 8, 94, 95]. Depending on the specific type of acoustic waves employed, these devices can be separated in bulk acoustic wave (BAW) and surface acoustic wave (SAW) devices, based on the propagation of the acoustic waves in the bulk or surface of the material.

In recent years, high-frequency acoustic waves also became of interest in the field of quantum technology and research, due to their ability to couple to a variety of different quantum systems [20–25, 29, 69, 70]. Here SAWs have particular importance due to their intrinsic surface confinement, which allows them to travel long distances with little dissipation, enabling quantum protocols relying on itinerant phonons [38–40]. The coupling between phonons and quantum systems on the other hand relies on localized phonons, due to the enhanced interaction provided by the phonon confinement [29].

For this reason, among SAW devices, cavities are of great importance, and even though cavities with high quality factors have been demonstrated at cryogenic temperatures [23, 24, 96], their realization with a small mode volume has only recently been achieved [20, 28, 52, 97, 98]. For this purpose, all loss mechanism must be reduced, such as diffraction losses, material losses, and BAW scattering losses [29, 48–50]. The latter in particular poses a problem in the realization of high-Q, small mode-volume SAW cavities, and even if there are approaches to mitigate these losses, they can not always be avoided [29, 99, 100]. Excitation of spurious BAWs in SAW devices is a very well known problem, but its investigation is primarily done by means of all-electrical measurements [49, 50, 99, 101–103]. There are a few reports of direct observation of BAWs in SAW devices with optical probes, but only measuring the bottom or the side of the substrate [104, 105].

Here we report the observation of spurious BAWs in SAW devices, by optically imaging the out-of-plane displacement on the top surface of SAW cavity devices. This is easily possible with a setup that allows for simultaneous measurement of amplitude and phase of the acoustic field, but we show that amplitude-only measurements are sufficient to identify the presence of spurious BAWs. This is because the interference of bulk and surface waves, leads to an acoustic-wavelength spatial periodicity in the amplitude of the acoustic field, distinct from the half-wavelength spatial periodicity originating from standing SAWs.

We investigate GHz SAW cavities on (001)-cut GaAs, by using a Michelson interferometer with spatial scanning capabilities, to image the amplitude of the out-of-plane surface displacement across the whole device, obtaining an image of the distribution of the acoustic field. By using 2D Fourier analysis and filtering, we are able to separate the spatial distribution of the spurious bulk waves, from that of the surface waves, and to detect imperfection and impurities on the surface of the device. Furthermore, on top of the Rayleigh waves propagating along the [011] direction of the GaAs substrate, the analysis of the 2D Fourier transform also revealed the presence of pseudo (or leaky) surface waves along other directions, which are Rayleigh waves coupled to a transverse horizontal bulk wave [106–108], most likely originating from diffraction of the Rayleigh waves or scattering from impurities on the GaAs surface.

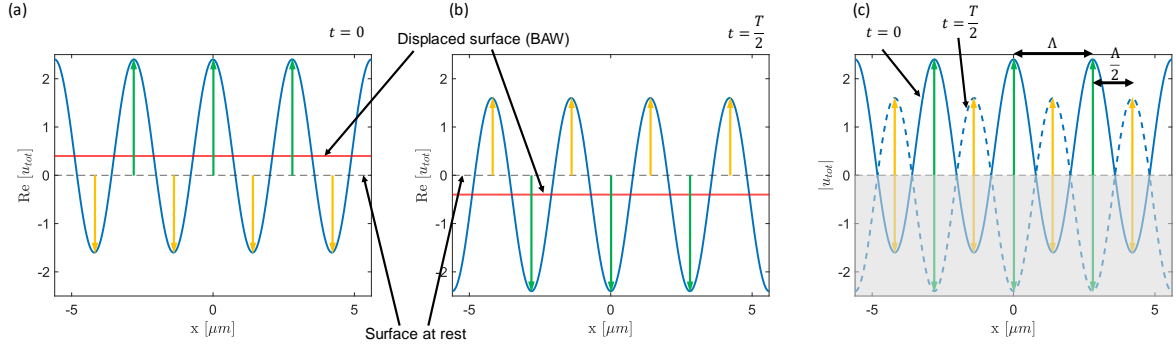


Figure 3.1: Interference of standing SAWs with BAWs. (a) Plot of the out-of-plane total displacement ($\text{Re}[u_{tot}]$) at time $t = 0$: the red line indicates the displaced surface caused by the BAW, and the blue line indicates the standing SAWs displacement, with respect to the displaced surface. The green (yellow) arrows indicate the distances of the oscillating surface from its rest position, showing an enhanced (decreased) displacement for the portion of the standing wave that is moving in phase (out of phase) with the bulk wave. (b) Plot of the out-of-plane total displacement ($\text{Re}[u_{tot}]$) at time $t = T/2$, corresponding to half oscillation. (c) Total surface oscillation at time $t = 0$ (full blue line), and at time $t = T/2$ (dashed blue line). The combination of these two lines in the non-shaded area, correspond to the absolute value of the total out-of-plane surface displacement. The green (yellow) arrows show the portion of the standing wave where the surface displacement is amplified (destructive) interference between the surface standing wave and the bulk wave, leading to a Λ -periodic modulation of the surface displacement. All plots are based on Eqs. 3.4, 3.5 with parameters $u_L = u_R = 1$, $u_B = 0.2$, $\varphi_L = \varphi_R = \varphi_B = 0$, $g(x) = 1$, and SAW wavelength $\Lambda = 2.8 \mu\text{m}$.

3.2 Interference of surface and bulk waves

We first study the combined surface displacement of surface and bulk acoustic waves: first we show how by measuring the complex displacement (amplitude and phase), we can easily separate SAWs and BAWs, then we show how, due to the interference of surface and bulk waves, an amplitude-only measurement is sufficient to identify the presence of spurious BAWs in a SAW device.

Let us start by considering the out of plane displacement generated by a combination of left and right traveling SAWs:

$$\begin{aligned} u_{left} &= u_L e^{i(Kx + \Omega t)} e^{i\varphi_L} \\ u_{right} &= u_R e^{i(-Kx + \Omega t)} e^{i\varphi_R}, \end{aligned} \quad (3.1)$$

where u_L (u_R) is the out-of-plane displacement amplitude, φ_L (φ_R) a generic phase term, $\Omega = 2\pi/T$ the angular frequency of the SAW, where T is the oscillation period, $K = 2\pi/\Lambda$ the wavenumber with Λ the SAW wavelength, and x is the direction along which the surface waves are excited. For the bulk waves, we assume that their amplitude is localized in a specific region of space and we write the out-of-plane displacement as

$$u_{bulk} = u_B g(x) e^{i\Omega t} e^{i\varphi_B}, \quad (3.2)$$

where u_B is the peak out-of-plane displacement amplitude, $g(x)$ is a continuous, non-diverging, non-periodic and slowly varying function of x , with values in the interval $g(x) \in [0, 1]$. The total out-of-plane displacement is given by

$$u_{tot}(x) = u_{left} + u_{right} + u_{bulk} \quad (3.3)$$

$$= e^{i\Omega t} \left[u_L e^{i(Kx + \varphi_L)} + u_R e^{i(-Kx + \varphi_R)} + u_B g(x) e^{-i\varphi_B} \right]. \quad (3.4)$$

Since the total displacement is a linear combination of the individual displacements of the different waves, and since the Fourier transform is a linear operation, the spatial Fourier transform of the demodulated total complex displacement at the frequency $f = \Omega/2\pi$ will show three peaks: a peak at the spatial frequency $f_x = 0$, corresponding to the bulk waves, a peak at spatial frequency $f_x = K/2\pi = 1/\Lambda$, corresponding to left-traveling SAWs, and a peak at spatial frequency $f_x = -1/\Lambda$, corresponding to right-traveling SAWs. This means that knowledge of the amplitude and phase of the total surface displacement, allows for the separation of SAWs and BAWs contributions. We now show that, to some extent, this is still possible with an amplitude-only measurement of the total surface displacement. The absolute value of the total out-of-plane displacement is $|u_{tot}(x)| = \sqrt{|u_{tot}(x)|^2} = \sqrt{u_{tot} \times u_{tot}^*}$, and can be written as

$$\begin{aligned} |u_{tot}(x)| &= \sqrt{|u_{DC}^2 + |u_{\Lambda/2}^2 + |u_{\Lambda}^2} \quad (3.5) \\ |u_{DC}^2 &= u_L^2 + u_R^2 + u_B^2 g^2(x) \\ |u_{\Lambda/2}^2 &= 2u_L u_R \cos(2Kx + \varphi_L - \varphi_R) \\ |u_{\Lambda}^2 &= 2u_B g(x) [u_L \cos(Kx + \varphi_L - \varphi_B) + u_R \cos(Kx - \varphi_R + \varphi_B)] . \end{aligned}$$

In the equation above we have split the absolute value into three terms: a DC-term with spatial frequency $f_x \sim 0$, a $\Lambda/2$ -term with spatial frequency $f_x = 2K/2\pi = 2/\Lambda$, and a Λ -term with spatial frequency $f_x = K/2\pi = 1/\Lambda$. The DC term $|u_{DC}^2$ denotes the non-periodic term: depending on the particular function $g(x)$, this term is not necessarily constant in x , but can slowly vary. The DC-term is present whenever there is at least one of the displacement components of Eqs. 3.1 and 3.2. The $\Lambda/2$ -term $|u_{\Lambda/2}^2$ represents the usual standing wave pattern given by the interference of a left and right traveling SAWs, and shows a periodicity in x equal to $\Lambda/2$, which is the distance between two adjacent nodes or antinodes. The Λ -term $|u_{\Lambda}^2$ is a Λ -periodic modulation caused by the interference between left/right traveling waves and the bulk waves, and it is an unequivocal sign of the presence of bulk acoustic waves. The operation of taking the absolute value therefore has the effect of mixing the DC spatial frequency of the complex BAW displacement with the spatial frequencies $f_x = \pm 1/\Lambda$ of the traveling SAWs, leading to the appearance of the two BAWs sidebands in the displacement amplitude, at frequencies $f_x = \pm 1/\Lambda$.

Eq. 3.5 is very generic, and depending on the choice of the parameters $u_L, u_R, u_B, \varphi_L, \varphi_R, \varphi_B, g(x)$ it describes different situations. Let's briefly investigate some of these cases by assuming $\varphi_L = \varphi_R = \varphi_B = 0$, and $g(x) = 1$. For pure BAWs, or traveling SAWs, only one of the amplitudes u_L, u_R, u_B is different than zero, resulting in a pure DC-component. For pure standing SAWs, $u_L = u_R$ and $u_B = 0$, resulting only in a $\Lambda/2$ -component. For pure right (left) traveling SAWs interfering with BAWs, $u_L = 0$ ($u_R = 0$) and $u_B \neq 0$, resulting in a DC-term and a Λ -term. Finally for standing SAWs interfering with BAWs, we have $u_L = u_R, u_B \neq 0$, resulting in $\Lambda/2$ periodic standing wave pattern, where the height of the antinodes is modulated with a spatial periodicity of Λ . This effect is visible because some portions of the standing SAW are in phase with the BAW, and some other

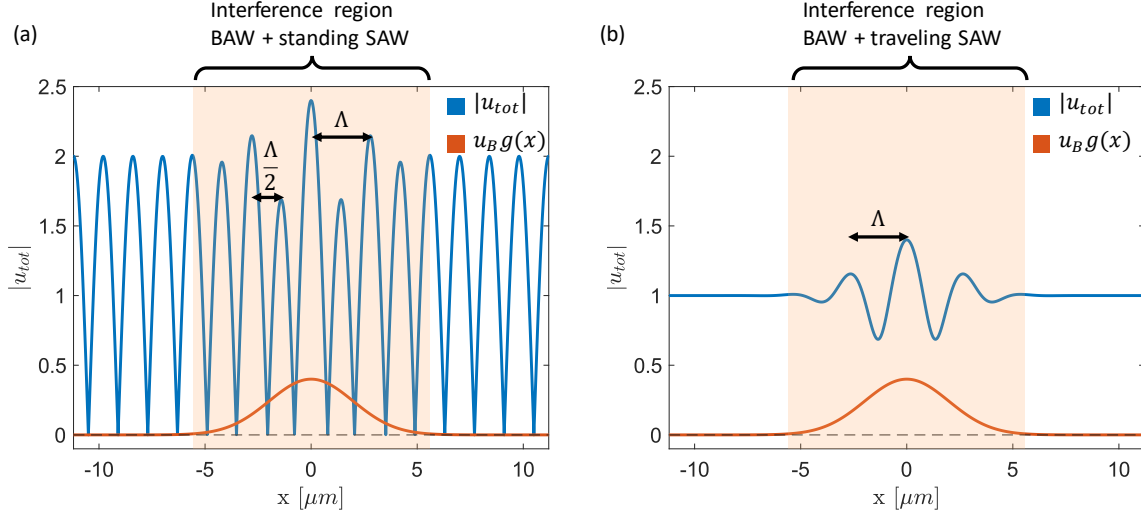


Figure 3.2: Localized SAW-BAW interference. Here we show the effect of introducing localization in Eq. 3.5: as an example we choose $g(x) = \exp(-x^2/\Lambda^2)$, where $\Lambda = 2.8 \mu\text{m}$ is the SAW wavelength. (a) shows the interference between standing surface waves ($u_L = u_R = 1$) and bulk waves ($u_B = 0.4$). (b) shows the interference between traveling surface waves ($u_L = 0, u_R = 1$) and bulk waves ($u_B = 0.4$). In both (a) and (b), all phases are set to zero ($\varphi_L = \varphi_R = \varphi_B = 0$).

portions are out of phase, leading to constructive or destructive interference, as shown in Fig. 3.1. This is not true anymore if we re-introduce the phase terms, with $\varphi_L = \varphi_R$ and $\varphi_B = \varphi_R + (m + 1)\pi/2$, where m is an integer: in this situation the bulk wave has a $\pi/2$ phase shift with respect to the standing surface wave, and even if both waves are present, there is no interference and therefore no Λ -term in the amplitude of the out-of-plane displacement.

Normally, in surface acoustic wave devices, spurious bulk waves are not excited uniformly along the whole device, but originate from localized scatterers which scatter SAWs into bulk waves. In our mathematical model, this is taken into account by the function $g(x)$ that determines the spatial profile of the out-of-plane surface displacement caused by the bulk wave. In Fig. 3.2 we show the localization of the surface-bulk wave interference for a bulk wave with Gaussian surface-profile $g(x) = \exp(-x^2/\Lambda^2)$, both for standing (a) and traveling (b) surface waves, representing the interference pattern that we expect to see for a scatterer with size of the order of the acoustic SAW wavelength Λ .

3.3 Acoustic fringe analysis

Now we validate the model introduced above by investigating the BAW-SAW interference in surface acoustic wave cavities. First we measure the acoustic field distribution across the device, and by Fourier analysis and filtering of the Λ -periodic spatial component, we are able to identify the presence of BAWs, and locate the region of the SAW device where the BAWs are excited.

In particular we investigate two planar SAW cavities with identical configurations, but different cavity lengths, metal thickness and composition. These cavities have been nanofabricated via e-beam lithography and e-beam evaporation of aluminium on a (001)-cut GaAs substrate. Both cavities consist of an IDT with 10 metal finger pairs, and two

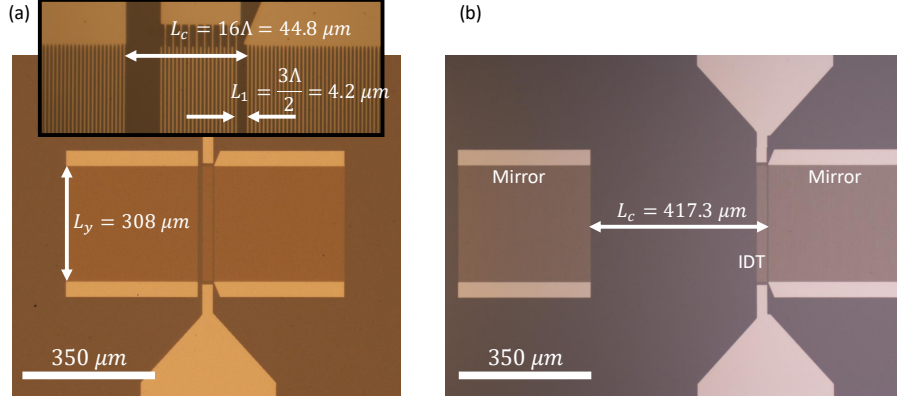


Figure 3.3: Optical microscope images of the short (a) and long (b) cavities. The geometrical cavity length L_c of the short cavity is a multiple integer of $\Lambda/2$, where Λ is the acoustic wavelength at which the cavity is designed to operate. This condition is not satisfied for the long cavity.

metal-grating acoustic mirrors with 250 metal fingers each, with a center-to-center finger spacing of $p = 1.4 \mu\text{m}$, and finger width of $d = 700 \text{ nm}$. The length of the fingers on the transverse direction is $L_y = 308 \mu\text{m}$, and the two cavities are both oriented along the $[110]$ direction, for which the speed of the Rayleigh wave is $v_{SAW} \simeq 2860 \text{ m/s}$, resulting in an acoustic wavelength $\Lambda \simeq 2.8 \mu\text{m}$ at the design frequency $f_{SAW} \simeq 1.02 \text{ GHz}$.

The two cavities have different geometrical cavity length of $L_c = 471.3 \mu\text{m}$ for the long cavity, and $L_c = 16\Lambda = 44.8 \mu\text{m}$ for the short cavity. These distances are measured between the centers of the first metal fingers of the 2 mirrors, and while for the short cavity it is a multiple integer of $\Lambda/2$, this is not true for the long cavity. The distance between the IDT and the adjacent mirror is $L_1 = 3\Lambda/2 = 4.2 \mu\text{m}$ for both cavities, also measured between the centers of the metal fingers. For the short cavity we evaporated a 10 nm adhesion layer of Ti, followed by 80 nm of Al, and finally another 10 nm of Ti, for a total metal height of $h = 100 \text{ nm}$. For the long cavity we only evaporated $h = 50 \text{ nm}$ of Al, without any adhesion or top layer; the absence of these two layers does not affect the operation of the cavity. Fig. 3.3 shows microscope pictures of the short (a) and long (b) SAW cavities used in this experiment.

Using the optical scanning Michelson interferometer described in detail in the previous chapter, we image the acoustic field distribution in both the long and short cavities, and we now analyze these measurements by means of 2D Fourier analysis.

3.3.1 Long SAW cavity

We drive the IDT at the resonant frequency of the SAW cavity $f_0 = 1.021965 \text{ GHz}$ and we image the acoustic field distribution. In Fig. 3.4 (a) we show the amplitude of the out-of-plane displacement. In the left inset we show a cross section of the measurement in the middle of the cavity, where standing waves are visible, with antinodes equally spaced at a distance of $\Lambda/2$. In the right inset we show a cross section of the acoustic field inside the mirror. Next to the exponential decay, we observe also a modulation in the height of the antinodes, with a spatial periodicity of Λ , as predicted by our model.

In Fig. 3.4 (b) we show the 2D Fourier transform of the amplitude of the out-of-plane displacement measured in (a). On the f_x axis, we observe two peaks at the spatial frequencies $f_x = 1/\Lambda = 0.357 \mu\text{m}^{-1}$ and $f_x = 2/\Lambda = 0.714 \mu\text{m}^{-1}$, corresponding to a Λ

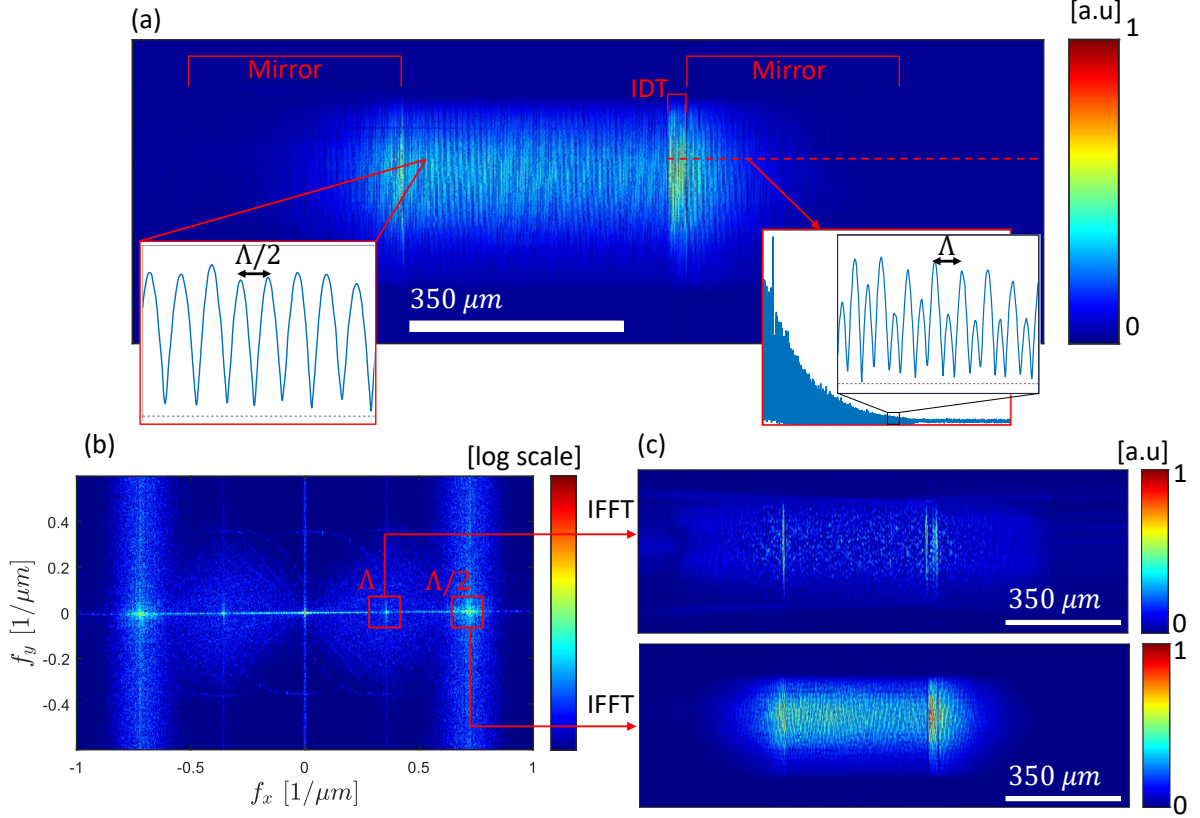


Figure 3.4: Acoustic field distribution in the long cavity. (a) Image of the SAW cavity, showing the amplitude of the out-of-plane displacement. The inset on the left shows a cross section of the standing wave field inside the cavity. The inset on the right shows a cross section of the exponentially decaying field inside the acoustic mirror, where the standing wave pattern is now modulated in amplitude by the BAWs. (b) 2D Fourier transform of (a), showing two peaks at the spatial frequencies $f_x = 0.357 \mu\text{m}^{-1}$ and $f_x = 0.714 \mu\text{m}^{-1}$, corresponding to a Λ and $\Lambda/2$ periodicity in the real space. (c) Fourier filtered images obtained from (b) by selecting only the Λ -term (top image) and the $\Lambda/2$ -term (bottom image) in the Fourier spectrum.

and $\Lambda/2$ periodicity in real space. There is also a DC term, which is caused partially by spurious BAWs and partially by the presence of spurious traveling SAWs, resulting from the finite reflectivity of the SAW mirrors. Finally we note that the Fourier transform shown here is limited to the spatial frequency range $f_x = [-1, 1] \mu\text{m}^{-1}$, and that there are other peaks along the f_x axis at higher spatial frequencies, corresponding to the harmonics of $f_x = 2/\Lambda$, since we are analyzing here the amplitude of the out-of-plane displacement $|u_{tot}(x)| = \sqrt{|u_{tot}(x)|^2}$.

In the 2D Fourier transform, we select the peaks corresponding to the spatial frequencies $f_x = \pm 1/\Lambda$ by applying two narrow square box functions as a mask, and we compute the inverse 2D Fourier transform, obtaining a real-space image of the spatial distribution of the Λ -periodic term. The top image in fig. 3.4 (c) shows the result of this process, while the bottom image shows the spatial distribution of the $\Lambda/2$ -periodic term, resulting from Fourier filtering the $f_x = 2/\Lambda$ spatial frequency. While the latter strongly resembles the original image (a), the Λ -periodic component shows high amplitude in the SAW cavity, at

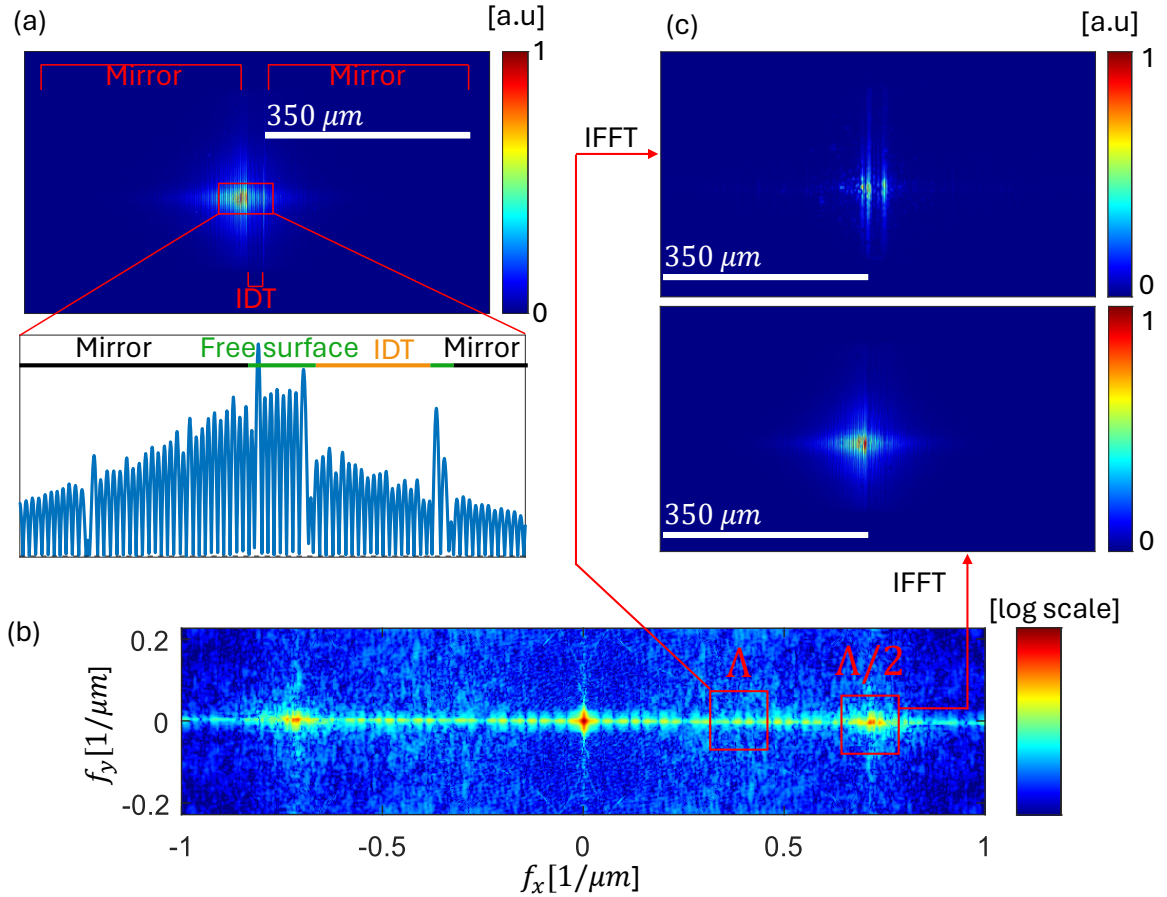


Figure 3.5: Acoustic field distribution in the short cavity, when driven at its resonance frequency. (a) Amplitude of the out-of-plane displacement. In the inset we show the cross section of the acoustic field in the middle of the cavity. We indicate in black the position of the mirrors, in green the position of the free GaAs surface, and in yellow the position of the IDT. (b) 2D Fourier transform of (a), where the peak corresponding to the $\Lambda/2$ term is visible, while there is no visible peak corresponding to the Λ -term. Fourier filtered images obtained from (b) by selecting only the Λ -term (top image) and the $\Lambda/2$ -term (bottom image) in the Fourier spectrum.

the line boundaries between free GaAs and the metal grating of the mirrors and IDT. In addition to this, there are several high-amplitude spots, and a low-amplitude background across the whole SAW cavity.

3.3.2 Short SAW cavity

The resonance frequency of the short cavity is found to be $f_0 = 1.0107$ GHz. We drive the IDT at this frequency and we measure the amplitude of the out-of-plane displacement, as shown in Fig. 3.5 (a). In the inset we show a cross section in the middle of the cavity. The asymmetry in the amplitude of the field in the left and right mirror is most likely to be attributed to the small gap between the IDT and the right mirror, but a rigorous analysis of this requires a TMM (transfer matrix method) calculation of the field in the Bragg grating.

In Fig. 3.5 (b) we show the 2D Fourier transform of the surface displacement, where now

the peak corresponding to the Λ -component is not visible. Nevertheless, as described for the long cavity, we Fourier filter the spatial frequencies corresponding to the Λ -periodicity and to the $\Lambda/2$ -periodicity, and we show the result in Fig. 3.5 (c). The results are similar to the long cavity, where the spatial distribution of the $\Lambda/2$ -component mirrors the non-filtered surface displacement. The Λ -component, however, only shows as bright lines inside the SAW cavity, in correspondence of the interfaces between free surface and metal structures.

As a final experiment, we drive the short SAW cavity at the frequency $f = 0.995$ GHz, which is outside of the stopband of the mirrors. The idea is that in this situation the surface acoustic waves are mainly not confined in the cavity, but traveling.

In Fig. 3.6 (a) we show the image of the measured surface displacement (top), and a cross section (bottom) taken at the transverse position indicated by the dashed line. Now the presence of the traveling waves is clear as indicated by the significant DC offset in regions (i) and (iv), corresponding to the free surface outside of the cavity. The regions (ii) and (iii), corresponding to the mirrors, IDT and cavity, show the presence of a spurious resonant mode. This is a weak resonance, as visible by the strong DC component, and most likely appears because we are driving at a sideband of the Bragg mirror. The amplitude asymmetry between the left and right side of the cavity is probably connected to the small gap between the IDT and the right mirror. Fig. 3.6 (b) shows the 2D Fourier transform, where now the peak corresponding to the Λ -periodicity is clearly visible.

In Fig. 3.6 (c) we show the Fourier-filtered images, showing the spatial distribution of the Λ -component (top) and $\Lambda/2$ -component (bottom). Off-resonance, the surface waves travel through the mirrors almost unaffected, and this shows in the filtered image, where the Λ -component now has bright lines at all the interface between metal and free-surface, also the ones outside of the cavity. BAW scattered from point-like centers are now also visible, and, across the whole device, a faint Λ -component indicates the presence of BAW interfering with traveling surface waves.

3.3.3 Discussion

We now first discuss the images corresponding to the Fourier-filtered Λ -component in Figs. 3.4,3.5,3.6 (c): all of them show strong signals at the interfaces between metal structures and free GaAs surface. This is explained by the theory of SAW reflection by a periodic grating: upon incidence of a SAW on a periodic structure, the single elements of the grating not only reflect the surface waves, but also scatter them into bulk acoustic waves.

In our case the cavity is operated at its fundamental resonance frequency, therefore only the grating elements close to the edges of the metal structure, scatter surface waves into propagating bulk waves. Inside the grating, and far from the edges, BAWs are still excited by each individual grating element, but they interfere and cancel each other out, resulting in no propagation inside the bulk [101–103]. This is precisely what we observe in the Λ -filtered images, and in particular Fig. 3.6 (c) shows that when driving the short SAW cavity off-resonance, also the edges of the mirrors at the outer side of the cavity scatter BAWs since now the surface wave are not reflected and can travel through the mirrors.

In the same images, we observe high-amplitude points, appearing to be randomly distributed. These points, some of which are encircled as an example in Fig. 3.6 (c), correspond to particles on the GaAs surface or defects in the mirrors, which scatter surface

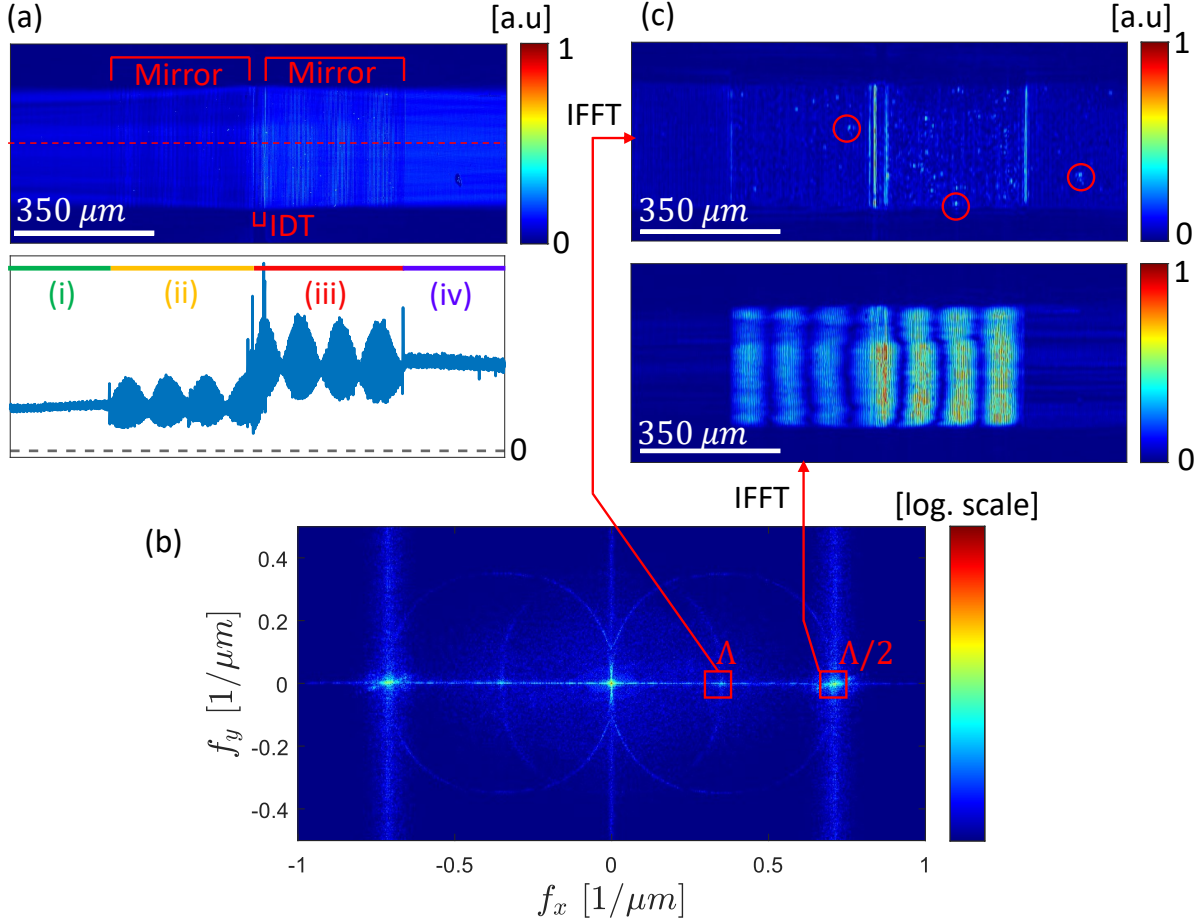


Figure 3.6: Acoustic field distribution in the short cavity, driven at a non-resonant frequency. (a) Amplitude of the out-of-plane displacement with a cross section of the acoustic field. The 4 regions (i) - (iv) highlight areas with different acoustic field distribution, and are discussed in the main text. (b) 2D Fourier transform of (a). (c) Fourier filtered images obtained from (b) by selecting only the Λ -term (top image) and the $\Lambda/2$ -term (bottom image) in the Fourier spectrum.

waves, partially also into the bulk. Finally in the long cavity, and in the off-resonance measurement of the short cavity, we also observe a low-intensity Λ -periodic background, across the whole SAW cavity. We attribute this to BAWs originating from the surface scattering points mentioned above, propagating inside the bulk GaAs, and reflected from the bottom surface of the wafer. It is not fully clear why this background is not present in the short cavity, when driven at resonance.

For the short cavity driven off-resonance, we compare the 2D Fourier transform of the complex out-of-plane displacement, with the Fourier transform of the amplitude of the out-of-plane displacement, as shown in Fig. 3.7 (a) and (b). As explained in section II, the bulk waves correspond to a peak at zero spatial frequency in the Fourier transform of the complex displacement. Taking the amplitude of the displacement mixes the $f_x = 0$ periodicity of the bulk waves, with the $f_x = \pm 1/\Lambda$ periodicity of the left (right) traveling waves, effectively creating two sidebands in the displacement amplitude, as indicated by the red arrows in Fig. 3.7 (a) and (b). In Fig. 3.7 (c) we show the Fourier filtered displacement amplitude, obtained by selecting a small region around $f_x = 0$ in the Fourier

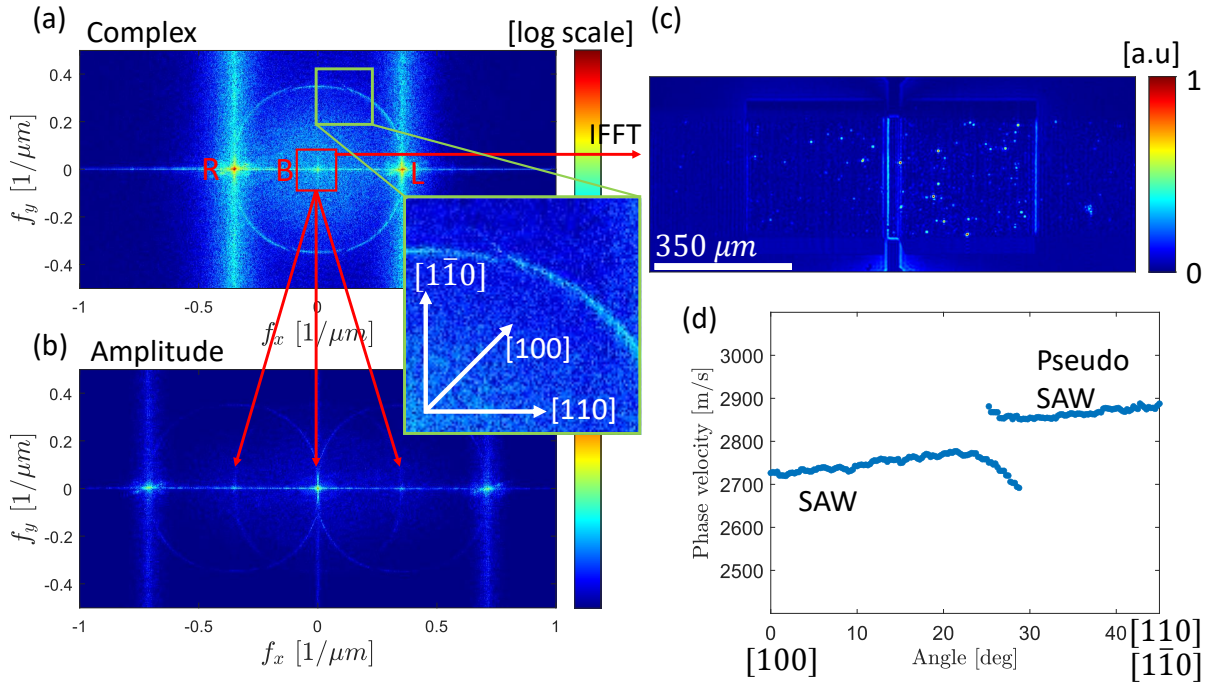


Figure 3.7: Comparison between Fourier transform of the complex displacement, and Fourier transform of the displacement amplitude, for the short cavity driven off-resonance. (a) Absolute value of the 2D Fourier transform of the complex displacement (amplitude and phase), with two peaks at the spatial frequencies $f_x = \pm 1/\Lambda$ corresponding to left and right traveling waves, and a peak at $f_x = 0$, corresponding to the bulk waves. (b) 2D Fourier transform of the amplitude of the displacement. We can see here a ‘splitting’ of the peaks corresponding to the bulk waves, as indicated by the red arrows. (c) Fourier filtered displacement amplitude, obtained from (a) by selecting only the spatial frequencies around $f_x = 0$. (d) Measured phase velocity as a function of the propagation angle, obtained from the Fourier transform in the inset of (a).

transform of the complex displacement. By comparison with the Filtered image obtained from the Fourier transform of the displacement amplitude, in Fig. 3.6 (c), we see that the two are equivalent, with only a difference in the intensities.

Finally we investigate the circular signal in the Fourier transform, as visible in the inset of Fig. 3.7 (a). We note that in the Fourier transform, the f_x axis in the Fourier transform correspond to the [110] direction and the f_y axis to the $[1\bar{1}0]$ direction, but the two are equivalent due to the symmetry in the crystalline structure of GaAs. The direction at 45° from both the f_x and f_y axis is the [100] direction. The following analysis on the circular signal is done by considering the portion of the circle between the [100] and $[1\bar{1}0]$ directions, because here the circular signal is clearly visible, as opposed to the [110] direction, where it is covered by the strong SAWs component that travels on the excitation axis. Due to the equivalence between the $[1\bar{1}0]$ and [110] axis, in the following we will only refer to the [100] direction.

The circular signal in the Fourier transform corresponds to surface acoustic waves traveling off-axis with respect to the [110] direction along which the waves are excited. The presence of these off-axis propagating waves can be attributed partially to diffraction, and partially to scattering by impurities on the surface of the GaAs substrate.

By analyzing the circle, and converting it into an acoustic wavelength as a function of the angle of the propagating direction $\Lambda(\theta)$, we can calculate the phase velocity of the surface acoustic wave $v_{SAW}(\theta) = f_0 \times \Lambda(\theta)$, where $f_0 = 0.995$ GHz is the excitation frequency. The result is shown in Fig. 3.7 (d), and shows the presence of two different kind of waves with different phase velocities, which branch out at an angle of about $25^\circ - 30^\circ$, from the [100] direction, which is at an angle of 45° from [110], the direction of excitation of the IDT transducer. The bottom branch is associated with a Rayleigh-type surface acoustic waves, while the top branch is a pseudo surface acoustic wave, which correspond to a Rayleigh wave coupled to a transverse horizontal bulk wave [106–108]. At the [110] direction the excited wave is a pure Rayleigh wave.

We note that in our measurement, the two branches stop at the branching point. The pure SAWs can in principle exist also at higher angles (measured from the [100] direction), but in our measurement are not detected due to their low amplitude. On the other hand, the pseudo SAW is not present at low angles, because the Rayleigh wave component disappears, leaving only the transverse horizontal bulk wave. The latter does not have an out-of-plane displacement component, and therefore is not directly detectable with our interferometer. Even if the amplitude of this transverse horizontal bulk wave is generally low, we hypothesize that the metal structures of the SAW cavity can partially scatter this wave into bulk waves with an out-of-plane component, and therefore be detected as a bulk wave in our interferometric measurements.

3.4 Conclusions and outlook

We have shown the power of analyzing spatial Fourier transforms of surface displacement in SAW devices. In particular we focused on the analysis of the acoustic fringes caused by interference of bulk and surface waves which, experimentally, only requires imaging the amplitude of the surface displacement, avoiding the technical complications of implementing phase detection at GHz frequencies.

Despite this method is only qualitative, since it can not measure the absolute amplitude of the bulk waves, it can be very useful in identifying the presence of unwanted bulk waves in surface acoustic wave devices, or equivalently unwanted surface waves in bulk acoustic wave devices. In SAW cavities, unwanted BAWs are scattered by edge discontinuities in the acoustic mirrors, creating losses in the surface acoustic wave cavity-mode. This is normally a secondary effect, since there are other loss mechanisms that are predominant, however it becomes important in high-Finesse SAW cavities where all other loss-mechanism are minimized, in particular if the cavity is operated at cryogenic temperatures.

This regime is of great importance for example in telecommunications and quantum technologies, and our novel method can potentially play an important role in reducing BAW losses in SAW cavities, increasing their finesse and providing better GHz electrical filters, or increasing the coupling between SAW phonons and quantum systems.

4 Observation of the optical Talbot effect from a surface acoustic wave dynamic grating

We demonstrate the dynamical Talbot effect caused by optical diffraction from standing surface acoustic waves. The Talbot effect is a wave interference phenomenon in the Fresnel regime, and we observe it by optically imaging 1 GHz (standing) surface acoustic waves with a fiber-based optical interferometer. By studying the interferometric signal at 1 GHz, we first discover the existence of an amplitude-modulated term, that can exceed in magnitude the usual phase-modulated term, enabling a new way of imaging surface acoustic waves. Secondly, we reveal with this method the Talbot effect, where a modified Talbot length appears. As a consequence, the amplitude modulation vanishes at periodic positions.

This chapter is based on M. Fisicaro, Y.C. Doedes, T. A. Steenbergen, M. P. van Exter and W. Löffler, Observation of the Talbot effect from a surface acoustic wave dynamic grating, arXiv:2409.11161 (submitted).

4.1 Introduction

The Talbot effect is a wave interference phenomenon in the Fresnel regime by diffraction of a plane wave by a periodic structure such as a grating. Upon diffraction of the wave by the grating, periodic images of the grating appear at specific distances; this phenomenon is also known as lensless imaging or self-imaging [109–111]. The Talbot effect was firstly discovered in optics in 1836 by Henry Fox Talbot [112], but it was Lord Rayleigh who quantitatively explained it in 1881 [113]. Four years later, Lord Rayleigh made another important scientific contribution by predicting the existence of a particular type of surface acoustic waves, characterized by an elliptical motion of the surface [1]. In his paper, he accurately predicted that these waves have a significant role in earthquakes and the collision of elastic solids, and they were later named Rayleigh waves in his honor. For about 140 years, these two physical phenomena have not been connected: despite the Talbot effect has been observed in many different systems [114–120], to the best of our knowledge, it has never been observed as a consequence of optical diffraction from Rayleigh waves.

In this study we demonstrate this phenomenon through optical imaging of standing Rayleigh waves, which, from now on, we will generically refer to as standing surface acoustic waves (SAWs).

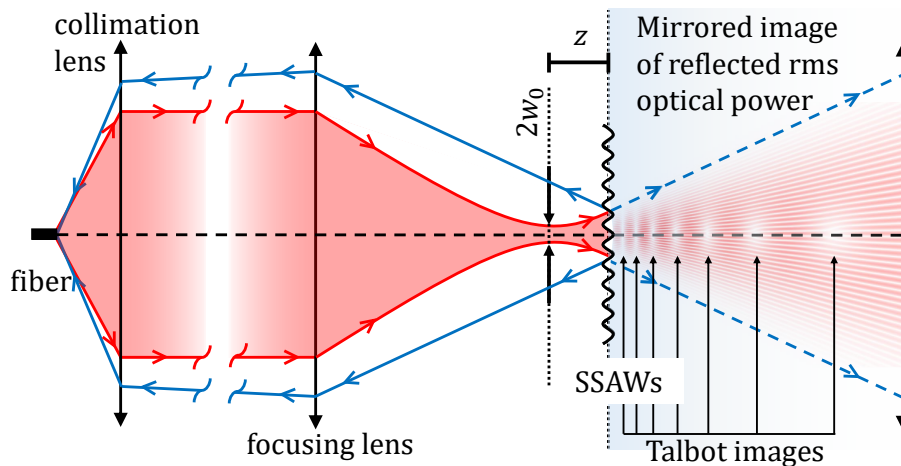


Figure 4.1: Sketch of the experiment: laser light from a single mode fiber is first collimated and then focused onto a partially reflecting surface on which standing surface acoustic waves (SSAWs) are excited. The incident light is reflected back, for clarity we plot here its mirrored image to the right of the reflecting surface. If the position of the beam waist z is displaced with respect to the reflecting surface, so that the light beam illuminates multiple periods of the oscillating surface grating, the Talbot effect can be observed where self-images of the field at the grating are reproduced in the near field at specific locations away from the grating. Here the self images are visible as regions of zero power on the right of the grating, where we have plotted the rms optical power of the reflected diffracted beam.

Surface acoustic waves (SAWs) can be excited using an interdigital transducer (IDT) [41,61,121] on the surface of a piezoelectric substrate at frequencies up to a few GHz, which for most materials corresponds to acoustic wavelengths down to the sub-micrometer range

[6,122–124]. If confined in an acoustic Fabry-Perot cavity [24,29,52,71–73,96,125] standing SAWs appear. This results in a surface that behaves as an oscillating surface grating, and can therefore dynamically diffract an optical beam upon reflection, by spatial phase modulation. In our case, we use a fiber-based scanning optical Michelson interferometer to image the displacement generated by 1 GHz SAWs. For spatially-resolved interferometric imaging of the SAWs, this diffraction is in principle an unwanted but unavoidable effect since at this frequency, the acoustic wavelength $\Lambda = 2.8 \mu\text{m}$ and the beam spot size of the focused laser beam $2w_0 = 2.8 \mu\text{m}$ (for $\lambda = 980 \text{ nm}$ and 0.55 NA) are comparable in size.

In our experiment, we were originally interested in the optical phase modulation induced by the SAWs, but we found that the interferometric signal consists of both a phase modulation term, and of an amplitude modulation term that appears due to mode filtering by the single-mode optical fiber. In this paper, we theoretically and experimentally demonstrate that the amplitude modulation term is zero when the laser beam is precisely focused on the surface of the SAW device, due to the symmetry of the optical phase modulation with respect to the focal position of the laser beam. Additionally, this amplitude modulation term is also zero at periodic defocusing distances due to the interference between the directly reflected beam and the beams diffracted by the oscillating grating. This phenomenon can be better understood through the Talbot effect under Gaussian beam illumination.

When a grating is illuminated by a Gaussian beam, rather than a plane wave, the Talbot effect still occurs but with two notable differences (see Fig. 4.1) : first, the position of the self-images depends non-linearly on the distance z from the grating, and second, the self-images are magnified, with the magnification factor also varying non-linearly with z [126]. For each defocusing distance, the position and magnification of the self-images change, changing the Talbot pattern. Remarkably, we find that when the defocusing distance is an integer multiple of the usual Talbot length $z_T = 2\Lambda^2/\lambda$, the resulting Talbot patterns have a self-image located at the focal position of the fiber, leading to periodically spaced zeros in the amplitude modulation.

4.2 Experimental setup

The experimental setup shown in Fig. 4.2 (a) is a Michelson interferometer implemented with a polarization-maintaining single-mode fiber coupler as the beam splitter (PM BS). Narrow-linewidth laser light enters the fiber coupler through port A and is split into the sample (D) and reference arm (C). In the reference arm, the light is focused onto a mirror by a single aspheric lens and back-reflected into the fiber. In the sample arm (D), light is first collimated by an aspheric lens, and then strongly focused onto the GaAs-based SAW device with an aspheric lens with 0.55 NA, resulting in a beam waist radius $w_0 = 1.4 \mu\text{m}$.

The GaAs surface acts as a partial mirror due to Fresnel reflection, and the reflected light is coupled back into the single-mode fiber using the same port D. The reflected light from the reference and sample arm of the interferometer is then recombined through the same fiber splitter, and exits through port B. For the SAW device, we nanofabricated on a GaAs substrate a surface acoustic wave (SAW) Fabry-Perot cavity, where surface acoustic waves are excited by an interdigital transducer (IDT) embedded inside the resonator (see inset in Fig. 4.2 (b)). In this way we can generate standing surface acoustic waves (SAWs) with a frequency of about 1 GHz, and a wavelength $\Lambda = 2.8 \mu\text{m}$. These waves change the optical path length in the sample arm of the interferometer, generating an interferometric signal at 1 GHz which is detected with a fast photodiode.

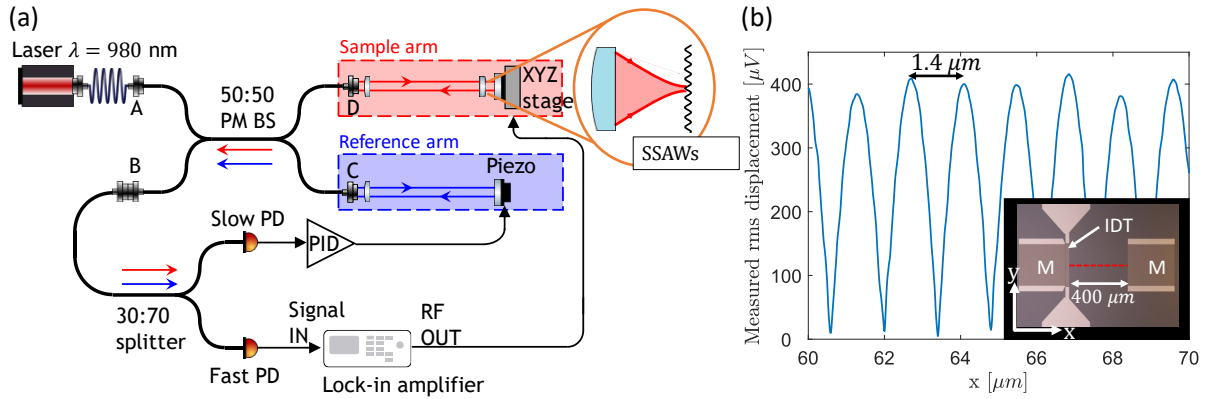


Figure 4.2: (a) Scheme of our experiment, a fiber-based Michelson interferometer using single-mode polarization-maintaining fibers, as described in the main text. (b) Microscope image (inset) of the SAW cavity showing the IDT and the SAW mirrors (M), and standing wave pattern measured along a short section of the dashed red line.

The interferometer is stabilized by a piezo actuator on which the mirror of the reference arm is mounted and a PID controller. The error signal is provided by the slow photodiode, and the PID controller is set to lock the interferometer to the side of an interference fringe. The SAW device is mounted on a three-axes nanopositioning stage, where translation along the optical (z) axis allows to adjust the focus of the laser beam, while the x and y axes allow us to scan the laser focus over the SAW device, in order to reconstruct an image of the out-of-plane displacement of the SAW device. Fig. 4.2 (b) shows a microscope image of the SAW device, and a cross-section along the x -direction of the standing acoustic waves, as indicated by the red line, with the laser focus exactly at the sample plane. Since we are plotting the rms amplitude of the measured displacement, the spatial periodicity is $\Lambda/2 = 1.4 \mu\text{m}$.

This measurement was taken with a locked interferometer, but we have found that even if the reference arm of our interferometer is blocked, we can sometimes observe the SAW signal very clearly. This is because on top of the usual optical phase changes induced by the standing SAWs, the coupling to the single mode fiber (port D) also changes the optical power by spatial mode filtering of the reflected light, effectively converting phase changes induced by the SAW into changes of the optical power coupled back into the fiber. We refer to this effect as amplitude modulation. Thus, the measurement shown in Fig. 4.2 (b) can be taken even by only using the sample arm of the interferometer, and it shows the same periodicity but different amplitude. However, it is important to notice that for this to happen, we need to defocus the device from the laser focus, because exactly in the focus the 1 GHz amplitude modulation is zero, due to the equal symmetry of the standing SAWs and the optical phase around the beam focus. As we will show later, we also expect a very weak 2 GHz amplitude modulation, but we intentionally limit our detection bandwidth to around 1 GHz.

4.3 Amplitude and phase modulation

We now present an analytical model that describes the interferometric signal for the fiber-based Michelson interferometer. In particular we will show how the interferometric signal

is affected by the optical wavelength λ , the SAW wavelength Λ , and the Gaussian beam radius at the GaAs surface w . We will show analytically that the interferometric signal contains an amplitude modulation term that persists also when the reference arm of the interferometer is blocked. Finally we will compare the analytic results to our experimental data, and we will show how both are a consequence of the Talbot effect.

4.3.1 Complex collection ratio

With Fig. 4.2 (a) in mind, let us consider what happens in the sample arm of the interferometer: light from a single mode fiber is imaged and focused onto a reflecting SAW device. The reflected light follows the same path in reversed direction and is collected by the same fiber. The same happens in the reference arm, and the two beams coming from the two arms of the interferometer are then recombined in the fiber beam splitter and interfere at the fast photodiode, which measures the intensity of the light. The standing SAWs induce time-periodic variations of the local curvature of the reflected light, leading to 1 GHz modulation of the amplitude and phase of the light in the single-mode fiber. Importantly, we not only consider that the SAW device is in-focus, but discuss the generic case where the focus is at distance z from the SAW device. Since we use linearly polarized light and the fiber coupler is polarization maintaining, it is sufficient to use scalar fields for the input field E_{in} , the collected field E_{col} , and the reference field E_{ref} . We introduce the complex collection ratio

$$\alpha(t) = \frac{E_{col}(t)}{E_{in}}, \quad (4.1)$$

which is a measure of the amplitude and phase of the reflected light collected by the single mode fiber, relative to the input light that enters the sample arm of the interferometer. Once we know $\alpha(z, t)$, we can write the total intensity at the fast photodiode as

$$\begin{aligned} I_{tot} &= |E_{ref} + \alpha(t) E_{in}|^2 \\ &= I_{ref} + |\alpha(t)|^2 I_{in} + \text{Re}[2\alpha(t) E_{in} E_{ref}^*], \end{aligned} \quad (4.2)$$

where Re denotes the real part. Due to the small amplitude of the excited surface acoustic waves (in our case 140 pm), we can neglect second-order loss contribution due to scattering into other spatial modes. We also note that while phase variations in $\alpha(t)$ are only visible in the double product term of Eq. 4.2, amplitude variations are also visible in the $|\alpha(t)|^2 I_{in}$ term and can be observed also with blocked reference arm when $E_{ref} = 0$.

The calculation of the complex collection ratio $\alpha(t)$ is based on the overlap integral between the Gaussian mode supported by the fiber and the beam reflected by the SAW device, as a function of the defocusing, namely the distance z between the SAW device surface and the beam waist position of the focused Gaussian beam. This overlap integral can be calculated at any plane, for simplicity we choose to calculate it on the device surface, so that we don't have to compute how the electric field propagates after reflection. Due to the presence of standing SAWs along the x axis, we can model the surface out-of-plane displacement as

$$\Delta d(x, y, t) = A(t) \cos [K(x - x_0)] , \quad (4.3)$$

where $K = 2\pi/\Lambda$ is the SAW wave number, x_0 is the transverse distance between the center of the laser focus and the position of the standing SAW anti-node, and $A(t) = A_0 \cos(\Omega t)$, is the time-dependent amplitude of the SAW with angular frequency Ω and

peak displacement A_0 . There is no dependency on y because the standing SAW are excited only along the x axis. In Eq. 4.1, we defined the complex collection ratio as a function of time, but now we compute it also as a function of z and x_0 : $\alpha(t) \rightarrow \alpha(z, x_0, t)$. From calculations shown in the Appendix 4.5.1 we obtain:

$$\begin{aligned}\alpha(z, x_0, t) &= \alpha_{DC}(z) + \alpha_{AC}(z, x_0) \cos(\Omega t) \\ \alpha_{DC}(z) &= \frac{1}{1 + i\tilde{z}} \\ \alpha_{AC}(z, x_0) &= \frac{2ikA_0 \cos(Kx_0) \times \exp[-B(1 - i\tilde{z})]}{1 + i\tilde{z}}\end{aligned}\quad (4.4)$$

Here, $\tilde{z} = z/z_R$, $z_R = \pi w_0^2/\lambda$ is the Rayleigh range of the focused Gaussian beam, w_0 its waist radius, $k = 2\pi/\lambda$ the wavenumber, and $B = K^2 w_0^2/8$. The complex collection ratio $\alpha(z, x_0, t)$ can be separated in two parts: a static term $\alpha_{DC}(z)$ which is a Lorentzian function of z and describes the complex collection ratio in the absence of standing SAWs, and a dynamic term $\alpha_{AC}(z, x_0)$, which describes the effect of the time modulation of the light field by the standing SAWs. This dynamic term not only contains the Lorentzian attenuation as a function of the defocusing, but also an additional exponential term that depends on the ratio between the Gaussian waist radius w_0 and the acoustic wavelength Λ via B . This exponential is a complex number, meaning that $\alpha_{AC}(z, t)$ has a certain periodicity in z . In the next section we will provide an explanation of this periodicity by using the Talbot effect.

4.3.2 Single-beam experiment: amplitude modulation

Here we block the reference arm, so that the signal is only given by the amplitude modulation. The quantity responsible for the amplitude modulation is $|\alpha(z, x_0, t)|^2$, and as shown in Appendix 4.5.1, $|\alpha(z, x_0, t)|^2 = |\alpha(z)|_{DC}^2 + |\alpha(z, x_0)|_{\Omega}^2 \cos(\Omega t) + |\alpha(z, x_0)|_{2\Omega}^2 \cos(2\Omega t)$. In our experiment we are only interested in the Ω component since the AC coupled RF photodiode blocks the DC component, and the lock-in amplifier demodulates at Ω . Moreover, the 2Ω term is much smaller in amplitude than the Ω term, since it scales like A_0^2 , as opposed to A_0 for the Ω term. After the demodulation by the lock-in amplifier, we are left with an rms signal of the amplitude modulation given by:

$$V_{amp}^{rms}(z) \propto \frac{2|\gamma|e^{-B}}{\sqrt{2}(1 + \tilde{z}^2)} \times |\sin(B\tilde{z})|, \quad (4.5)$$

where $\gamma = 2kA_0 \cos(Kx_0)$ and the proportionality symbol means that we are not taking into account the gain provided by photodiode and lock-in amplifier. This equation gives periodic zeros at positions that solve the equation $\sin(B\tilde{z}) = 0$, and substituting $B = K^2 w_0^2/8 = \pi^2 w_0^2/(2\Lambda^2)$ and $\tilde{z} = z\lambda/(\pi w_0^2)$, we find that the positions of the zeros is given by $z=n \times z_T$, where n is an integer, and $z_T = 2\Lambda^2/\lambda$ is the classical Talbot length for a diffraction grating with period Λ , illuminated by a plane wave.

4.3.3 Two-beams experiment: phase modulation

Here we interfere light from the sample arm with light from the reference arm. From Eq. 4.2, we see that the phase modulation is detected via $2\text{Re}[\alpha(z, x_0, t)E_{in}E_{ref}^*]$, where

$E_{ref} = E_{in} \times \exp(i\phi_{ref})$ and in the experiment, we adjust the intensity in the reference arm of the interferometer to be equal to the DC intensity in the sample arm at zero defocusing: $|\alpha(z=0)|_{DC}^2 = 1$. We stabilize the interferometer by locking ϕ_{ref} to a specific value of optical intensity I_{lock} via the feedback loop controlling the piezo in the reference arm. In our case we lock at the side of a fringe, which means $\phi_{ref} = \pm\pi/2$ and $I_{lock} = 2I_{ref}$, but only at $z = 0$. In our measurements we vary the distance z between the beam focus and the SAW device, therefore α_{DC} changes both in amplitude and phase, causing ϕ_{ref} to change in order to keep the interferometer locked at the same optical power. While we can calculate $\phi_{ref}(z)$ from Eq. 4.2, imposing that $I_{tot} = I_{lock}$, a more useful quantity is the difference between the phase of $\alpha_{DC}(z)$, and the phase of the reference beam $\Delta\phi(z) = \arg[\alpha_{DC}(z)] - \phi_{ref}(z)$:

$$\Delta\phi(z) \simeq \mp \arccos \left[\frac{\sqrt{1 + \tilde{z}^2}}{2} \left(\frac{I_{lock}}{I_{ref}} - 1 - \frac{1}{1 + \tilde{z}^2} \right) \right], \quad (4.6)$$

where the sign is chosen whether we lock the interferometer on a positive (−) or negative (+) slope. We note that in the derivation of this equation we considered $\arg(\alpha_{DC}) \simeq \arg(\alpha)_{DC}$, and $|\alpha_{DC}| \simeq |\alpha|_{DC}$, which is allowed since the SAW displacement is very small. The rms of the total interferometric signal is obtained by calculating the rms value of the Ω component of Eq. 4.2, which for small SAW displacement A_0 can be approximated as:

$$V_{tot}^{rms} \simeq \frac{2|\gamma|e^{-B}}{\sqrt{2}} \left| \frac{\sin(\Delta\phi + B\tilde{z})}{\sqrt{1 + \tilde{z}^2}} + \frac{\sin(B\tilde{z})}{1 + \tilde{z}^2} \right|. \quad (4.7)$$

The first term in the modulus is from the phase modulation, while the second term originates from amplitude modulation. In detection, the phase modulation term can not be separated from the amplitude modulation term, as it is the result of interference. In mathematical terms, $V_{tot}^{rms} \neq V_{amp}^{rms} + V_{phase}^{rms}$ due to the non-linearity of the modulus function.

4.3.4 Comparison to experiments

Now we compare our theory to experiments where we measure both the amplitude modulation V_{amp}^{rms} and the total interferometric signal V_{tot}^{rms} as a function of the defocusing z , distance between the beam focus and SAW device. In particular, we show the results corresponding to the situation where the focused Gaussian beam is centered on an antinode of the standing SAW, corresponding to $x_0 = 0$ in Eqs. 4.5 and 4.7. While changing the defocusing z , the relative position x_0 between the antinode and the beamspot could change due to imperfect alignment, we do a short line scan along the x direction, exemplarily shown in Fig. 4.2 (b), and we average the amplitudes of the measured peak values.

In Fig. 4.3 (a) we show the measured $|\alpha_{DC}|^2$ as a function of z , corresponding to the DC light intensity coupled back to the fiber in the sample arm of the interferometer measured with the slow photodiode (see Fig. 4.2 (a)), reproducing the expected Lorentzian dependency. Fig. 4.3 (b) shows the measured amplitude modulation V_{amp}^{rms} in blue, as well as the total interferometric signals V_{tot}^{rms} , obtained by locking the interferometer on the positive (red) or negative (yellow) slope on the side of the fringe. The measured signal is the rms Voltage detected by the lock-in amplifier after 1 GHz demodulation, and the grey areas are regions where it is not possible to lock the interferometer at the side of the fringe due to a decrease in the light intensity coupled back to the fiber in the sample

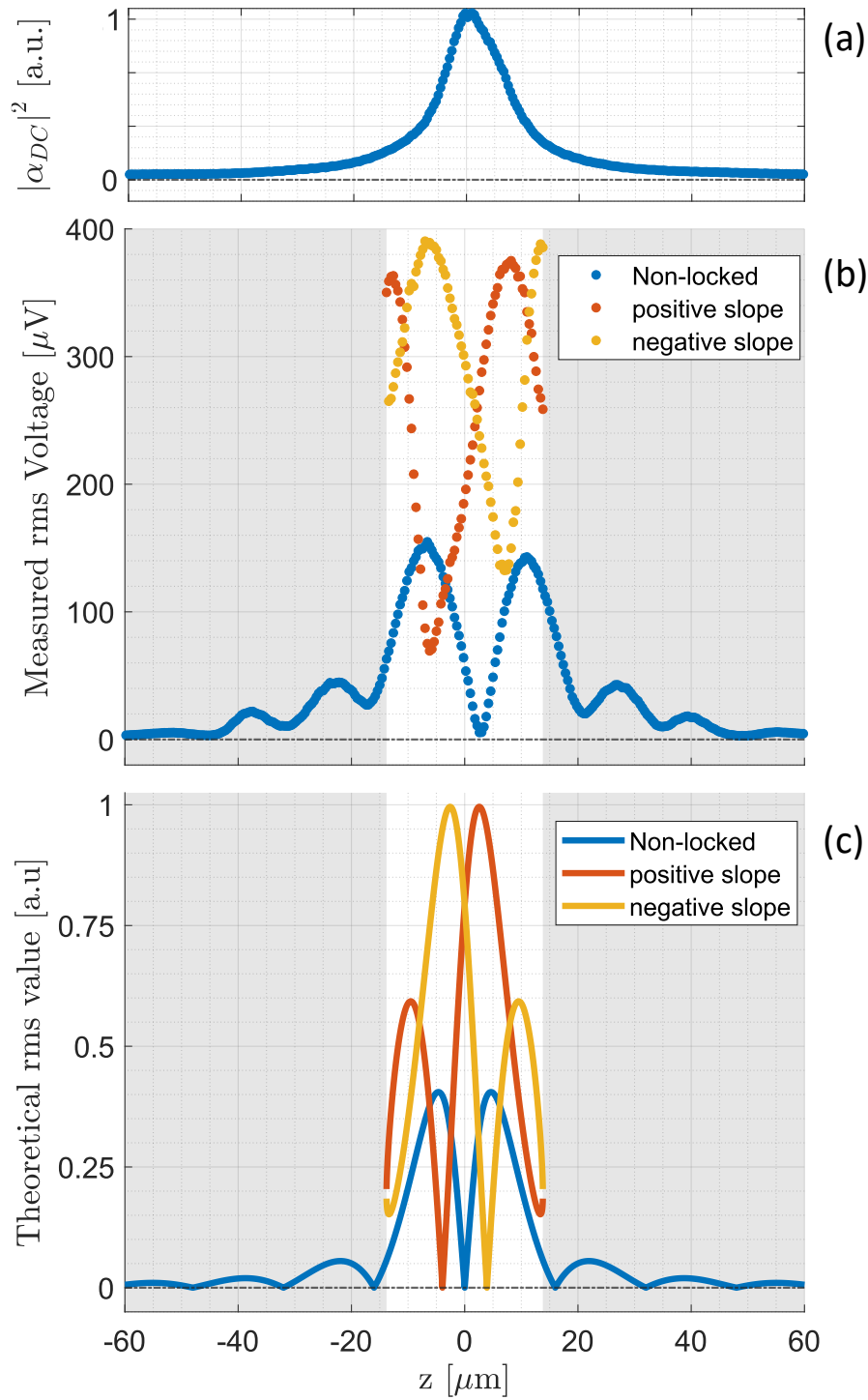


Figure 4.3: (a) Experimental DC component of the complex collection ratio as a function of the defocusing z . (b) Experimental and (c) theoretical Ω component of the amplitude modulation (blue) and of the total interferometric signals for the interferometer locked at the positive (red) or negative (yellow) slope of the fringe.

arm of the interferometer. Fig. 4.3 (c) shows the corresponding theoretical data based on Eqs. 4.5, 4.6 and 4.7.

We observe excellent qualitative agreement between measurements and theory: the signals are almost symmetric with respect to the z defocusing, the total interferometric signals locked at a positive and negative slope intersect at the defocusing z for which the amplitude modulation is zero, and the positions of the minima in the amplitude modulation are close-to-periodic with period $z_{period} = (15.6 \pm 2.8) \mu\text{m}$, where the error is the standard error. This value is quite close to the expected periodicity from Eq. 4.5: $z_T = 2\Lambda^2/\lambda = 16 \mu\text{m}$.

Residual misalignment of the sample arm of the interferometer can explain the few quantitative differences we observe, such as the minimum of the amplitude modulation located at $z \simeq 3 \mu\text{m}$ instead of $z = 0$, and the asymmetry in the height of the peaks between negative and positive detunings, both in the amplitude modulation and in the total interferometric signals. Spurious reflections inside the fiber beam splitter are most likely the reason why the measured signals don't reach zero, except for the central dip in the amplitude modulation.

4.3.5 Explaining the periodicity: the Talbot effect

We have seen from Eq. 4.5 that the amplitude modulation is a signal periodic in z with the period $z_T = 2\Lambda^2/\lambda$. In an attempt to find an intuitive explanation for this phenomenon, we will now show that this is a consequence of the optical Talbot effect caused by diffraction of the laser beam from the standing SAWs. If a reflective grating with periodicity Λ is illuminated by a plane wave under normal incidence, on top of the directly reflected plane wave (zero order), there are diffracted plane waves at angles $\theta \simeq \pm p \lambda/\Lambda$ ($\sin(\theta) \simeq \theta$ for $\lambda \ll \Lambda$), where p is a positive integer corresponding to the diffraction order. In the near field, interference of all the diffracted fields creates periodic replicas of the light field at the grating at integer multiples of the Talbot length $z_T = 2\Lambda^2/\lambda$.

We start with a standing SAW grating described by Eq. 4.3 for $x_0 = 0$ and $t = 0$, where the peak displacement of the standing SAWs is maximum. On the optical axis, we define a new coordinate system \bar{z} , with the SAW device placed at the origin $\bar{z} = 0$, and the beam focus at position $\bar{z} = z$. For clarity, we unfold the back reflected light propagation to the right of $\bar{z} = 0$, as shown in Fig. 4.4. In this new coordinate system, and due to the symmetric unfolding with respect to $\bar{z} = 0$, the projected image of the fiber is always at position $\bar{z} = -z$, and the field coupled back to the fiber after reflection, is the field at this position, after mode-matching to the fiber.

Since we know the optical field at the grating plane $\bar{z} = 0$, we can propagate it to any other plane using the Fresnel-Kirchhoff diffraction integral, and in particular we can calculate the transverse field at $\bar{z} = -z$. A detailed calculation is shown in Appendix 4.5.2, but in Fig. 4.4 (a) we plot an example of the computed diffraction integral at many planes, showing the intensity of the propagated light field after reflection from the grating.

We report here the most important results of the calculation: due to the small SAW displacement, only the first diffraction orders are present, corresponding to two beams tilted at angles of $\theta = \pm\lambda/\Lambda$ with respect to the optical axis. Interference of the zero order and the first-order beams creates periodic images of the field at the grating. Contrary to the case of a grating illuminated by a plane wave, under Gaussian beam illumination, these self-images are laterally magnified by a factor $M_G = R_{\bar{z}}/(R_{\bar{z}} - \bar{z})$ [126], where $R_{\bar{z}} = (\bar{z} - z) \times (1 + z_R^2/(\bar{z} - z)^2)$ is the radius of curvature of the Gaussian beam at a

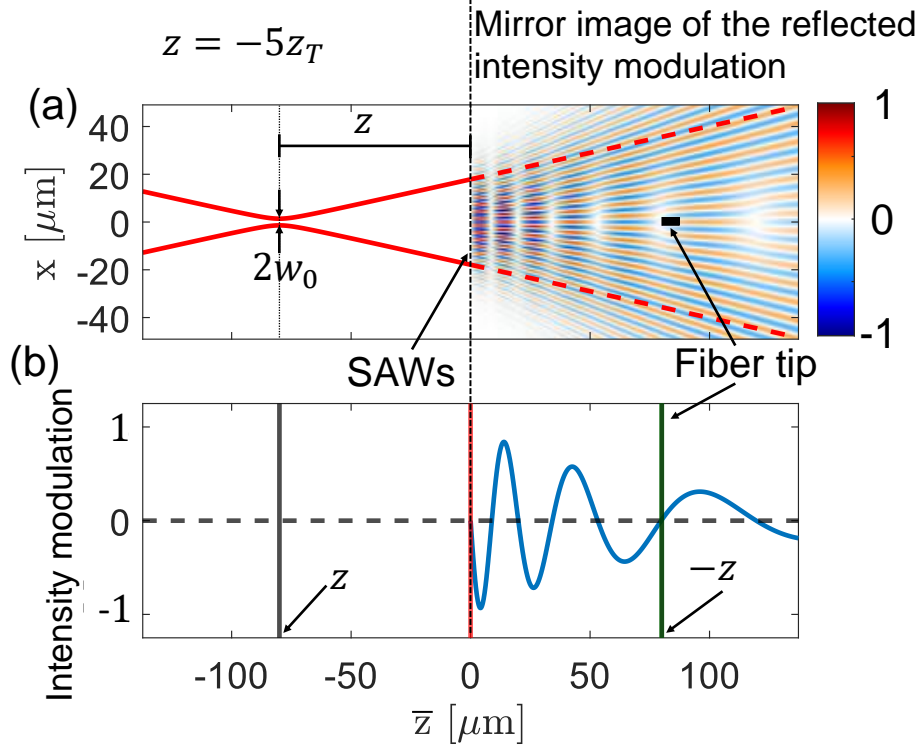


Figure 4.4: Example of Talbot pattern obtained with a beam defocusing of $z = -5z_T$. (a) shows for $\bar{z} < 0$ the Gaussian beam before the grating, and for $\bar{z} > 0$ the mirrored image of the reflected light intensity modulation, with respect to the constant intensity of the non-diffracted Gaussian beam. We considered a SAW profile given by Eq. 4.3, for $x_0 = 0$ and $t = 0$. Self-images of the field at the grating appear at specific positions given by Eq. 4.8, where here are visible as zones with zero intensity modulation. (b) shows a cross-sectional plot of (a) along $x = 0$, showing that on the optical axis, the intensity modulation of the reflected field is zero at the positions of the self-images, and in particular at the mirrored position of the image of the fiber tip as indicated.

generic observation plane \bar{z} . As shown in Ref. [126] the positions of these self images, also non-periodic in \bar{z} , are given by solving

$$m \frac{z_T}{2} = \frac{R_{\bar{z}} - \bar{z}}{R_{\bar{z}}} \times \bar{z}, \quad (4.8)$$

where m is a positive integer. From this equation it is clear that depending on the distance z between the beam focus and the SAW grating, the radius of curvature $R_{\bar{z}}$ changes, and with it, also the Talbot pattern created after reflection.

Each of these different Talbot patterns have self-images at different positions, obtained by solving Eq. 4.8 but, remarkably, we find in Appendix 4.5.2 that when the beam focus is at the distances $z = n \times z_T$ from the grating, with n an integer number, there is always one of the self-images at the position $\bar{z} = -z$, coinciding with the position of the projected image of the fiber.

This is visible in Fig. 4.4 (a) where for $\bar{z} \geq 0$ we show the intensity modulation, relative to the intensity of a non-diffracted Gaussian beam, as well as a cross section of this field along the optical axis $x = 0$ (b). These plots show the intensity of the diffracted light field at time $t = 0$, with respect to the intensity of a non-diffracted Gaussian beam (without

SAWs). After half period of the SAW oscillation, at time $t = T/2$, the plots are the same with the only difference that positive (red) and negative (blue) intensity fluctuations are exchanged.

The intensity of the field at the positions of the self-images is constant in time, because the reflection from SAWs acts as a phase grating, therefore modulating only the phase of the light field, as visible by writing the field at the grating, after reflection:

$$\psi_{reflect}^-(\bar{z} = 0, x, t) = \psi_{in}^+(\bar{z} = z) \times \exp[2ikA_0 \cos(Kx) \cos(\Omega t)] . \quad (4.9)$$

In Fig. 4.4 (a), we can also observe that the region of constant intensities are concentrated close to the optical axis ($x = 0$)- this is because we are illuminating only a small portion of the grating. We note that also the number of self-images obtained after reflection depends on the Gaussian beam radius at the grating, and therefore on the number of grating periods that are illuminated. In particular, the minimum beam radius needed to observe a number m of self-images is given by (derivation in Appendix 4.5.2):

$$w_{min}(m) = \Lambda \sqrt{\frac{2m}{\pi}} . \quad (4.10)$$

Despite the intensity of the field at the positions of the self-images is time independent, in principle this is not enough to ensure that the amplitude modulation is zero at the positions of the self-images, because mode-matching to the fiber can convert the time-dependent phase with angular frequency Ω , into a time-dependent amplitude of the field with the same angular frequency. However at the positions of the self images, this does not happen, as shown in the calculation for the complex collection ratio.

Although we did not find a truly intuitive explanation for this effect, we provide here a heuristic picture; first we consider the case where the laser beam is focused on the SAW device: at the surface, the wavefront of the non-diffracted Gaussian beam is flat, which correspond to a constant phase on the xy plane. The reflected Gaussian beam at the SAW surface is given by Eq. 4.9 for $z = 0$, and we can see that the corresponding surface displacements at the times $t = 0$, and time $t = T/2$, corresponding to half oscillation period, are symmetric with respect to the flat wavefront of the non-diffracted Gaussian beam. Because of this, the amplitude of the field mode-matched to the fiber is the same at the times $t = 0$ and $t = T/2$, giving rise to the 2Ω modulation as shown in Appendix 4.5.1, and no Ω component.

Now we consider the case where the laser beam is defocused with respect to the SAW device, specifically being at a distance $z = n \times z_T$ such that the projected image of the fiber is at the position of the $n - \text{th}$ Talbot image. While at this position the amplitude of the field is time independent, because it is an image of the amplitude of the field at the SAW grating, the phase is not time independent. Moreover, in this case, the non-diffracted Gaussian beam has a finite radius of curvature, leading to a non-constant phase on the xy plane: the surface displacement over one oscillation period is not symmetric anymore with respect to the phase of the non-diffracted Gaussian beam. However, given the small spatial extension of the fiber along the xy plane, the radius of curvature of the no-diffracted Gaussian beam can be approximated as flat. The result is that once again, the amplitude of the field coupled back to the fiber, has only 2Ω modulation, and no Ω modulation. Despite this picture is a simplification and does not fully grasp the complexity of the real experiment, it can be a useful tool to understand the phenomenon, without having to explicitly calculate the overlap integral between the field supported by the fiber and the propagated field after diffraction from the SAW grating.

4.4 Conclusions and outlook

By using a fiber-based Michelson interferometer to measure GHz standing SAWs in a SAW cavity, we discovered that on top of the usual phase modulation term, the total interferometric signal also has a significant amplitude modulation term. We measured the strength of the amplitude modulation as a function of the probe beam defocusing, and showed that the amplitude modulation vanishes at zero defocusing, but also at periodic defocusing from the SAW device, corresponding to multiples of the Talbot length. This is surprising as for non-plane wave illumination, Talbot self-images usually appear at non-periodic distances [126]; while this is true, the positions of the self-images change as we change the beam defocusing, but we find that when the beam defocusing is a multiple of the Talbot length, there is always a self-image created at the projected image of the collecting fiber.

We want to point out here that our experiment shows that an interferometric setup is not always the optimal solution for measuring spatially-resolved oscillating surface displacements such as induced by SAWs, and simple amplitude measurements in a single-mode fiber-coupled setup can be an easier way. Then, the fiber splitter can be replaced by a fiber circulator which maximizes the optical power available at the oscillating surface, and therefore maximizing the measured signal. Depending on the SAW period Λ and the beam waist radius w_0 , the amplitude modulation can even be stronger than the conventional interferometric signal – if $\Lambda \lesssim w_0$.

4.5 Appendix

4.5.1 The complex collection ratio

Here we derive the complex collection ratio $\alpha(z, x_0, t)$. We use the shifted reference frame where the focus of the Gaussian beam, as projected image of the input fiber, is the origin of the optical axis, and the reflecting surface is at a distance z . This shift does not change the final results that depend only on the relative distance between the SAW device and the focus of the Gaussian beam. We consider the ideal case where the imaging system produces a perfect image of the fiber tip in the focus. This field can be written as $E_{in}(x, y, z, t) = \psi_{in}^+(x, y, z) \exp(-ikz + i\omega t)$ with a forward-propagating Gaussian mode (without Gouy phase)

$$\begin{aligned} \psi_{in}^+(x, y, z) &= \frac{\sqrt{2}}{\sqrt{\pi}w(z)} \times \exp\left[-ik\frac{x^2 + y^2}{2q(z)}\right] \\ &= \frac{\sqrt{2}}{\sqrt{\pi}w(z)} \times \exp\left[-\frac{x^2 + y^2}{w^2(z)}(1 + i\tilde{z})\right], \end{aligned} \quad (4.11)$$

where $q(z) = z + iz_R$ is the complex beam parameter, $z_R = \pi w_0^2/\lambda$ is the Rayleigh range, w_0 is the beam waist radius located at $z = 0$, $w(z) = w_0\sqrt{1 + \tilde{z}^2}$ is the beam radius at position z , and $\tilde{z} = z/z_R$. The field is normalized:

$$\iint |\psi_{in}^+(x, y, z)|^2 dx dy = 1. \quad (4.12)$$

The complex collection ratio defined in the main text can be calculated via the overlap integral between the reflected backward-propagating field, and the backward-propagating image of the input field $\psi_{in}^- = (\psi_{in}^+)^*$. This overlap integral can be calculated at any z plane, since optical propagation is a unitary operation. We calculate it at the plane of the SAW device. For a flat and perfectly reflecting interface, the reflected field mimics the input field $E_{refl}^- = E_{in}$, and we obtain the DC coupling:

$$\alpha_{DC} = \iint \psi_{in}^+(x, y, z)^2 dx dy = \frac{1}{1 + i\tilde{z}}.$$

We can calculate the in-coupling efficiency η as

$$\eta = |\alpha_{DC}|^2 = \frac{I_{col}}{I_{in}} = \frac{1}{1 + \tilde{z}^2}, \quad (4.13)$$

which corresponds to the DC coupling when we displace the reflecting surface by an amount z , with respect to the position of the beam waist.

We now consider how standing surface acoustic waves (SAWs) modulate the complex collection ratio α . In presence of standing SAWs, the reflecting surface oscillates with profile

$$\Delta z(x, y) = A(t) \cos[K(x - x_0)], \quad (4.14)$$

where $K = 2\pi/\Lambda$ is the SAW wave number, Λ is the SAW wavelength, $A(t) = A_0 \cos(\Omega t)$ is the displacement at an anti-node with amplitude A_0 , Ω is the SAW angular frequency, and x_0 indicates the position of the laser beam. The reflected field becomes

$$\psi_{refl}^- = \exp(2ik(z + \Delta z))\psi_{in}^+, \quad (4.15)$$

where $\Delta z > 0$ is away from the input fiber. From Eq. 4.15, we remove the stationary phase factor $\exp(2ikz)$, and we obtain

$$\alpha(z, x_0, t) = \iint \exp(2ik\Delta z)\psi^+(x, y, z)^2 dx dy. \quad (4.16)$$

Substituting 4.14 into 4.16, we arrive at the following integral:

$$\begin{aligned} \alpha(z, x_0, t) &= \iint \exp\{2ikA(t) \cos[K(x - x_0)]\} \\ &\times \exp\left[-\frac{2(x^2 + y^2)(1 + i\tilde{z})}{w^2(z)}\right] \frac{dx dy}{\pi w^2(z)}. \end{aligned} \quad (4.17)$$

This integral can be solved by separating the integral in x and y direction:

$$\begin{aligned} \alpha(z, x_0, t) &= \frac{2}{\pi w^2(z)} I_y I_x, \text{ where} \\ I_y &= \int_{-\infty}^{+\infty} \exp\left[-\frac{2y^2}{w^2(z)}(1 + i\tilde{z})\right] dy \\ I_x &= \int_{-\infty}^{+\infty} \exp\left[-\frac{2x^2}{w^2(z)}(1 + i\tilde{z})\right] \times e^{2ik\Delta z} dx. \end{aligned} \quad (4.18)$$

I_x and I_y can be solved by using the standard integral

$$\int_{-\infty}^{+\infty} \exp[-ax^2 + ibx] dx = \sqrt{\frac{\pi}{a}} \exp\left(-\frac{b^2}{4a}\right). \quad (4.19)$$

While evaluation of I_y is straightforward, yielding

$$I_y = \sqrt{\frac{\pi}{2(1 + i\tilde{z})}} w(z), \quad (4.20)$$

evaluating I_x requires a few more steps: first we separate the generic standing SAW displacement in Eq. 4.14 into the sine and cosine quadratures:

$$\cos[K(x - x_0)] = \cos(Kx) \cos(Kx_0) + \sin(Kx) \sin(Kx_0), \quad (4.21)$$

then, since $kA(t) \ll 1$, we can expand the exponential:

$$\begin{aligned} \exp\{2ikA(t) \cos[K(x - x_0)]\} &\simeq \\ 1 + 2ikA(t)[\cos(Kx) \cos(Kx_0) + \sin(Kx) \sin(Kx_0)]. \end{aligned} \quad (4.22)$$

Multiplication of this term by the Gaussian function, and their integration, leads to I_x . We observe that, since $\sin(Kx)$ is an odd function of x , whereas the Gaussian function is even, the integral vanishes and we obtain:

$$I_x = I_y + 2ikA(t) \cos(Kx_0) \quad (4.23)$$

$$\times \int_{-\infty}^{+\infty} \exp \left[-\frac{2x^2}{w^2(z)}(1 + i\tilde{z}) \right] \cos(Kx) dx .$$

We can use the expansion $\cos[Kx] = [\exp(iKx) + \exp(-iKx)]/2$ to obtain the following equation:

$$I_x = I_y + ikA(t) \cos(Kx_0) \times (G^+ + G^-), \quad \text{where} \quad (4.24)$$

$$G^\pm = \int_{-\infty}^{+\infty} \exp \left[-\frac{2x^2}{w^2(z)}(1 + i\tilde{z}) \right] \times \exp(\pm iKx) dx.$$

The physical meaning of this equation is the following: for a small SAW displacement A_0 , the reflecting surface behaves as an amplitude diffraction grating with cosine profile. The Gaussian beam impinges on this diffraction grating, and the back reflection is coupled back to the fiber (term I_y in Eq. 4.24). The diffraction grating also generates two tilted Gaussian beams with angles $\theta^\pm = \pm\lambda/\Lambda$, corresponding to the terms G^+ and G^- in Eq. 4.24, as will be shown in Appendix 4.5.2. By using once again the standard integral 4.19, we obtain:

$$G^\pm = \sqrt{\frac{\pi}{2(1 + i\tilde{z})}} w(z) \exp[-B(1 - i\tilde{z})] , \quad (4.25)$$

where $B = -K^2 w_0^2/8$. Inserting Eq.4.25 into I_x , and I_x into Eq. 4.18, we get:

$$\alpha(z, x_0, t) = \frac{1}{1 + i\tilde{z}} \{1 + 2ikA(t) \cos(Kx_0) \exp[-B(1 - i\tilde{z})]\} . \quad (4.26)$$

The amplitude modulation term is given by $|\alpha(z, t)|^2$, which after some calculations can be expressed as:

$$|\alpha|^2 = |\alpha|_{DC}^2 + |\alpha|_\Omega^2 \cos(\Omega t) + |\alpha|_{2\Omega}^2 \cos(2\Omega t) \quad (4.27)$$

$$|\alpha|_{DC}^2 \simeq \frac{1}{1 + \tilde{z}^2}$$

$$|\alpha|_\Omega^2 = -\frac{2\gamma \times \exp(-B) \times \sin(B\tilde{z})}{1 + \tilde{z}^2}$$

$$|\alpha|_{2\Omega}^2 = \frac{\gamma^2 \times \exp(-2B)}{2(1 + \tilde{z}^2)} ,$$

where $\gamma = 2kA_0 \cos(Kx_0)$.

4.5.2 The Talbot effect

Here we explicitly calculate the propagated field after the grating, used to create the plots in Figs. 4.1 and 4.4, and to visualize the Talbot patterns created by diffraction of a Gaussian beam from a periodic grating. Since the grating affects the propagated field only along the x transverse direction, for simplicity we study the evolution of a 1D Gaussian beam after reflection from the surface.

On the optical axis, we define a new coordinate system \bar{z} with the origin at the surface of the SAW device. In this coordinate system, the beam focus is at position $\bar{z} = z$, where z is the beam defocusing introduced in the calculations for the complex collection ratio. For clarity, and as illustrated in Fig. 4.4 in the main text, we unfold the reflected field to the right of $\bar{z} = 0$. The field at the surface ($\bar{z} = 0$) is given by the function

$$\psi_{reflect}^-(\bar{z} = 0, x, t) = \psi_{in}^+(z) \times \exp[2ikA(t) \cos(Kx_0) \cos(Kx)] ,$$

where we omitted the sine quadrature in the expansion of the displacement (Eqs. 4.14, 4.22) due to integration in the next step. The field $g(x, \bar{z}, t)$ at a generic position \bar{z} is given by convolution of the input field $\psi_{reflect}^-(\bar{z} = 0, x, t)$ with the impulse response function of free space in the Fresnel approximation (Fresnel-Kirchhoff diffraction integral):

$$h(x, \bar{z}) \simeq h_0 \exp\left(-i\frac{\pi}{\lambda\bar{z}}x^2\right) , \quad (4.28)$$

where $h_0 = i/(\lambda\bar{z})$, leading to

$$g(x, \bar{z}, t) = h_0 \int_{-\infty}^{+\infty} \psi_{reflect}^-(x', t) \times \exp\left[-i\frac{\pi}{\lambda\bar{z}}(x - x')^2\right] dx' . \quad (4.29)$$

Following the same steps we used to calculate the complex collection ratio $\alpha(z, t)$, we expand the exponential containing the cosine term:

$$\begin{aligned} \exp[2ikA(t) \cos(Kx_0) \cos(Kx)] &\simeq 1 + i\gamma(t) \cos(Kx), \\ \text{where } \gamma(t) &= 2kA_0 \cos(Kx_0) \cos(\Omega t) . \end{aligned} \quad (4.30)$$

Physically this means that for small SAW displacements, the phase grating described above can be approximated by an amplitude grating with cosine profile, and a phase shift of $\pi/2$ given by the imaginary number in front of the cosine. We can expand the cosine in exponential form: $\cos(Kx) = [\exp(iKx) + \exp(-iKx)]/2$, and finally we can rewrite Eq. 4.29 as

$$\begin{aligned} g(x, \bar{z}, t) &= \int_{-\infty}^{+\infty} \psi_{in}^+ \times h(x - x', \bar{z}) dx' \\ &+ \frac{i\gamma(t)}{2} \int_{-\infty}^{+\infty} \psi_{in}^+ \times \exp(iKx') \times h(x - x', \bar{z}) dx' \\ &+ \frac{i\gamma(t)}{2} \int_{-\infty}^{+\infty} \psi_{in}^+ \times \exp(-iKx') \times h(x - x', \bar{z}) dx' . \end{aligned} \quad (4.31)$$

The first term describes the evolution of a Gaussian beam, and therefore represents the backreflected Gaussian beam, as if it was reflected from a flat surface. The second and third terms describe two tilted beams at an angle of $\theta = \pm\lambda/\Lambda$ with respect to the optical axis, as we can see by writing the second (+) and third (-) terms as:

$$\begin{aligned} g_{\pm} &= \frac{i\gamma(t)h_0C}{2} \exp\left(-\frac{i\pi x^2}{\lambda\bar{z}}\right) \int_{-\infty}^{+\infty} \exp[-ax'^2] \\ &\times \exp\left[ix' \frac{2\pi}{\lambda\bar{z}} \left(x \pm \bar{z} \frac{\lambda}{\Lambda}\right)\right] dx' , \end{aligned} \quad (4.32)$$

where

$$a = \left(\frac{1 + iz/z_R}{2w_0^2(1 - z^2/z_R^2)} + \frac{i\pi}{\lambda\bar{z}} \right), \quad (4.33)$$

and C is a normalization factor. The integral in Eq. 4.31 can be solved by using the standard integral from Eq. 4.19. We do not show here the lengthy expression, but an example solution is shown in Fig. 4.4 in the main text, where we evaluated the integral at $t = 0$ and $z_0 = 5z_T$.

As a result of the interference between the diffracted beams, self-images of the field at the grating appear at non-periodic positions on the optical axis. These positions are dependent on the radius of curvature of the field impinging on the grating, and therefore on the beam defocusing z . Therefore different values of z , leads to different Talbot patterns.

4.5.2.1 Existence and positions of the self images

Here we solve Eq. 4.8, and we show that for beam defocusings $z = nz_T$, where n is an integer, one of the self-images is always located at $\bar{z} \simeq -z$, which in our coordinate system and with the unfolded reflection, corresponds to the position of the projection of the image of the fiber. We will also give a proof for Eq. 4.10.

Starting by substitution of $R_{\bar{z}} = (\bar{z} - z)(1 + z_R^2/(\bar{z} - z)^2)$ into Eq. 4.8, we obtain a second order equation $a\bar{z}^2 + b\bar{z} + c = 0$, where $a = z + mz_T/2$, $b = -(mzz_T + z^2 + z_R^2)$, $c = mzz_T(z^2 + z_R^2)/2$. This equation has two solutions given by

$$\bar{z}_{1,2} = \frac{m z z_T + z^2 + z_R^2 \pm (z^2 + z_R^2)\sqrt{1 - \delta^2}}{2(z + mz_T/2)}, \quad (4.34)$$

where $\delta = mzz_T/z_R/(z^2 + z_R^2)$. The first thing we notice is that the solutions only exist if $\delta^2 \leq 1$, which, under the condition that $m > 0$, leads to the equation:

$$z_0^2 \geq z_R (m z_T - z_R), \quad (4.35)$$

which gives the minimum distance between the beam waist of the focused Gaussian beam and the grating, in order to observe a number m self images. This equation can be rewritten in terms of the beam radius at the grating, showing that in order to see m self-images, the minimum beam radius at the grating has to be

$$w_{min}(m) = \Lambda \sqrt{\frac{2m}{\pi}}. \quad (4.36)$$

We can now see what happens to Eq. 4.34 when $z = nz_T$, in the limit that $\delta \ll 1$, where we can approximate $\sqrt{1 - \delta^2} \simeq 1$:

$$\bar{z}_{1,2} \simeq \frac{m n z_T^2 + n^2 z_T^2 + z_R^2 \pm (n^2 z_T^2 + z_R^2)}{z_T(2n + m)}, \quad (4.37)$$

and by choosing the solution with the (-) sign, we obtain $\bar{z}_1 \simeq z_T \times mn/(2n + m)$, and for $n = -m$ we get $\bar{z}_1 = -nz_T$, proving that the n -th self image lies at the position $\bar{z} \simeq -z$. To check if $\delta \ll 1$, we can introduce a variable a equal to the ratio between the SAW wavelength and the beam waist radius, such that $\Lambda = aw_0$, and we can write

$$\delta = \frac{2\pi m a^2}{\pi^2 + 4 m^2 a^4}. \quad (4.38)$$

We can see that $\delta \sim m^{-1}$ when $m \rightarrow \infty$, therefore the approximation is better for high values of m . In our experiment $a = 2$ ($\Lambda = 2.8 \mu m$ and $w_0 = 1.4 \mu m$), and already for $m = 1$, the approximation used in Eq. 4.37 is valid.

5 Active stabilization of an open-access optical microcavity for low-noise operation in a standard closed-cycle cryostat

Open-access optical microcavities are Fabry-Perot type cavities consisting of two micrometer-size mirrors, separated by an air (or vacuum) gap typically of a few micrometers. Compared to integrated microcavities, this configuration is more flexible as the relative position of the two mirrors can be tuned, allowing for easy changes in parameters such as cavity length and mode volume and the selection of specific transverse cavity modes. These advantages come at the expense of the mechanical stability of the cavity itself, which is particularly relevant in noisy closed-cycle cryostats. Here, we show an open-access optical microcavity based on scanning-probe microscope design principles. When operated at 4 K in a tabletop optical closed-cycle cryostat without any dedicated mechanical low-pass filter, we obtain stabilities of 5.7 and 10.6 pm rms in the quiet and full periods of the cryocooler cycle, respectively. Our device has free-space optical access, essential, for instance, for full polarization control.

This chapter is based on: M. Fisicaro, M. Witlox, H. van der Meer, and W. Löffler, Active Stabilization of an Open-Access Optical Microcavity for Low-Noise Operation in a Standard Closed-Cycle Cryostat, *Review of Scientific Instruments* 95, 033101 (2024) [60].

5.1 Introduction

Optical microcavities are a powerful tool to enhance the interaction between light and quantum systems [127]. Depending on the strength of this interaction, it enables different applications: in the weak coupling regime, the Purcell effect enables highly efficient extraction of photons for single photon sources as well as counteracting dephasing by the increased spontaneous emission rate in the desired optical mode [53–56, 128], while the strong coupling regime enables deterministic interaction between distant quantum emitters and two-photon quantum gates [129–134]. Open-access microcavities are a miniaturized version of Fabry-Perot optical cavities, consisting of two mirrors where at least one has a micrometer-scale curvature and which can be positioned with very high precision with respect to each other [135, 136]. While maintaining a small mode volume and potentially high finesse [58, 137, 138], they allow tuning of the resonance frequency and transverse cavity mode [139], spatial positioning of the cavity mode with respect to quantum emitters, and a high coupling or collection efficiency [56, 136, 140].

For the above-mentioned applications, many quantum emitters require cooling down to a few Kelvin, ideally around 4 K for self-assembled semiconductor quantum dots, and the cavity needs to be mechanically stable to maintain spectral overlap with an optical transition of the quantum emitter. While helium bath cryostats can be made mechanically very quiet, resulting in a very high mechanical stability of the cavity with root mean square (rms) fluctuations of the cavity length down to 4.3 pm [58, 138], it would be highly advantageous to be able to use instead a tabletop optical closed-cycle cryostat without the need for liquid helium, enabling portability and minimizing maintenance.

Because of the noisy nature of closed-cycle cryostats, the realization of stable open-access microcavities is challenging. Recent developments have been made with fiber-based microcavities by using mechanical low-pass filters in the cryostat [59, 141–143], and fluctuations of the cavity length as low as 15 pm rms have been obtained in noncontact mode, down to 0.8 pm rms when the cavity is operated with direct contact between the two mirrors [59]. However the use of a mechanical low-pass filter is not trivial in combination with free-space optical coupling to the cavity. A low-pass filter is essentially a low-Q harmonic oscillator [144], and while it rejects high-frequency vibrations, it introduces inevitably a time dependent sideways motion of the whole open-cavity device with respect to the laser beam. This sideways motion happens at the resonance frequency of the low-pass filter and can cause time dependent fluctuations in the optical power coupled to the cavity.

Here, we show that for an open microcavity with free-space optical access, it is possible to achieve high stability in an optical tabletop closed-cycle cryostat (Montana Cryostation s100 with Gifford-McMahon cryocooler) without using a dedicated mechanical low-pass filter, by careful mechanical design of the open-cavity device and using conventional feedback stabilization. In particular, without direct contact between the two mirrors, we demonstrate sub-picometer stability at room temperature, while in a tabletop closed-cycle cryostat at 4 K, we reach stabilities of 5.7 and 10.6 pm rms in the quiet and full periods of the cryocooler, respectively.

5.2 Device design

Our open microcavity has a plano-concave configuration, where we use a large flat bottom thin-film mirror and, as the top concave mirror, a commercial chip containing an array of

micro-mirrors with radii of curvature ranging from 10 to 100 μm . The desired top mirror can be selected by adjusting the external mode-matching optics. The two mirrors need to be kept at a fixed distance by a device that allows for nanometric alignment of the two mirrors with respect to each other along the three spatial directions and two angles, while being insensitive to vibrations in order to operate in a mechanically noisy environment. This is because the cryo-cooler used in closed-cycle cryostats produces periodic mechanical pulses that propagate through the cryostat, reaching the open-cavity device and exciting its mechanical resonances. As a result, the distance between the two mirrors is subject to fluctuations induced by these vibrations.

The consequences of these vibrations are more or less severe depending on the cavity finesse which is determined by the mirror reflectivity. In order to maintain resonance of the laser with respect to the cavity (or quantum emitters therein), the fluctuations of the cavity length must be much smaller than the FWHM (full width at half maximum) of the cavity resonance. In our case, we aim to use the cavity for a Purcell-enhanced quantum-dot single photon source, and therefore, a modest finesse is sufficient [53–56]. The coating of the concave micromirrors was, therefore, designed for a cavity with a finesse of $F \sim 2500$ at a wavelength of $\lambda = 935$ nm, which results in a FWHM of the cavity resonance in terms of cavity length change of $\Delta L_{FWHM} \sim 190$ pm, where ΔL_{FWHM} is given by

$$\Delta L_{FWHM} = \frac{\lambda}{2F}. \quad (5.1)$$

The fluctuations in the cavity length must be much smaller than this value. For example, for fluctuations 10 times smaller than ΔL_{FWHM} , we require a stability of 19 pm.

This is extremely challenging, and because fully tunable open access optical microcavities are relatively new, most of the techniques and approaches related to the design of such systems are not very well established in the field of optics. However, the same challenges can be found in scanning probe microscopes (SPMs) that have been developed since the 1980s, where the challenge is to keep the tip-sample distance stable in the same way as for the two mirrors here. For SPMs, ultra-high mechanical stabilities have been achieved in a closed cycle cryostat, with a tip-sample distance variation up to 1.5 pm [145] but only if a helium exchange gas vibration isolation system is used, and even a higher stability in a He bath cryostat, with an average vibration level of ~ 6 fm/ $\sqrt{\text{Hz}}$ [146]. With this in mind we decided to design our device shown in Fig. 5.1 following the principles and guidelines adopted in the design of scanning tunneling microscopes (STMs) [144, 146].

As shown in Figs. 5.1(a) and 5.1(b), the device is divided into two parts: the top plate and the bottom part. The bottom flat mirror (1) is mounted with grease on a custom-built high-stiffness XY translation stage (2) that consists of a polished sapphire plate on top of a XY shear piezo glued to the bottom part of the device, similar to those used in STMs [147]. The XY stage has a step size in the nanometer range with a travel range of about 5 mm. The top plate has a hole in its center for optical access.

On the bottom side of the top plate, the top cavity mirror mount is attached in an assembly that consists of a ring-shaped alumina disk (3), a ring piezo (4), another alumina ring-shaped disk (5), and the micro-mirrors array (6), all glued together with epoxy adhesive (EPO-TEK H74F), which is proven to enable strong and stiff connections in SPM vacuum applications. The thickness of the alumina disks has been chosen to minimize cavity length changes during cooldown.

The ring piezo (4) (Noliac NAC2125) is used for precision scanning and active stabilization of the cavity length. The relative alignment of the two cavity mirrors is accomplished

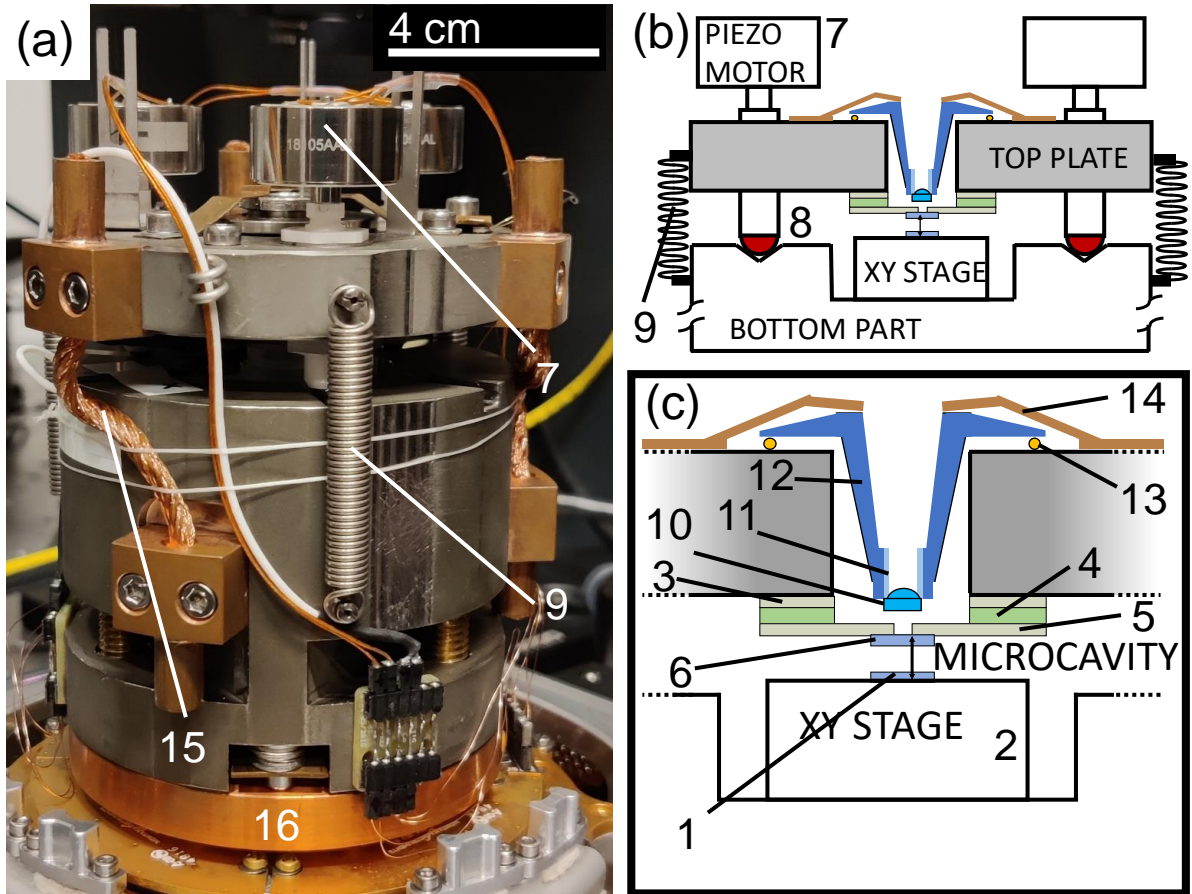


Figure 5.1: Picture of the open-cavity device (a) and corresponding not-to-scale sketches (b), and (c). The top plate and bottom part, as well as the lens mount (11, 12), are made from invar and held together by springs; the bottom part is clamped to the cold base plate of the cryostat by a copper adapter disk (16). Three copper braids are used to cool the top plate (15). The other elements are described in the main text.

with three piezo motors (JPE CLA 2201) in a tip-tilt configuration (7), which enables adjustment of the distance as well as the angles between the top and bottom mirrors with nanometric precision.

To ensure mechanical stability and to decouple the movement of the top plate from a XY translation, the three ceramic spherical tips (8) at the end of the spindle of the piezo motors rest on three v-grooves engraved on the upper side of the bottom part. Finally, the top plate and bottom part are held together with three metal springs (9) each exerting a force of 12 N, tuned such that the piezo motors operate well. Mode matching to the microcavity mode is achieved with an aspheric lens with 0.4 NA (10), mounted in a lens holder consisting of an invar micrometric screw (11) in a threaded invar cone (12) housed in the central hole of the top plate.

The lens holder has a smaller diameter than the hole in the top part, in such a way that the lens can be translated in the XY plane for alignment with the optical microcavity mode, and rests on three ruby balls (13) of 1 mm diameter, glued into holes made in the top invar plate. After aligning the lens in the XY plane and along the z direction (with the micrometric inner screw), it is clamped down with three leaf springs (14). To achieve cooling of the top plate, we thermally connected it to the bottom part of the open-cavity

device using three copper braids (15). This soft connection minimizes the amount of vibration transferred to the top plate. The bottom part is clamped to the cold base plate of the cryostat by a copper adapter disk (16), without a dedicated mechanical low-pass filter between the cryostat and our device.

The choice of the particular ring piezo mounted on the top plate is a compromise, as usually one would choose a small-diameter piezo element with small capacitance and, therefore, high bandwidth, but our choice is limited by the mode matching lens. Due to its short working distance (3.39 mm), in order to get close to the concave top cavity mirror, the lens must fit in the hole of the ring piezo, therefore limiting its minimum size. The material of choice for the bottom part, top plate, and lens mount is Invar-36, which has been proven to be a good solution in designing optical cryogenic systems due to its low thermal expansion coefficient [148], which ensures minimal optical realignment after cool-down.

The use of nanopositioners and piezo elements is crucial for the alignment and operation of the microcavity, but the complex structure of these actuators introduces mechanical resonance frequencies into the device. In particular, the lowest-frequency mechanical resonance of the cavity device that significantly affects the cavity length reduces the passive mechanical stability [144] and the maximum possible bandwidth of the feedback stabilization circuit [149]. In order to push this mechanical resonance as high as possible in frequency, we maximized the stiffness of the open-cavity device by connecting the different parts together by using either springs with high spring constants or a high-performance epoxy adhesive. In addition, we preserved, as much as possible, a rotational symmetry with respect to the central axis of the open-cavity device; this avoids mechanical mode-splitting and reduces the number of mechanical resonances in the device.

5.3 Device characterization: feedback loop and mechanical resonances

We now introduce the experimental setup that we will use in the rest of this paper. We discuss the negative feedback circuit used for active stabilization of the cavity length, and we show how, by measuring the transfer function of this feedback loop, we can characterize the resonances of the open-cavity device [150–152]. This knowledge is of extreme importance not only because the lowest mechanical resonance can pose a serious limitation on active stabilization, but also because it limits the passive stability, as discussed in Ref. [144]. The identification of the mechanical resonances helped us improve the stability of the open-cavity device by redesigning some of its parts iteratively.

5.3.1 Optical setup:

We operate the microcavity in reflection, as shown in Fig. 5.2: a collimated laser beam is sent to the mode-matching lens of the open-cavity device, which couples light to the cavity; the reflected light travels back along the same path and is redirected to a photodiode (Thorlabs PDA-36 EC) by a beam splitter. Before reaching the photodiode, part of the light is also sent to an imaging CCD by a pellicle beam splitter, allowing imaging of the micro-mirrors array and observation of the shape of the particular transverse mode excited in the cavity.

We use narrow-linewidth tunable diode lasers in a range from $\lambda = 935$ nm to 1000 nm.

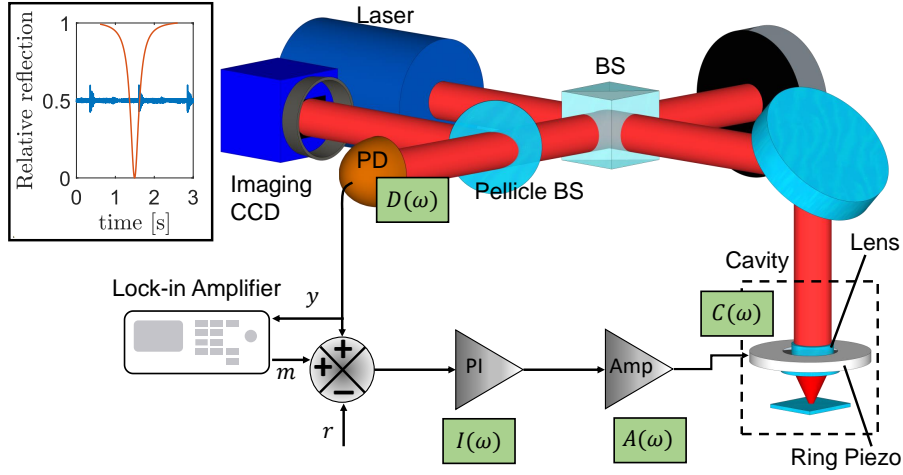


Figure 5.2: Optical scheme for measuring the open-loop transfer function of the feedback loop: laser light is coupled to the cavity, and the backreflection is both monitored with an imaging CCD and measured by a photodiode, giving a signal y . The difference between y and the (constant) reference signal r is the error signal that is fed into the proportional-integral (PI) controller that controls the ring piezo via an amplifier. A lock-in amplifier is used to measure the signal y from the photodiode and to add a modulation m on top of it in order to measure the open loop transfer function of the feedback system. The inset shows the cavity reflection dip as well as a time trace of the stabilized cavity length.

The thin-film coating of our cavity micro-mirrors is centered at $\lambda = 935$ nm, for which the cavity has a finesse F of ~ 2500 . The maximum coupling efficiency we obtained at $\lambda = 935$ nm is $\eta = 64\%$, and we reach $\eta = 80\%$ at a different wavelength where the cavity has a finesse $F = 500$. We have identified the scattering losses of the mirrors as the main limiting factor for the coupling efficiency. The cavity resonance reflection dip is shown in the inset of Fig. 5.2.

5.3.2 Cavity stabilization feedback loop

In order to keep the cavity resonant with the laser, we use active stabilization of the cavity length. The signal from the photodiode is first sent through a lockbox (PI controller with scanning and locking capabilities), and then through a low noise piezo amplifier (Falco Systems WMA-200) that drives the ring piezo. Each of these stages has a specific frequency-dependent complex transfer function, defined as the ratio between the output and input voltages of that stage. Here and in the following, we will use interchangeably the words “gain” and “transfer function”. We define the transfer functions of the PI controller as $I(\omega)$, the piezo amplifier $A(\omega)$, the optical microcavity $C(\omega)$, and the photodiode $D(\omega)$. The product of these quantities, $G(\omega) = IACD$, is the open loop gain of the feedback loop, i.e., the ratio between the voltage measured on the photodiode and the voltage entering the PI controller, when the output of the photodiode is disconnected from the PI controller, i.e., when the feedback loop is open.

We now quantify the contribution of each individual stage in order to provide insight into the overall gain G . I is the gain of the PI controller, and it is given by $I(\omega) = 1/(j\omega\tau_I) + G_P$, where the frequency dependent part is given by the integrator and the

constant part is given by the proportional term. τ_I is the integration time, which is inversely proportional to the integral gain. The piezo amplifier has a gain $A(\omega) = A_0/(1 + j\omega/\omega_c)$, where $\omega_c = 2\pi f_c$. In our case, $A_0 = 20$, and the cutoff frequency is $f_c = 4600$ Hz when the amplifier is driving the ring piezo, which has a capacitance of 700 nF. The gain of the cavity $C(\omega)$ and the photodiode $D(\omega)$ are a bit more complicated, as they involve a conversion from the input voltage to different physical quantities.

First, the input voltage to the piezo results in a displacement based on the piezoelectric coefficient r_{piezo} [nm/V], then this displacement changes the cavity length, which in turn changes the amount of light power that is reflected back and sent to the photodiode, as shown in the inset of Fig. 5.2. This power is then converted into a voltage signal by the photodiode. Since we will lock the cavity at half of the reflection dip (side-of-fringe lock), which gives maximum sensitivity to changes in the cavity length, we determine the combined gain of the cavity and photodiode: $CD(\omega) = -r_{piezo} \times 2\eta V_0 F/\lambda$, where η is the coupling efficiency of the light to the cavity, F is the finesse, λ is the wavelength of the incident light, and V_0 is the voltage on the photodiode when the cavity is tuned off-resonance. This gain is different for different measurements since we vary the cavity finesse by adjusting the laser wavelength, which also changes the laser power and, consequently, V_0 . Moreover, the piezoelectric coefficient is $r_{piezo} = 3.8$ nm/V at room temperature but becomes a factor ~ 3 lower when operating the cavity at 4 K. As an example, at room temperature we have $CD = 7.1$ for $\lambda = 935$ nm, $F = 2500$, and a typical value of $V_0 = 0.7$ V and $\eta = 0.5$.

5.3.3 Identification of mechanical resonances

In reality, however, CD is not constant, and its frequency dependency can be used to find the mechanical resonances of the open cavity device. The ring piezo is mechanically coupled to the rest of the open cavity device and, therefore, to all its mechanical resonances.

Because of this, the piezoelectric coefficient r_{piezo} is, in fact, frequency dependent and will show a resonance–anti-resonance behavior in proximity to the mechanical resonances present in the system [153]. This shows up in the total open loop transfer function of the feedback loop, as shown in Fig. 5.3. This measurement has been done with a locked cavity, using a lock-in amplifier to apply a frequency-swept small modulation m to the input port of the PI controller and to measure the signal from the photodiode y , from which the open-loop gain G is calculated as

$$G(\omega) = \frac{H(\omega)}{1 + H(\omega)}, \text{ with } H(\omega) = \frac{y(\omega)}{m}. \quad (5.2)$$

By performing several measurements of the transfer function G while damping, removing, or changing the configuration of specific parts of the open-cavity device, we were able to identify the origin of several mechanical resonances and redesign the responsible components in order to remove or shift them to higher frequencies. After device optimization, we obtain the transfer function G shown in Fig. 5.3 of the device mounted in the cryostat at room temperature (red curve) and 4 K with the cryocooler on (blue curve).

The cryocooler leads to noise, particularly visible at low frequencies. We observe only a small shift and change in the resonance frequencies while cooling down. At 4 K, the first $-\pi$ phase crossing happens at 4.1 kHz, and the first unity gain frequency is at 8.58 kHz, while the feedback loop oscillation frequency is 22.8 kHz. For a simple system with

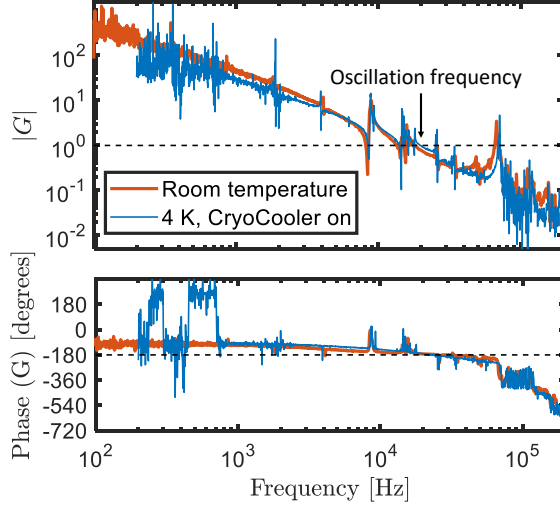


Figure 5.3: Measured amplitude and phase (unwrapped) of the feedback loop transfer function for two different conditions: device mounted in the cryostat with the cryocooler switched off at room temperature and ambient pressure (red), and at 4 K with the cryocooler on (blue). The positions of the mechanical resonances are not significantly shifted at low temperatures. The dashed lines correspond to unity gain and $-\pi$ phase, respectively; the feedback loop oscillates at 22.8 kHz if the gain is set too high.

only one mechanical resonance, these three frequencies would coincide, but our open-cavity device is more complex as there are many mechanical resonances coupled with the resonance of the ring piezo. We identified some of the resonances to be drum modes of the top plate (8.58, 14.3, 15.6, 26 and 35 kHz) but we were not able to pinpoint the origin of the resonances at 1.8, 2 and 4.1 kHz.

5.4 Stability at room temperature

To measure the stability of the cavity, we use the scheme shown in Fig. 5.2 but without the modulation signal m , and again lock the cavity to the laser frequency using a side-of-fringe lock. In particular, we lock the cavity at half the depth of the reflection dip, and we record ten time traces of 10 s of the photodiode signal at a sample rate of 200 kHz. After a proper calibration (see Appendix 5.7.2) we calculate the power spectral density (PSD) of these time traces, corresponding to fluctuations in the cavity length. In Fig. 5.4 we show data measured (i) on the optical table resting on air dampers, (ii) in the cryostat under vacuum, (iii) in the cryostat under vacuum with the cryocooler switched on but still at room temperature, and (iv) in the same conditions as (iii) but only considering the quiet periods of the cryocooler, corresponding to 40% of the full period. Panel (a) shows a section of the time traces, and (b) shows the corresponding PSDs. The finesse of the cavity is 1500, and the PI parameters are $\tau_I = 30 \mu\text{s}$, $G_P = 0.17$.

Comparing the measurements without a cryocooler, it is clear that the cavity length is more stable when the device is mounted directly on the optical table (yellow trace) than when it is mounted in the cryostat. The rms cavity length fluctuations integrated from 1 Hz to 100 kHz are $\Delta L_{rms} = 0.29 \text{ pm}$ on the optical table and $\Delta L_{rms} = 1.5 \text{ pm}$ mounted in the cryostat. This decrease in stability can be attributed to mechanical noise entering

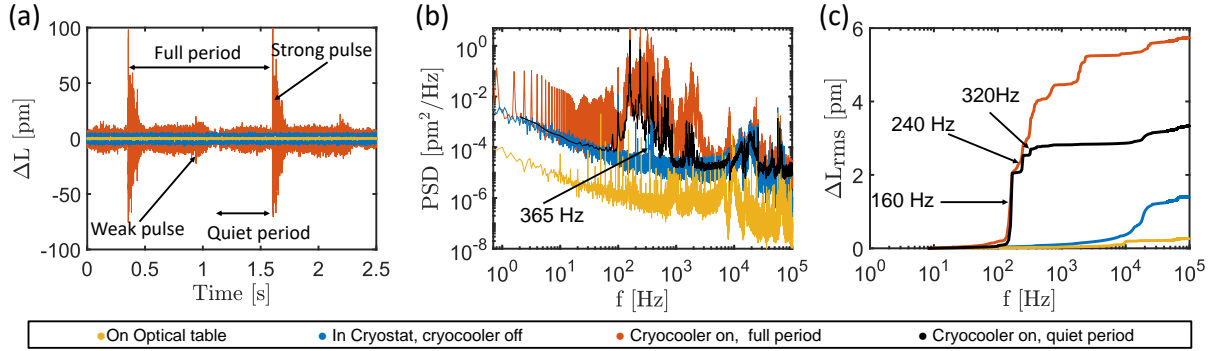


Figure 5.4: Room-temperature stability measurements of the open-cavity device for three different conditions: mounted on the optical table (yellow), mounted in the cryostat under vacuum (blue), and in the cryostat under vacuum and with the cryocooler switched on (red). Note that the measurement in yellow corresponds to an earlier version of the cavity device. (a) Time trace of the signal from the photodiode for a cavity locked at half of the reflection dip. (b) Power spectral density of the signal from the time traces. (c) Cumulative cavity length fluctuation as a function of frequency. The cavity finesse is $F = 1500$ in all cases.

the cavity through the connections of the cryostat to the rest of the lab environment (such as the high-pressure helium flex lines); this noise bypasses the low-pass filter of the optical table. The small peak at 365 Hz in the PSD (blue) in Fig. 5.4(b) corresponds to a mechanical resonance in the base of the cryostat.

Focusing on the measurement with the cryocooler switched on, the time traces show a strong and a weak pulse, both with a period of 1.25 s (0.8 Hz) separated by 0.625 s. In the PSD, we can see the harmonics of this frequency up to kHz frequencies. By calculating the PSD for different bandwidths, we can plot the cumulative cavity length fluctuation in Fig. 5.4(c), which enables the best understanding of the frequencies that contribute most to the mechanical noise.

Because of the large cavity length changes caused by the pulses of the cryocooler, here and in the rest of the paper, we define a quiet period between the weak pulse and the strong pulse, corresponding to 40% of the time between two strong pulses, and we will use it to calculate the PSD and noise characteristics of the cavity device [59, 142]. In this way, the PSD will also be cleaner, as all the cryocooler harmonics caused by the train of pulses in the time trace will be removed, and it will be easier to identify mechanical resonances.

The PSD and the cumulative rms noise are shown as black lines in Figs. 5.4(b) and 5.4(c). During the quiet period, we obtain an rms cavity length fluctuation of $\Delta L_{rms} = 3.4$ pm and 5.7 pm if measured over the full period of the cryocooler. As can be seen from the cumulative cavity length fluctuations, the major contribution to the mechanical noise comes from frequencies lower than 1 kHz, in particular 160, 240, and 320 Hz. These frequencies are not resonances of the cavity device, as they are not visible in the transfer function measurement shown in Fig. 5.3, and they appear in the cryostat measurements only when the cryocooler is switched on. Further evidence of this is presented in Appendix 5.7.1.

5.5 Stability in a closed-cycle cryostat at 4 K

Now we describe the cool-down, realignment, and measurements under cryogenic conditions. With the aid of a copper adapter plate, the open-cavity device is tightly mounted on the base of the closed-cycle cryostat. The cavity is aligned at room temperature using the nanopositioners and the external optics before the system is cooled down to 4 K. By monitoring the free spectral range of the cavity during cool-down, we observe a change in the cavity length of $\Delta L = 5.5 \mu\text{m}$. Once at 4 K, the cavity length can be readjusted with the three piezo motors if needed.

We control the finesse of the cavity by detuning the laser frequency, which changes the mirror reflectivity, such that we obtain the highest finesse cavity that can be locked despite the noise from the cryocooler. The PI parameters of the feedback system are well controlled, as described in Sec. II. In practice, the highest possible finesse is obtained when the peak-to-peak displacement of the cavity length caused by the cryocooler is slightly smaller than the FWHM of the reflection cavity resonance dip; beyond that, the lock is lost during every cryocooler cycle. We usually start with a laser frequency far detuned from the thin-film mirror stop-band center, locking the cavity and optimizing the PI parameters to minimize the mechanical noise in the cavity length, then slightly changing the laser frequency in order to increase the finesse of the cavity, and iterating the procedure until the PI controller is not able to keep the cavity locked.

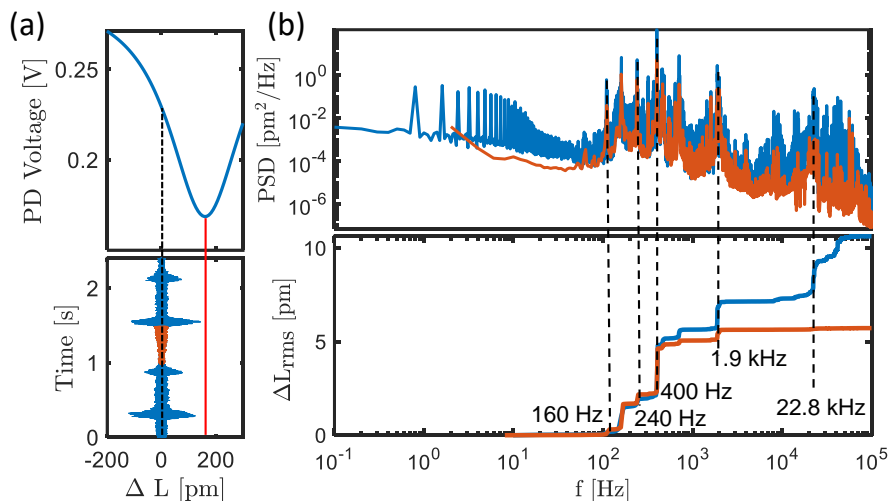


Figure 5.5: Stability measurement at 4 K for a cavity finesse $F = 1800$ ($\lambda = 990 \text{ nm}$). Panel (a) shows the calibration curve and a section of a time trace of the cavity length displacement. The red-highlighted part in (a) corresponds to the quiet period of the cryocooler. In (b), the PSD and cumulative noise correspond to the quiet period (red) and full period (blue) of the cryocooler. The rms mechanical noise is 5.7 pm in the quiet period and 10.6 pm in the full period.

The thin-film mirror design wavelength is 935 nm, resulting in a cavity finesse of 2500. In our case, the highest finesse we were able to achieve is 1800 at $\lambda = 990 \text{ nm}$, for which we have a stable lock that lasts for at least 2 days without any adjustment by using the PI parameters $\tau_I = 50 \mu\text{s}$ and $G_P = 0.03$. As described in the previous section, once the cavity is locked at half of the reflection dip, we record ten time traces, each 10 s long, of the photodiode signal. After converting this voltage signal into cavity length fluctuations

(see Appendix 5.7.2), we calculate the PSD and the cumulative integrated rms noise to identify the frequencies that contribute most strongly.

In Fig. 5.5(a), we show a reflection dip and a small portion of the calibrated time trace taken with a locked cavity, which represents the fluctuations of the cavity length from the locked position. The red vertical line corresponds to the maximum peak cavity length fluctuation that allows locking of the cavity, while the red-highlighted part of the time trace corresponds to the quiet period of the cryocooler (40% of the full period). Using the calibrated time trace, we calculate the power spectral density and the cumulative cavity length fluctuation for the quiet period (red) and the full period (blue) of the cryocooler, as shown in Fig. 5.5(b). The total rms mechanical noise in a 100 kHz bandwidth is 5.7 pm during the quiet period of the cryocooler and 10.6 pm during the full period. As it is clearly visible in the plot, also at 4 K, the major contribution to the noise comes from the same low frequencies that were present at room temperature with an operating cryocooler, in particular at 160 and 240 Hz. In addition, now there is also mechanical noise at 400 Hz, which we think is a mechanical resonance of the base of the cryostat that shifted from the room temperature value of 365 Hz.

Only a small part of the noise comes from resonances of the open-cavity device itself, one small contribution at 1.9 kHz (compare Fig. 5.3), and a contribution from 22.8 kHz, which is the oscillation frequency of the feedback loop. We note that the contribution from 22.8 kHz is significant only in the full period curve (blue) because the pulses from the cryocooler bring the feedback close to instability.

5.6 Conclusions and outlook

In conclusion, we have developed an open-access optical microcavity compatible with a tabletop optical closed-cycle cryostat. At 4 K, the open cavity device has stabilities of 5.7 and 10.6 pm rms during the quiet and full periods of the cryocooler cycle, respectively. The device allows for full nanometric but millimeter-range tunability of the cavity along the three spatial directions and two angles and requires only minimal optical realignment when cooling down to 4 K. The key to this is an extremely high-stiffness and compact design, which allows for active feedback stabilization of the cavity with very high bandwidth.

Most importantly, our design does not use a dedicated mechanical low-pass filter, which would complicate the integration of the cavity in a free-space optical setup, essential, for instance, for full polarization control. Nevertheless, a low-pass filter would increase the stability of our open-access optical microcavity. We estimate that a combination of a mechanical low-pass filter at around 50 Hz and electronic filtering in the feedback loop [153,154], will allow us to achieve at cryogenic temperatures the same cavity stability as on an optical table at room temperature.

Finally, we want to point out that for simultaneous locking of the open-access microcavity and operation of, e.g., a cavity-enhanced quantum dot single photon source, the locking laser has to be separated efficiently from the single photons. The micro-mirror array allows us to operate two spatially separate cavities with two different lasers simultaneously; then, one cavity can be used for stabilization and one for quantum dot spectroscopy.

5.7 Appendix

5.7.1 Comparison of cryocooler in low- and high-power mode

The Gifford-McMahon cryocooler used in our cryostat can be operated in low-power (LP) and high-power (HP) modes. We compare here the effects of the two different settings on the stability of the open-cavity device. As a result of the exchange of helium gas undergoing compression-expansion cycles, the cryocooler introduces mechanical noise in the open-cavity device in the form of pulses. The frequency of this cycle is 0.8 Hz for LP and 1.01 Hz for HP mode, corresponding to the frequency at which the compressed gas enters the regenerator through the high-pressure line. In the middle of the cycle, the helium gas expands and returns to the compressor. This results in two mechanical pulses per cycle of the base plate of the cryostat.

In Figs. 5.6(a) and 5.6(b) we show the fluctuation of the cavity length measured over time with the cryocooler in the LP and HP modes, where the cavity length is actively stabilized by locking at half of the reflection dip as explained in the main text. Each plot shows two kinds of pulses corresponding to the high and low pressure parts of the cycle. Comparing Fig. 5.6(b) to Fig. 5.6(a), we see that in addition to the higher frequency of the pulses, the peak-to-peak amplitude of the pulse is also higher as a result of the increased pressure difference of the helium. We calculated the power spectral density

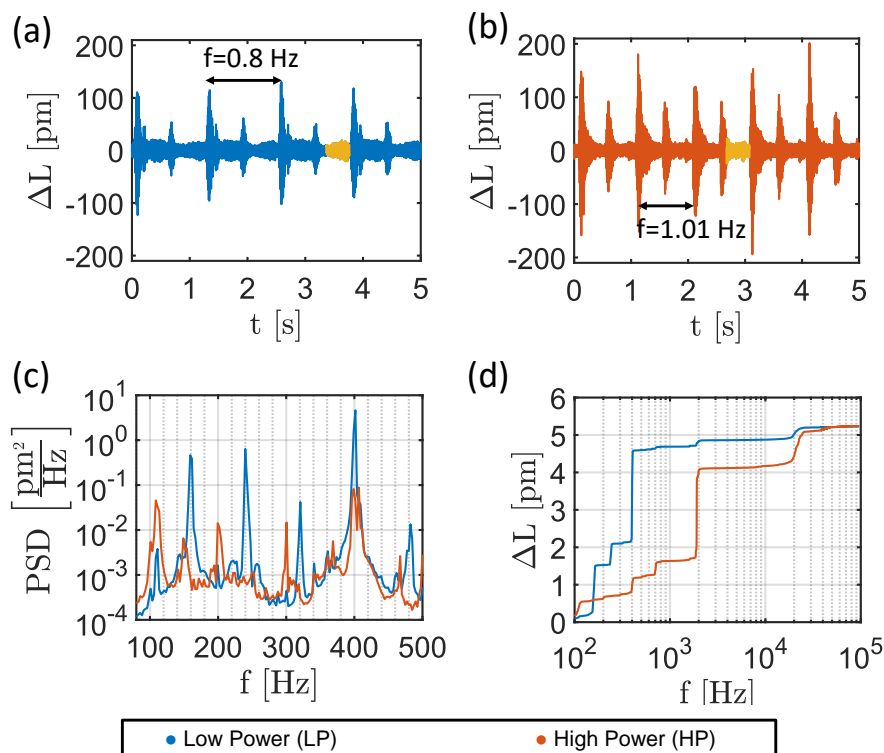


Figure 5.6: Comparison of low- and high-power modes. Panels (a) and (b) show the measured cavity length fluctuations as a function of time for LP (a) and HP (b) modes. The yellow portion of the data are used to calculate the PSD shown in (c) and the cumulative length fluctuations (d), with blue curves for LP and red curves for HP mode.

(PSD) as explained in the main text by considering the yellow sections of the time traces

in Figs. 5.6(a) and 5.6(b) which correspond to the quiet period, i.e. 40% of the cycle for the high power setting. We also considered the same section for the low power mode, so that the frequency separation of the points in the PSD is the same for both configurations, making a comparison easier. As explained in the main text, we take ten time traces of 10 seconds each. For each time trace, we select the yellow sections in each cycle of the cryocooler, calculate the PSD of each section, and finally, average them together. The result of this process is shown in Fig. 5.6(c), where we plot only a small frequency range of 80-500 Hz because outside of this range, there are not many differences between LP and HP modes, except for the peak heights. In particular, in both PSDs, we see a 400 Hz peak corresponding to a resonance of the base of the cryostat, as motivated in the main text. All other low frequency peaks that are visible in the LP mode (160, 240, and 320 Hz) are not present in the HP mode, where there are now three extra peaks at 150, 200, and 300 Hz, most likely harmonics of 50 Hz line noise.

Despite the fact that we do not know the exact origin of the peaks at 160, 240, and 320 Hz, we can conclude that it is the noise introduced by the cryocooler, and these peaks do not correspond to mechanical resonances in the system because otherwise, they should be visible with the cryocooler in HP mode. Because of the constant frequency separation between these peaks, one hypothesis is that they originate from the inverter used in the He compressor, as in LP mode the frequency of the inverter is 40 Hz.

Fig. 5.6(d) shows the cumulative cavity length fluctuation measured in the quiet period of the cryocooler cycle. The total rms noise $\Delta L_{rms} = 5.3$ pm is nearly the same for the two modi, despite the frequencies that contribute to the noise are different. We have used the same PI parameters for both measurements, optimized for the LP mode for minimum vibrations. The feedback loop is less stable in the HP mode due to a higher peak-to-peak amplitude of the pulses excited by the cryocooler, as visible in the 22.8 kHz peak corresponding to the oscillation frequency of the feedback loop.

5.7.2 Calibration of the photodiode signal

In order to measure the stability of the cavity device, we lock the cavity length to half of the reflection dip and record time traces of the voltage signal from the photodiode, as explained in the main text. This voltage must be multiplied by a conversion factor in order to give a measure of the cavity length. While this is trivial in the case of a quiet system where the cavity length does not change much and therefore this conversion factor is simply the slope of the reflection dip at the locking point, in the case of a mechanically noisy system, it is more complicated. In fact, when the cavity length changes significantly, the error signal cannot be approximated anymore as being linear, and in order to retrieve the exact cavity length, we must take the nonlinearities into account.

For this purpose, we calibrate the voltage signal of the photodiode V_{PD} as a function of the cavity length L , by linearly changing the latter via the ring piezo and recording the reflection dip, which is fitted with a Lorentzian,

$$V_{PD} = V_0 + \frac{A}{(L - L_0)^2 + \left(\frac{w}{2}\right)^2} . \quad (5.3)$$

Inverting the equation, we are able to obtain a conversion factor from photodiode voltage to cavity length,

$$L = L_0 \pm \sqrt{\frac{A}{V_{PD} - V_0} - \left(\frac{w}{2}\right)^2} , \quad (5.4)$$

where the \pm sign is chosen depending on whether the cavity is locked on the left or right side of the reflection dip. A , V_0 , L_0 and w are fitting parameters; w is the full width at half maximum of the reflection dip; and L_0 is the resonance cavity length, for which the reflection dip has its minimum.

While this procedure takes into account the nonlinearity of the error function, it still has some drawbacks: for calibration we scan the cavity length at a finite speed, and in the presence of vibrations, the shape of the reflection dip will change depending on the speed at which the cavity is scanned, leading to shifts in the position of the dip, broadening of the cavity reflection dip, and asymmetries. In Fig. 5.7(a), we demonstrate this effect. We have recorded four times a cavity dip, and we observe four very different results, with extracted finesses varying from 1100 to 4600. The real room-temperature finesse is measured to be $F = 2500$ at a wavelength $\lambda = 935$ nm. A simple way to deal with this is to measure the width of the reflection dip at room temperature without mechanical vibrations as a function of the wavelength of the laser and use this value to obtain the conversion factor of Eq. 5.4, as we expect the reflectivity of the mirrors to be constant from 300 to 4 K.

As an additional proof and to have a better understanding of the phenomena, we show here measurements of the shifts of the resonance widths and dips (w , L_0) and compare them to simulations. For the measurement, we recorded 150 reflection dips at 4 K with

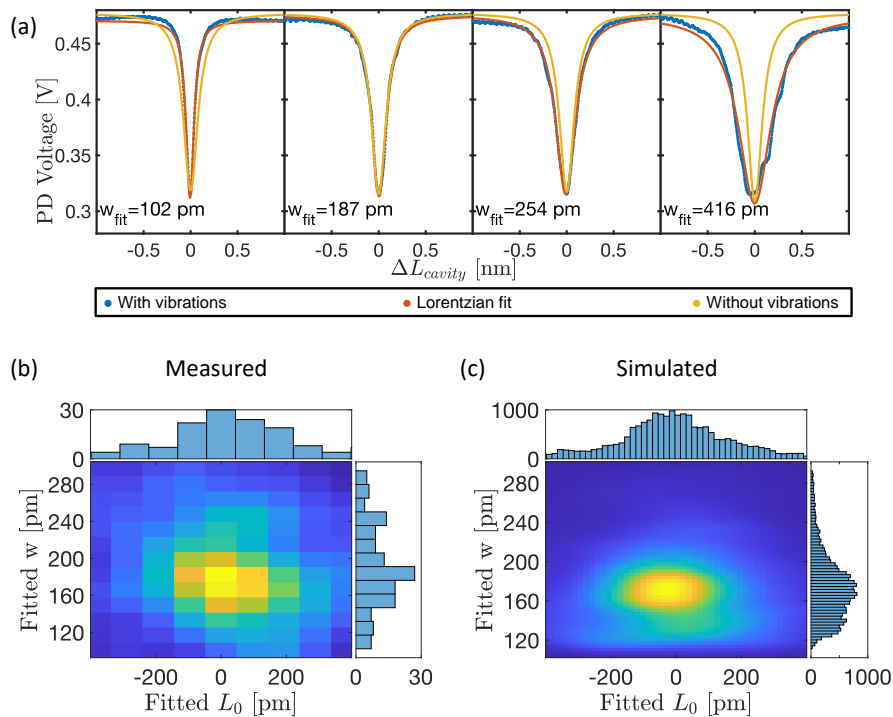


Figure 5.7: (a) In blue, four measurements of a cavity resonance recorded at 4 K with the cryocooler ON, with the same scanning speed but at different times of the cryocooler cycle. In red is the corresponding Lorentzian fit, and in yellow is the real cavity resonance measured at room temperature without vibrations. (b) Scatter plot and relative histograms of the fitted widths and positions of the cavity resonance, measured at 4 K. (c) Scatter plot and relative histograms of the fitted widths and positions of the cavity resonance, the result of a computer simulation.

the mechanical noise generated by the cryocooler by scanning the cavity length repeatedly with the ring piezo. We fit each reflection dip using Eq. 5.3, and we show the resulting scatter plot in Fig. 5.7(b). The data of the scatter plot have been convoluted with a Gaussian mask function with a width of 10 pm to smooth the data due to the low number of samples. The mean value for the width is $w_{mean} = 189$ pm, which is in very good agreement with the real value of 185 pm. The mean value for L_0 is around 0, as we shifted the data manually, since we do not know the real position of the resonance in the absence of vibrations. For the simulation, we used the power reflection coefficient of a Fabry-Perot cavity,

$$R(L) = \left| \frac{E_{reflected}}{E_{incident}} \right|^2 = \left| \frac{r \left(\exp \left(i \frac{4\pi L}{\lambda} \right) - 1 \right)}{1 - r^2 \exp \left(i \frac{4\pi L}{\lambda} \right)} \right|^2, \quad (5.5)$$

where $L = L_{piezo} + L_{noise}$. $L_{piezo} = v_{piezo} \times t$, and v_{piezo} is the scanning speed of the piezo. For L_{noise} we used the measured displacements from Fig. 5.6 (a) recorded with a cavity locked on the side of the reflection dip, where we compensated for the effect of the integrator: $L_{noise} = (1 + I) \times L_{noise}^{lock}$. We chose a mirror reflectivity $R = r^2 = 0.9988$, which correspond to a cavity with a finesse $F \sim 2600$, and a resonance width of $w \sim 178$ pm at the wavelength $\lambda = 935$ nm. For all other free parameters, such as v_{piezo} and the open loop gain of the integrator I , we have used experimental values.

We have simulated 20000 reflection dips using Eq. 5.5 by randomly shifting in time the experimental L_{noise} , and we fitted the curves with Eq. 5.3 in order to extract w_{fit} and L_0^{fit} . The results are shown in Fig. 5.7(c), where the data have been smoothed by convolution with a Gaussian mask function. The mean values are $w_{mean} = 179$ pm and $L_0^{mean} = -1.7$ pm. Visually, the distribution in Fig. 5.7(c) is clearly shifted toward negative L_0 . We hypothesize that this is because of the forces that keep together the two mirrors, i.e., gravity and the three metal springs holding together the top plate and the bottom part of the open cavity device. Since L_0 is the rest-length of the cavity, mechanical vibrations in the open-cavity device will exert sinusoidal forces that act in the same direction as gravity and the spring force for $L_0 < 0$, and in the opposite direction for $L_0 > 0$, causing the asymmetry visible in the histogram. The very good agreement between the measured data and the simulation, as well as the comparison to the reflection dip widths measured in the absence of noise, shows us that indeed we can calibrate the photodiode signal at 4 K with the parameters measured at room temperature for the same wavelength.

Bibliography

- [1] Rayleigh, L. On Waves Propagated along the Plane Surface of an Elastic Solid. *Proceedings of the London Mathematical Society* **s1-17**, 4 (1885).
- [2] Yamagata, M., Cao, N., John, D. D. & Hashemi, H. Surface-Acoustic-Wave Waveguides for Radio Frequency Signal Processing. *IEEE TRANSACTIONS ON MICROWAVE THEORY AND TECHNIQUES* **71** (2023).
- [3] Lewis, M. F. Surface Acoustic Wave Devices and Applications: 6. Oscillators — the next Successful Surface Acoustic Wave Device? *Ultrasonics* **12**, 115 (1974).
- [4] Campbell, C. Surface Acoustic Wave Convolver for Spread-Spectrum Mobile and Wireless Communications. In *1999 International Symposium on Electromagnetic Compatibility (IEEE Cat. No.99EX147)*, 686 (IEICE of Japan, Tokyo, Japan, 1999).
- [5] Lu, R., Yang, Y., Hassanien, A. E. & Gong, S. Gigahertz Low-Loss and High Power Handling Acoustic Delay Lines Using Thin-Film Lithium-Niobate-on-Sapphire. *IEEE Trans. Microwave Theory Techn.* **69**, 3246 (2021).
- [6] Delsing, P. *et al.* The 2019 Surface Acoustic Waves Roadmap. *J. Phys. D: Appl. Phys.* **52**, 353001 (2019).
- [7] Makkonen, T. *et al.* Fundamental Mode 5 GHz Surface-Acoustic-Wave Filters Using Optical Lithography. *Applied Physics Letters* **83**, 3596 (2003).
- [8] Hashimoto, K.-y. *Surface Acoustic Wave Devices in Telecommunications* (Springer Berlin Heidelberg, Berlin, Heidelberg, 2000).
- [9] Go, D. B., Atashbar, M. Z., Ramshani, Z. & Chang, H.-C. Surface Acoustic Wave Devices for Chemical Sensing and Microfluidics: A Review and Perspective. *Anal. Methods* **9**, 4112 (2017).
- [10] Wixforth, A. Acoustically Driven Planar Microfluidics. *Superlattices and Microstructures* **33**, 389 (2003).
- [11] Franke, T., Braunmüller, S., Schmid, L., Wixforth, A. & Weitz, D. A. Surface Acoustic Wave Actuated Cell Sorting (SAWACS). *Lab Chip* **10**, 789 (2010).
- [12] Huang, Y., Das, P. K. & Bhethanabotla, V. R. Surface Acoustic Waves in Biosensing Applications. *Sensors and Actuators Reports* **3**, 100041 (2021).
- [13] Baumgartner, K., Täufer, P., Lienhart, M., Lienhart, R. & Westerhausen, C. Pulsed Surface Acoustic Waves Accelerate Wound Healing and Reveal New Parameter Limits for Cell Stimulation in Vitro. *J. Phys. D: Appl. Phys.* **57**, 155401 (2024).

- [14] Paschke, B., Wixforth, A., Denysenko, D. & Volkmer, D. Fast Surface Acoustic Wave-Based Sensors to Investigate the Kinetics of Gas Uptake in Ultra-Microporous Frameworks. *ACS Sens.* **2**, 740 (2017).
- [15] DeCrescent, R. A. *et al.* Coherent Control of an Optical Quantum Dot Using Phonons and Photons (2024). arXiv: 2404.02079.
- [16] Lienhart, M. *et al.* Heterogeneous Integration of Superconducting Thin Films and Epitaxial Semiconductor Heterostructures with Lithium Niobate. *J. Phys. D: Appl. Phys.* **56**, 365105 (2023).
- [17] Weig, E. M. *et al.* Single-Electron-Phonon Interaction in a Suspended Quantum Dot Phonon Cavity. *Phys. Rev. Lett.* **92**, 046804 (2004).
- [18] Weiß, M. *et al.* Optomechanical Wave Mixing by a Single Quantum Dot. *Optica* **8**, 291 (2021).
- [19] Choquer, M. *et al.* Quantum Control of Optically Active Artificial Atoms With Surface Acoustic Waves. *IEEE Trans. Quantum Eng.* **3**, 1 (2022).
- [20] DeCrescent, R. A. *et al.* Large Single-Phonon Optomechanical Coupling Between Quantum Dots and Tightly Confined Surface Acoustic Waves in the Quantum Regime. *Phys. Rev. Appl.* **18**, 034067 (2022).
- [21] Metcalfe, M., Carr, S. M., Muller, A., Solomon, G. S. & Lawall, J. Resolved Sideband Emission of InAs / GaAs Quantum Dots Strained by Surface Acoustic Waves. *Phys. Rev. Lett.* **105**, 037401 (2010).
- [22] Gustafsson, M. V. *et al.* Propagating Phonons Coupled to an Artificial Atom. *Science* **346**, 207 (2014).
- [23] Manenti, R. *et al.* Circuit Quantum Acoustodynamics with Surface Acoustic Waves. *Nat Commun* **8**, 975 (2017).
- [24] Moores, B. A., Sletten, L. R., Viennot, J. J. & Lehnert, K. W. Cavity Quantum Acoustic Device in the Multimode Strong Coupling Regime. *Phys. Rev. Lett.* **120**, 227701 (2018).
- [25] Satzinger, K. J. *et al.* Quantum Control of Surface Acoustic-Wave Phonons. *Nature* **563**, 661 (2018).
- [26] Golter, D. A., Oo, T., Amezcua, M., Stewart, K. A. & Wang, H. Optomechanical Quantum Control of a Nitrogen-Vacancy Center in Diamond. *Phys. Rev. Lett.* **116**, 143602 (2016).
- [27] Hernández-Mínguez, A., Poshakinskiy, A. V., Hollenbach, M., Santos, P. V. & Astakhov, G. V. Acoustically Induced Coherent Spin Trapping. *Science Advances* **7**, eabj5030 (2021).
- [28] Whiteley, S. J. *et al.* Spin-Phonon Interactions in Silicon Carbide Addressed by Gaussian Acoustics. *Nat. Phys.* **15**, 490 (2019).
- [29] Schuetz, M. J. A. *et al.* Universal Quantum Transducers Based on Surface Acoustic Waves. *Phys. Rev. X* **5**, 031031 (2015).

- [30] Midolo, L., Schliesser, A. & Fiore, A. Nano-Opto-Electro-Mechanical Systems. *Nature Nanotech* **13**, 11 (2018).
- [31] Clerk, A. A., Lehnert, K. W., Bertet, P., Petta, J. R. & Nakamura, Y. Hybrid Quantum Systems with Circuit Quantum Electrodynamics. *Nat. Phys.* **16**, 257 (2020).
- [32] Blésin, T., Tian, H., Bhave, S. A. & Kippenberg, T. J. Quantum Coherent Microwave-Optical Transduction Using High-Overtone Bulk Acoustic Resonances. *Phys. Rev. A* **104**, 052601 (2021).
- [33] Forsch, M. *et al.* Microwave-to-Optics Conversion Using a Mechanical Oscillator in Its Quantum Ground State. *Nat. Phys.* **16**, 69 (2020).
- [34] Lauk, N. *et al.* Perspectives on Quantum Transduction. *Quantum Sci. Technol.* **5**, 020501 (2020).
- [35] Tsuchimoto, Y. *et al.* Large-Bandwidth Transduction Between an Optical Single Quantum Dot Molecule and a Superconducting Resonator. *PRX Quantum* **3**, 030336 (2022).
- [36] van Thiel, T. C. *et al.* Optical Readout of a Superconducting Qubit Using a Scalable Piezo-Optomechanical Transducer (2023). arXiv: 2310.06026.
- [37] Weaver, M. J. *et al.* An Integrated Microwave-to-Optics Interface for Scalable Quantum Computing. *Nat. Nanotechnol.* **19**, 166 (2024).
- [38] Bienfait, A. *et al.* Quantum Erasure Using Entangled Surface Acoustic Phonons. *Phys. Rev. X* **10**, 021055 (2020).
- [39] Bienfait, A. *et al.* Phonon-Mediated Quantum State Transfer and Remote Qubit Entanglement. *Science* **364**, 368 (2019).
- [40] Dumur, É. *et al.* Quantum Communication with Itinerant Surface Acoustic Wave Phonons. *npj Quantum Inf* **7**, 1 (2021).
- [41] White, R. M. & Voltmer, F. W. DIRECT PIEZOELECTRIC COUPLING TO SURFACE ELASTIC WAVES. *Applied Physics Letters* **7**, 314 (1965).
- [42] Royer, D. & Dieulesaint, E. *Elastic Waves in Solids II: Generation, Acousto-Optic Interaction, Applications* (Springer Science & Business Media, 1999).
- [43] ROYER, DANIEL. & Dieulesaint, E. *Elastic Waves in Solids I: Free and Guided Propagation* (Springer Science & Business Media, 1999).
- [44] Ekström, M. K. *et al.* Surface Acoustic Wave Unidirectional Transducers for Quantum Applications. *Applied Physics Letters* **110**, 073105 (2017).
- [45] Dumur, É. *et al.* Unidirectional Distributed Acoustic Reflection Transducers for Quantum Applications. *Applied Physics Letters* **114**, 223501 (2019).
- [46] Tsung-Tsong Wu, He-Tai Tang, Yung-Yu Chen & Pei-Ling Liu. Analysis and Design of Focused Interdigital Transducers. *IEEE Trans. Ultrason., Ferroelect., Freq. Contr.* **52**, 1384 (2005).

- [47] Lima, M. M. D. & Santos, P. V. Modulation of Photonic Structures by Surface Acoustic Waves. *Rep. Prog. Phys.* **68**, 1639 (2005).
- [48] Bell, D. & Li, R. Surface-Acoustic-Wave Resonators. *Proc. IEEE* **64**, 711 (1976).
- [49] Li, R., Alusow, J. & Williamson, R. Experimental Exploration of the Limits of Achievable Q of Grooved Surface-Wave Resonators. In *1975 Ultrasonics Symposium*, 279 (IEEE, 1975).
- [50] Tanski, W. GHz SAW Resonators. In *1979 Ultrasonics Symposium*, 815 (IEEE, 1979).
- [51] Andersson, G. *et al.* Squeezing and Multimode Entanglement of Surface Acoustic Wave Phonons. *PRX Quantum* **3**, 010312 (2022).
- [52] Msall, M. E. & Santos, P. V. Focusing Surface-Acoustic-Wave Microcavities on Ga As. *Phys. Rev. Applied* **13**, 014037 (2020).
- [53] Thomas, S. E. *et al.* Bright Polarized Single-Photon Source Based on a Linear Dipole. *Phys. Rev. Lett.* **126**, 233601 (2021).
- [54] Somaschi, N. *et al.* Near-Optimal Single-Photon Sources in the Solid State. *Nature Photon* **10**, 340 (2016).
- [55] Snijders, H. *et al.* Fiber-Coupled Cavity-QED Source of Identical Single Photons. *Phys. Rev. Applied* **9**, 031002 (2018).
- [56] Tomm, N. *et al.* A Bright and Fast Source of Coherent Single Photons. *Nat. Nanotechnol.* **16**, 399 (2021).
- [57] Ding, X. *et al.* High-Efficiency Single-Photon Source above the Loss-Tolerant Threshold for Efficient Linear Optical Quantum Computing (2023). arXiv: 2311.08347.
- [58] Greuter, L. *et al.* A Small Mode Volume Tunable Microcavity: Development and Characterization. *Appl. Phys. Lett.* **105**, 121105 (2014).
- [59] Pallmann, M. *et al.* A Highly Stable and Fully Tunable Open Microcavity Platform at Cryogenic Temperatures. *APL Photonics* **8**, 046107 (2023).
- [60] Fisicaro, M., Witlox, M., van der Meer, H. & Löffler, W. Active Stabilization of an Open-Access Optical Microcavity for Low-Noise Operation in a Standard Closed-Cycle Cryostat. *Review of Scientific Instruments* **95**, 033101 (2024).
- [61] Joshi, S. G. & White, R. M. Excitation and Detection of Surface Elastic Waves in Piezoelectric Crystals. *The Journal of the Acoustical Society of America* **46**, 17 (1969).
- [62] Chen, Z. *et al.* Ultrahigh-Frequency Surface Acoustic Wave Sensors with Giant Mass-Loading Effects on Electrodes. *ACS Sens.* **5**, 1657 (2020).
- [63] Grate, J. W. Acoustic Wave Microsensor Arrays for Vapor Sensing. *Chem. Rev.* **100**, 2627 (2000).

- [64] Länge, K., Rapp, B. E. & Rapp, M. Surface Acoustic Wave Biosensors: A Review. *Anal Bioanal Chem* **391**, 1509 (2008).
- [65] Guo, F. *et al.* Controlling Cell–Cell Interactions Using Surface Acoustic Waves. *Proceedings of the National Academy of Sciences* **112**, 43 (2015).
- [66] Collins, D. J. *et al.* Two-Dimensional Single-Cell Patterning with One Cell per Well Driven by Surface Acoustic Waves. *Nat Commun* **6**, 8686 (2015).
- [67] Takai, T. *et al.* High-Performance SAW Resonator on New Multilayered Substrate Using LiTaO₃ Crystal. *IEEE Trans. Ultrason., Ferroelect., Freq. Contr.* **64**, 1382 (2017).
- [68] Yang, K. *et al.* Advanced RF Filters for Wireless Communications. *Chip* **2**, 100058 (2023).
- [69] Weiß, M. & Krenner, H. J. Interfacing Quantum Emitters with Propagating Surface Acoustic Waves. *J. Phys. D: Appl. Phys.* **51**, 373001 (2018).
- [70] Sato, Y., Chen, J. C. H., Hashisaka, M., Muraki, K. & Fujisawa, T. Two-Electron Double Quantum Dot Coupled to Coherent Photon and Phonon Fields. *Phys. Rev. B* **96**, 115416 (2017).
- [71] Manenti, R. *et al.* Surface Acoustic Wave Resonators in the Quantum Regime. *Phys. Rev. B* **93**, 041411 (2016).
- [72] Takasu, R. *et al.* Surface-Acoustic-Wave Resonators with Ti, Cr, and Au Metallization on GaAs. *Appl. Phys. Express* **12**, 055001 (2019).
- [73] Luschmann, T. *et al.* Surface Acoustic Wave Resonators on Thin Film Piezoelectric Substrates in the Quantum Regime. *Mater. Quantum. Technol.* **3**, 021001 (2023).
- [74] Camara, I. S. *et al.* Vector Network Analyzer Measurement of the Amplitude of an Electrically Excited Surface Acoustic Wave and Validation by X-ray Diffraction. *Journal of Applied Physics* **121**, 044503 (2017).
- [75] Hellemann, J., Müller, F., Msall, M., Santos, P. V. & Ludwig, S. Determining Amplitudes of Standing Surface Acoustic Waves via Atomic Force Microscopy. *Phys. Rev. Applied* **17**, 044024 (2022).
- [76] Goddard, P. A., Clark, G. F., Tanner, B. K. & Whatmore, R. W. Stroboscopic Synchrotron-X-radiation Topography and Its Application to the Imaging of Traveling Surface Acoustic Waves. *Nuclear Instruments and Methods in Physics Research* **208**, 705 (1983).
- [77] Nicolas, J.-D. *et al.* Time-Resolved Coherent X-ray Diffraction Imaging of Surface Acoustic Waves. *J Appl Crystallogr* **47**, 1596 (2014).
- [78] Hanke, M. *et al.* Scanning X-ray Diffraction Microscopy of a 6 GHz Surface Acoustic Wave. *Phys. Rev. Applied* **19**, 024038 (2023).
- [79] Gualtieri, J. & Kosinski, J. Large-Area, Real-Time Imaging System for Surface Acoustic Wave Devices. *IEEE Transactions on Instrumentation and Measurement* **45**, 872 (1996).

- [80] Hisatomi, R. *et al.* Quantitative Optical Imaging Method for Surface Acoustic Waves Using Optical Path Modulation. *Phys. Rev. B* **107**, 165416 (2023).
- [81] Iwasaki, A. *et al.* Temporal-Offset Dual-Comb Vibrometer with Picometer Axial Precision. *APL Photonics* **7**, 106101 (2022).
- [82] Kamizuma, H., Yang, L., Omori, T., Hashimoto, K.-y. & Yamaguchi, M. High-Speed Laser Probing System for Surface Acoustic Wave Devices Based on Knife-Edge Method. *Jpn. J. Appl. Phys.* **44**, 4535 (2005).
- [83] Taga, K. *et al.* Optical Polarimetric Measurement of Surface Acoustic Waves. *Applied Physics Letters* **119**, 181106 (2021).
- [84] Rummel, B. D. *et al.* Imaging of Surface Acoustic Waves on GaAs Using 2D Confocal Raman Microscopy and Atomic Force Microscopy. *Applied Physics Letters* **118**, 031602 (2021).
- [85] Knuuttila, J. V., Tikka, P. T. & Salomaa, M. M. Scanning Michelson Interferometer for Imaging Surface Acoustic Wave Fields. *Opt. Lett., OL* **25**, 613 (2000).
- [86] Kokkonen, K. & Kaivola, M. Scanning Heterodyne Laser Interferometer for Phase-Sensitive Absolute-Amplitude Measurements of Surface Vibrations. *Applied Physics Letters* **92**, 063502 (2008).
- [87] Gollwitzer, A., Lerner, A. & Fischerauer, G. Interferometric Observation of Surface Acoustic Wave Phase Fronts. In *2006 IEEE International Frequency Control Symposium and Exposition*, 424 (2006).
- [88] Hashimoto, K.-y. *et al.* A Laser Probe Based on a Sagnac Interferometer with Fast Mechanical Scan for RF Surface and Bulk Acoustic Wave Devices. *IEEE Transactions on Ultrasonics, Ferroelectrics, and Frequency Control* **58**, 187 (2011).
- [89] Takahashi, H., Omori, T. & Hashimoto, K.-y. Development of a High-Speed, Phase-Sensitive Laser Probe System for RF Surface Acoustic Wave/Bulk Acoustic Wave Devices with an Absolute Vibration Amplitude Measurement Function. *Jpn. J. Appl. Phys.* **60**, SDDC10 (2021).
- [90] Arnaud, J. A. *et al.* Technique for Fast Measurement of Gaussian Laser Beam Parameters. *Appl. Opt., AO* **10**, 2775 (1971).
- [91] Skinner, D. R. & Witcher, R. E. Measurement of the Radius of a High-Power Laser Beam near the Focus of a Lens. *J. Phys. E: Sci. Instrum.* **5**, 237 (1972).
- [92] Campbell, C. Modelling the Transverse-Mode Response of a Two-Port SAW Resonator. *IEEE Trans. Ultrason., Ferroelect., Freq. Contr.* **38**, 237 (1991).
- [93] Aspelmeyer, M., Kippenberg, T. J. & Marquardt, F. Cavity Optomechanics. *Rev. Mod. Phys.* **86**, 1391 (2014).
- [94] Naumenko, N. Laterally Excited Bulk Acoustic Resonators (XBARs): Optimization Method and Application to Resonators on LiTaO₃. In *2022 IEEE MTT-S International Conference on Microwave Acoustics and Mechanics (IC-MAM)*, 70 (2022).

- [95] Yandrapalli, S., Eroglu, S. E. K., Plessky, V., Atakan, H. B. & Villanueva, L. G. Study of Thin Film LiNbO₃ Laterally Excited Bulk Acoustic Resonators. *J. Microelectromech. Syst.* **31**, 217 (2022).
- [96] Magnusson, E. B. *et al.* Surface Acoustic Wave Devices on Bulk ZnO Crystals at Low Temperature. *Applied Physics Letters* **106**, 063509 (2015).
- [97] Imany, P. *et al.* Quantum Phase Modulation with Acoustic Cavities and Quantum Dots. *Optica* **9**, 501 (2022).
- [98] Maity, S. *et al.* Coherent Acoustic Control of a Single Silicon Vacancy Spin in Diamond. *Nat Commun* **11**, 193 (2020).
- [99] Tanski, W. Surface Acoustic Wave Resonators on Quartz. *IEEE Trans. Son. Ultrason.* **26**, 93 (1979).
- [100] Ebata, Y. Suppression of Bulk-Scattering Loss in SAW Resonator with Quasi-Constant Acoustic Reflection Periodicity. In *IEEE 1988 Ultrasonics Symposium Proceedings.*, 91 (IEEE, Chicago, IL, USA, 1988).
- [101] Haus, H. Bulk Scattering Loss Of SAW Grating Cascades. *IEEE Trans. Son. Ultrason.* **24**, 259 (1977).
- [102] Islam, M., Haus, H. & Melngailis, J. Bulk Radiation by Surface Acoustic Waves Propagating Under a Grating. *IEEE Trans. Son. Ultrason.* **31**, 123 (1984).
- [103] Ronnekleiv, A. & Souquet, J. Surface Wave to Bulk Wave Scattering from Grooves. In *1975 Ultrasonics Symposium*, 434 (IEEE, 1975).
- [104] Schmidt, R. V. Excitation of Shear Elastic Waves by an Interdigital Transducer Operated at Its Surface-Wave Center Frequency. *Journal of Applied Physics* **43**, 2498 (1972).
- [105] Knuuttila, J. V. *et al.* Bulk-Acoustic Waves Radiated from Low-Loss Surface-Acoustic-Wave Resonators. *Applied Physics Letters* **84**, 1579 (2004).
- [106] Hunt, W. D., Miller, R. L. & Hunsinger, B. J. Slowness Surface Measurements for Zero- and Five-Degree [100]-Cut GaAs. *Journal of Applied Physics* **60**, 3532 (1986).
- [107] Kuok, M. H., Ng, S. C. & Zhang, V. L. Angular Dispersion of Surface Acoustic Waves on (001), (110), and (111) GaAs. *Journal of Applied Physics* **89**, 7899 (2001).
- [108] Maznev, A. A., Lomonosov, A. M., Hess, P. & Kolomenskii, A. A. Anisotropic Effects in Surface Acoustic Wave Propagation from a Point Source in a Crystal. *Eur. Phys. J. B* **35**, 429 (2003).
- [109] Montgomery, W. D. Self-Imaging Objects of Infinite Aperture*. *J. Opt. Soc. Am., JOSA* **57**, 772 (1967).
- [110] Patorski, K. I The Self-Imaging Phenomenon and Its Applications. In Wolf, E. (ed.) *Progress in Optics*, vol. 27, 1 (Elsevier, 1989).

- [111] Wen, J., Zhang, Y. & Xiao, M. The Talbot Effect: Recent Advances in Classical Optics, Nonlinear Optics, and Quantum Optics. *Adv. Opt. Photon., AOP* **5**, 83 (2013).
- [112] Talbot, H. LXXVI. Facts Relating to Optical Science. No. IV. *The London, Edinburgh, and Dublin Philosophical Magazine and Journal of Science* **9**, 401 (1836).
- [113] Rayleigh, L. XXV. On Copying Diffraction-Gratings, and on Some Phenomena Connected Therewith (1881).
- [114] Chapman, M. S. *et al.* Near-Field Imaging of Atom Diffraction Gratings: The Atomic Talbot Effect. *Phys. Rev. A* **51**, R14 (1995).
- [115] Song, X.-B. *et al.* Experimental Observation of Quantum Talbot Effects. *Phys. Rev. Lett.* **107**, 033902 (2011).
- [116] Candelas, P., Fuster, J. M., Pérez-López, S., Uris, A. & Rubio, C. Observation of Ultrasonic Talbot Effect in Perforated Plates. *Ultrasonics* **94**, 281 (2019).
- [117] Bakman, A., Fishman, S., Fink, M., Fort, E. & Wildeman, S. Observation of the Talbot Effect with Water Waves. *American Journal of Physics* **87**, 38 (2019).
- [118] Gao, T. *et al.* Talbot Effect for Exciton Polaritons. *Phys. Rev. Lett.* **117**, 097403 (2016).
- [119] Zhang, Y., Wen, J., Zhu, S. N. & Xiao, M. Nonlinear Talbot Effect. *Phys. Rev. Lett.* **104**, 183901 (2010).
- [120] Rozenman, G. G., Schleich, W. P., Shemer, L. & Arie, A. Periodic Wave Trains in Nonlinear Media: Talbot Revivals, Akhmediev Breathers, and Asymmetry Breaking. *Phys. Rev. Lett.* **128**, 214101 (2022).
- [121] Mamishev, A., Sundara-Rajan, K., Fumin Yang, Yanqing Du & Zahn, M. Interdigital Sensors and Transducers. *Proc. IEEE* **92**, 808 (2004).
- [122] Yamanouchi, K., Cho, Y. & Meguro, T. SHF-range Surface Acoustic Wave Interdigital Transducers Using Electron Beam Exposure. In *IEEE 1988 Ultrasonics Symposium Proceedings.*, 115 (1988).
- [123] Büyükköse, S., Vratzov, B., van der Veen, J., Santos, P. V. & van der Wiel, W. G. Ultrahigh-Frequency Surface Acoustic Wave Generation for Acoustic Charge Transport in Silicon. *Applied Physics Letters* **102**, 013112 (2013).
- [124] Wang, L. *et al.* High Performance 33.7 GHz Surface Acoustic Wave Nanotransducers Based on AlScN/Diamond/Si Layered Structures. *Applied Physics Letters* **113**, 093503 (2018).
- [125] Shao, L. *et al.* Phononic Band Structure Engineering for High-Q Gigahertz Surface Acoustic Wave Resonators on Lithium Niobate. *Phys. Rev. Appl.* **12**, 014022 (2019).
- [126] Szapiel, S. & Patorski, K. Fresnel Diffraction Images of Periodic Objects under Gaussian Beam Illumination. *Optica Acta: International Journal of Optics* **26**, 439 (1979).

- [127] Vahala, K. J. Optical Microcavities. *Nature* **424**, 839 (2003).
- [128] Ding, X. *et al.* On-Demand Single Photons with High Extraction Efficiency and Near-Unity Indistinguishability from a Resonantly Driven Quantum Dot in a Microcavity. *Phys. Rev. Lett.* **116**, 020401 (2016).
- [129] Evans, R. E. *et al.* Photon-Mediated Interactions between Quantum Emitters in a Diamond Nanocavity. *Science* **362**, 662 (2018).
- [130] Kimble, H. J. The Quantum Internet. *Nature* **453**, 1023 (2008).
- [131] Cirac, J. I., Zoller, P., Kimble, H. J. & Mabuchi, H. Quantum State Transfer and Entanglement Distribution among Distant Nodes in a Quantum Network. *Phys. Rev. Lett.* **78**, 3221 (1997).
- [132] Northup, T. E. & Blatt, R. Quantum Information Transfer Using Photons. *Nature Photon* **8**, 356 (2014).
- [133] Bonato, C. *et al.* CNOT and Bell-state Analysis in the Weak-Coupling Cavity QED Regime. *Phys. Rev. Lett.* **104**, 160503 (2010).
- [134] Hacker, B., Welte, S., Rempe, G. & Ritter, S. A Photon–Photon Quantum Gate Based on a Single Atom in an Optical Resonator. *Nature* **536**, 193 (2016).
- [135] Trupke, M. *et al.* Microfabricated High-Finesse Optical Cavity with Open Access and Small Volume. *Appl. Phys. Lett.* **87**, 211106 (2005).
- [136] Barbour, R. J. *et al.* A Tunable Microcavity. *Journal of Applied Physics* **110**, 053107 (2011).
- [137] Wachter, G. *et al.* Silicon Microcavity Arrays with Open Access and a Finesse of Half a Million. *Light Sci Appl* **8**, 37 (2019).
- [138] Najer, D. *et al.* A Gated Quantum Dot Strongly Coupled to an Optical Microcavity. *Nature* **575**, 622 (2019).
- [139] Koks, C., Baalbergen, F. B. & van Exter, M. P. Observation of Microcavity Fine Structure. *Phys. Rev. A* **105**, 063502 (2022).
- [140] Mader, M., Reichel, J., Hänsch, T. W. & Hunger, D. A Scanning Cavity Microscope. *Nat Commun* **6**, 7249 (2015).
- [141] Vadia, S. *et al.* Open-Cavity in Closed-Cycle Cryostat as a Quantum Optics Platform. *PRX Quantum* **2**, 040318 (2021).
- [142] Fontana, Y., Zifkin, R., Janitz, E., Rodríguez Rosenblueth, C. D. & Childress, L. A Mechanically Stable and Tunable Cryogenic Fabry–Pérot Microcavity. *Review of Scientific Instruments* **92**, 053906 (2021).
- [143] Bogdanović, S. *et al.* Design and Low-Temperature Characterization of a Tunable Microcavity for Diamond-Based Quantum Networks. *Appl. Phys. Lett.* **110**, 171103 (2017).

- [144] Chen, C. J. *Introduction to Scanning Tunneling Microscopy: Second Edition*. Monographs on the Physics and Chemistry of Materials (Oxford University Press, Oxford, 2007).
- [145] Hackley, J. D., Kislitsyn, D. A., Beaman, D. K., Ulrich, S. & Nazin, G. V. High-Stability Cryogenic Scanning Tunneling Microscope Based on a Closed-Cycle Cryostat. *Review of Scientific Instruments* **85**, 103704 (2014).
- [146] Battisti, I., Verdoes, G., van Oosten, K., Bastiaans, K. M. & Allan, M. P. Definition of Design Guidelines, Construction, and Performance of an Ultra-Stable Scanning Tunneling Microscope for Spectroscopic Imaging. *Review of Scientific Instruments* **89**, 123705 (2018).
- [147] Mashoff, T., Pratzner, M. & Morgenstern, M. A Low-Temperature High Resolution Scanning Tunneling Microscope with a Three-Dimensional Magnetic Vector Field Operating in Ultrahigh Vacuum. *Review of Scientific Instruments* **80**, 053702 (2009).
- [148] Fedoseev, V., Fisicaro, M., van der Meer, H., Löffler, W. & Bouwmeester, D. Realignment-Free Cryogenic Macroscopic Optical Cavity Coupled to an Optical Fiber. *Review of Scientific Instruments* **93**, 013103 (2022).
- [149] Bechhoefer, J. Feedback for Physicists: A Tutorial Essay on Control. *Rev. Mod. Phys.* **77**, 783 (2005).
- [150] Reinhardt, C., Müller, T. & Sankey, J. C. Simple Delay-Limited Sideband Locking with Heterodyne Readout. *Opt. Express* **25**, 1582 (2017).
- [151] Janitz, E., Ruf, M., Fontana, Y., Sankey, J. & Childress, L. High Mechanical Bandwidth Fiber-Coupled Fabry-Perot Cavity. *Opt. Express, OE* **25**, 20932 (2017).
- [152] Saavedra, C., Pandey, D., Alt, W., Pfeifer, H. & Meschede, D. Tunable Fiber Fabry-Perot Cavities with High Passive Stability. *Opt. Express* **29**, 974 (2021).
- [153] Ryou, A. & Simon, J. Active Cancellation of Acoustical Resonances with an FPGA FIR Filter. *Review of Scientific Instruments* **88**, 013101 (2017).
- [154] Okada, M. *et al.* Extending the Piezoelectric Transducer Bandwidth of an Optical Interferometer by Suppressing Resonance Using a High Dimensional IIR Filter Implemented on an FPGA. *Review of Scientific Instruments* **91**, 055102 (2020).

Summary

Surface acoustic waves are mechanical waves that are confined to the surface of a material. These waves occur naturally during earthquakes and have also been engineered for use in miniaturized devices, playing a crucial role in sensing and processing of ultra-high-frequency electric signals. Artificial surface acoustic waves typically operate at frequencies of hundreds of MHz or higher, with wavelengths on the micrometer scale, and surface displacements of hundreds of picometers - comparable to the size of an atom.

Excitation of these waves can be done via electromechanical conversion by an interdigital transducer on a piezoelectric material. Surface acoustic waves can have very low loss which, in combination with the ability to couple to a number of quantum systems via strain or electric fields in piezoelectric materials, has recently enabled exploration of the field of quantum acoustics.

This coupling is possible both at the classical level, where a large number of coherent phonons interact with the quantum system, and at the quantum level, where the quantum system ideally couples to a single phonon. This is of interest not only for quantum physics research, but also for applications ranging from quantum sensing to quantum transduction, where a quantum signal is converted from one type of carrier (e.g. photon) to another (e.g. phonon).

In this thesis we work with surface acoustic waves on GaAs, which is both a piezoelectric material and a semiconductor. In this way, surface acoustic waves can be generated in the same medium that hosts InGaAs quantum dots, which are optically active quantum systems. The coupling between surface acoustic waves and quantum dots can be enhanced by confining the phonons in an acoustic cavity and placing the quantum dot in an optical microcavity to enhance the optical readout. To this end, we describe here the realization of a platform comprising an acoustical cavity and an open-access optical microcavity which, in the near future, will be used for quantum acoustics experiments with gigahertz surface acoustic waves and InGaAs semiconductor quantum dots.

Fabrication of high-finesse surface acoustic wave cavities is not trivial due to a number of loss mechanisms. Because of the system's complexity, finite element simulations are time-consuming and not easy to perform. Therefore, fabrication of high-finesse surface acoustic wave cavities usually involves an optimization process based on iterating sample fabrication and characterization. In our case, we nanofabricate surface acoustic wave cavities via electron beam lithography and evaporation of Al on GaAs. These cavities operate at 1 GHz, and contain an interdigital transducer for surface acoustic wave excitation.

In Chapter 2, focusing on the characterization of surface acoustic wave cavities, we build a fiber-based scanning optical interferometer for measuring the amplitude and phase of the displacement of GHz surface acoustic waves, as well as for imaging their spatial distribution in an acoustic cavity. Characterization of surface acoustic wave cavities is usually done with all-electrical measurements employing the same interdigital transducer used for wave excitation. We find that this method is incomplete and can result in misleading information, especially regarding the distribution of the acoustic field inside the cavity. We show this by imaging transverse modes in a surface acoustic wave cavity

and demonstrating that the superposition of these modes leads to unconventional mode profiles.

One of the loss mechanisms in surface acoustic wave cavities is the scattering of surface waves into bulk waves from the surface acoustic wave mirrors. In Chapter 3 we investigate spurious bulk acoustic waves in surface acoustic wave cavities. This investigation has been possible due to the high spatial resolution of our scanning interferometer, enabling the analysis of the acoustic-wave interference fringes in surface acoustic wave cavities. We also show that amplitude-only measurements of the surface displacement are sufficient to detect bulk waves, due to the interference between surface and bulk waves. This method can be valuable for exploring geometries that minimize bulk wave scattering.

A particular feature of our interferometer is its single-mode fiber splitter. This led to the unexpected observation of the dynamical Talbot effect, where the standing waves in a surface acoustic wave cavity behave as an oscillating diffraction grating. As a result, oscillating replicas of the optical field at the grating are produced at specific locations away from the grating. In Chapter 4 we report the observation and investigation of this phenomenon.

In Chapter 5 we describe the realization of an open-access optical microcavity compatible with a tabletop closed-cycle cryostat. The high mechanical stability of 5.7 pm rms, obtained when the cryostat is operated at 4 K, allows stable operation of a cavity with finesse $F \sim 1800$. In particular, our design has free-space optical access, essential for full polarization control. Tunability and small mode volume makes it compatible with semiconductor quantum dots.

At the time of writing this thesis, the surface acoustic wave cavity is being integrated with the open-access optical microcavity. For this, a GaAs substrate is first coated with an AlAs/GaAs Bragg mirror, and then a layer of InGaAs quantum dots is embedded in the middle of a 260 nm thick GaAs layer. This optically reflective GaAs substrate constitutes the flat mirror of our open-access optical microcavity. The optical microcavity has a mode volume $V \sim 10 \lambda^3$ ($\lambda = 935$ nm) and a finesse $F \sim 1800$, while the surface acoustic wave cavity (the short cavity presented in Chapter 3) has a mode volume $V_{SAW} \sim 3500 \Lambda^3$ ($\Lambda = 2.8 \mu\text{m}$), and finesse $F_{SAW} \sim 40$ at room temperature. With these parameters, the estimated single-phonon displacement is $U_0 \sim 0.01$ fm.

We plan to first study the interaction between surface acoustic waves in the classical regime and a quantum dot, and then explore this interaction with surface waves at the quantum level, ideally with the goal of detecting a single phonon by its modulation of the quantum dot frequency. According to our estimates, single-phonon detection is possible even with our rather large mode volume surface acoustic wave cavity, even though milli-Kelvin temperatures are needed to prepare the acoustic system in the ground state.

Samenvatting

Akoestische oppervlaktegolven golven zijn mechanische golven die beperkt zijn tot het oppervlak van een materiaal. Deze golven komen van nature voor tijdens aardbevingen en zijn ook ontworpen voor gebruik in zeer kleine apparaten, waar ze een cruciale rol spelen bij het detecteren en verwerken van ultrahoogfrequente elektrische signalen. Kunstmatige akoestische oppervlaktegolven opereren doorgaans op frequenties van honderden MHz of hoger, met golflengtes op micrometerschaal en oppervlakteverplaatsingen van honderden picometers - vergelijkbaar met de grootte van een atoom.

De excitatie van deze golven kan worden gedaan via elektromechanische omzetting door een interdigitale transducer op een piëzo-elektrisch materiaal. Akoestische oppervlaktegolven kunnen zeer lage verliezen hebben wat, in combinatie met de mogelijkheid tot koppelen aan een aantal kwantumsystemen via deformatie- of elektrische velden in piëzo-elektrische materialen, recentelijk de verkenning van het veld van kwantumakoestiek mogelijk heeft gemaakt.

Deze koppeling is mogelijk op klassiek niveau, waarbij een groot aantal coherente fononen interacteren met het kwantumsysteem, alswel op kwantumniveau, waarbij het kwantumsysteem idealiter koppelt aan een enkel fonon. Dit is niet alleen van belang voor onderzoek in de kwantumfysica, maar ook voor toepassingen variërend van kwantumdetectie tot kwantumtransductie, waarbij een kwantumsignaal wordt omgezet van het ene type drager (bijv. foton) naar een ander (bijv. fonon).

In dit proefschrift werken we met oppervlakte-akoestische golven op GaAs, dat zowel een piëzo-elektrisch materiaal als een halfgeleider is. Op deze manier kunnen akoestische oppervlaktegolven worden gegenereerd in hetzelfde medium dat de optisch actieve kwantumstippen InGaAs herbergt. De koppeling tussen akoestische oppervlaktegolven en kwantumstippen kan worden versterkt door de fononen op te sluiten in een akoestische trillholte en de kwantumstip in een optische micro-trillholte te plaatsen om de optische uitlezing te verbeteren. Hiertoe beschrijven we hier de realisatie van een platform bestaande uit een akoestische trillholte en een open optische micro-trillholte, dat in de nabije toekomst zal worden gebruikt voor kwantumakoestische experimenten met gigahertz akoestische oppervlaktegolven en InGaAs-halfgeleider-kwantumstippen.

De fabricage van trillholtes voor akoestische oppervlaktegolven met hoge finesse is niet triviaal vanwege de vele verliesmechanismen die aanwezig zijn. Door de complexiteit van het systeem zijn eindige-elementensimulaties tijdrovend en niet eenvoudig uit te voeren. Daarom omvat de fabricage van trillholtes voor akoestische oppervlaktegolven met hoge finesse meestal een optimalisatieproces op basis van het iteratief fabriceren en karakteriseren van samples. In ons geval fabriceren we trillholtes voor akoestische oppervlaktegolven via elektronenbundellithografie en verdamping van Al op GaAs. Deze trillholtes werken op 1 GHz en bevatten een interdigitale transducer voor het exciteren van akoestische oppervlaktegolven.

In Hoofdstuk 2, dat zich richt op de karakterisering van trillholtes voor akoestische oppervlaktegolven, bouwen we een optische interferometer die gebaseerd is op glasvezel om de amplitude en fase van de verplaatsing van GHz akoestische oppervlaktegolven te meten, evenals hun ruimtelijke distributie in een akoestische trillholte in beeld te brengen.

Karakterisering van trilholttes voor akoestische oppervlaktegolven wordt meestal gedaan met volledig elektrische metingen met dezelfde interdigitale transducer die wordt gebruikt voor de excitatie van de golven. We constateren dat deze methode onvolledig is en kan leiden tot misleidende informatie, vooral met betrekking tot de verdeling van het akoestische veld in de trilholtte. We tonen dit aan door transversale modi in een trilholtte voor akoestische oppervlaktegolven in beeld te brengen en te laten zien dat de superpositie van deze modi leidt tot onconventionele profielen.

Een van de verliesmechanismen in trilholttes voor akoestische oppervlaktegolven is de verstrooiing van oppervlaktegolven naar bulkgolven door de spiegels voor akoestische oppervlaktegolven. In Hoofdstuk 3 onderzoeken we ongewenste akoestische bulkgolven in trilholttes voor akoestische oppervlaktegolven. Dit onderzoek is mogelijk geweest dankzij de hoge ruimtelijke resolutie van onze scannende interferometer, waarmee we de interferentiepatronen van akoestische golven in de trilholttes kunnen analyseren. We laten ook zien dat vanwege de interferentie tussen oppervlakte- en bulkgolven, metingen van alleen de amplitude van de oppervlakverplaatsing voldoende zijn om bulkgolven te detecteren. Deze methode kan waardevol zijn bij het onderzoeken van geometrieën die bulk golfverstrooiing minimaliseren.

Een bijzonder kenmerk van onze interferometer is de single-mode glasvezelsplitser. Dit leidde tot de onverwachte observatie van het dynamische Talbot-effect, waarbij de staande golven in trilholttes voor akoestische oppervlaktegolven zich gedragen als een oscillerend diffractierooster. Hierdoor worden oscillerende replica's van het optische veld bij het rooster geproduceerd op specifieke locaties van het rooster. In Hoofdstuk 4 rapporteren we de observatie en het onderzoek van dit fenomeen.

In Hoofdstuk 5 beschrijven we de realisatie van een optische micro-trilholtte met open toegang, compatibel met een gesloten-cyclus cryostaat die op tafel is geplaatst. De hoge mechanische stabiliteit van 5.7 pm rms, verkregen in een cryostaat bij 4 K, maakt stabiele werking van een trilholtte met finesse $F \sim 1800$ mogelijk. In het bijzonder heeft onze opstelling vrije optische toegang, wat essentieel is voor volledige polarisatiecontrole. Verstelbaarheid en een klein modusvolume maken het compatibel met halfgeleiderkwantumstippen.

Op het moment van schrijven van dit proefschrift wordt de trilholtte voor akoestische oppervlaktegolven geïntegreerd met de optische micro-trilholtte met open toegang. Hiervoor wordt een GaAs-substraat eerst gecoat met een AlAs/GaAs Bragg-spiegel, waarna een laag InGaAs-kwantumstippen wordt ingebed in het midden van een 260 nm dikke GaAs-laag. Dit optisch reflectieve GaAs-substraat vormt de vlakke spiegel van onze open optische micro-trilholtte. De optische micro-trilholtte heeft een modevolume $V \sim 10 \lambda^3$ ($\lambda = 935$ nm) en een finesse $F \sim 1800$, terwijl de trilholtte voor akoestische oppervlaktegolven (de korte trilholtte gepresenteerd in Hoofdstuk 3) een modevolume $V_{SAW} \sim 3500 \Lambda^3$ ($\Lambda = 2.8 \mu\text{m}$) heeft, en finesse $F_{SAW} \sim 40$ bij kamertemperatuur. Met deze parameters is de geschatte verplaatsing van een enkel fonon $U_0 \sim 0.01$ fm.

We zijn van plan om eerst de interactie tussen akoestische oppervlaktegolven en een kwantumstip in het klassieke regime te bestuderen, en vervolgens deze interactie te onderzoeken met oppervlaktegolven op kwantumniveau, idealiter met als doel een enkel fonon te detecteren door de modulatie van de frequentie van de kwantumstip te meten. Volgens onze schattingen is de detectie van een enkel fonon mogelijk, zelfs met onze trilholttes voor akoestische oppervlaktegolven die een relatief grote modevolume hebben, alhoewel daarvoor millikelvin-temperaturen nodig zijn om het akoestische systeem in de grondtoestand te brengen.

Curriculum Vitae

Matteo Fisicaro

31-07-1994 Born in Villafranca di Verona (VR), Italy.

Education

- 2008-2013 Scientific high school
Liceo scientifico Belfiore, Mantova, Italy
- 2013-2016 BSc Physics
University of Trento
- 2017-2019 MSc Physics of matter,
University of Padova
- 2019-2024 PhD Physics
Universiteit Leiden

List of publications

1. V. Fedoseev, **M. Funicaro**, H. van der Meer, W. Löffler, and D. Bouwmeester, Realignment-free cryogenic macroscopic optical cavity coupled to an optical fiber, *Review of Scientific Instruments* 93, 013103 (2022).
2. **M. Funicaro**, M. Witlox, H. van der Meer, and W. Löffler, Active stabilization of an open-access optical microcavity for low-noise operation in a standard closed-cycle cryostat, *Review of Scientific Instruments* 95, 033101 (2024).
3. **M. Funicaro**, T. A. Steenbergen, Y. C. Doedes, K. Heck, and W. Löffler, Imaging Transverse Modes in a GHz Surface Acoustic Wave Cavity, submitted, arXiv:2408.11630.
4. **M. Funicaro**, Y. C. Doedes, T. A. Steenbergen, M. P. van Exter, and W. Löffler, Observation of the Talbot Effect from a Surface Acoustic Wave Dynamic Grating, submitted, arXiv:2409.11161.
5. **M. Funicaro**, T. A. Steenbergen, Y. C. Doedes and W. Löffler, Investigation of spurious bulk acoustic waves in surface acoustic wave devices by acoustic fringe analysis, to be submitted.

Acknowledgements

During my 5 years of PhD, I have had the pleasure to encounter and work with many people. Without your support, this thesis wouldn't have been possible. **Wolfgang**, thank you for giving me the honour of being one of your first PhD students and for teaching me how to be a scientist. Your excitement and enthusiasm about physics have been a great inspiration to me, while your commitment and care as a leader have contributed to creating a very nice and familiar atmosphere in the group. **Dirk** and **Vitaly**, thank you for leading me to Leiden by accepting me for a master's thesis project. In particular, thank you, Vitaly, for teaching me invaluable optics lab skills that I used throughout my whole PhD. **Petr** and **Kirsten**, you have always been present during my PhD. Thank you for sharing with me all the ups and downs of it, for the many scientific discussions, and the non-scientific conversations. You have been great friends and colleagues. **Renze**, it has been a pleasure supervising your bachelor project. Thank you for your enthusiasm, curiosity, and motivation. Despite the pandemic forcing us to opt for a side project, you managed it successfully. Your simulations on surface acoustic waves have provided valuable insight for my research. **Thomas** and **Yasmin**, many of the results in this thesis wouldn't have been possible without you. I had lots of fun working side by side with you during your master projects, teaching you, and learning from you. Thank you for all of this and, most importantly, thank you for rekindling my interest and passion for research after a challenging project and part of my PhD. My research wouldn't have been possible without the help from the electronics and fine mechanical departments. In particular, I would like to thank **Harmen**, **Martijn**, **Gijsbert**, **Emiel**, and **Harry**. **Luc**, thank you for your support and help regarding nanofabrication.

To all the present and past members of the Quantum Optics group, thank you for all the lunches, coffees, and fun times spent together. In particular, **Corné**, **Xing**, **Mio**, **Tom**, **Leon**, **Xinrui**, **Jacopo**, **Erik**, **Jonah**, and **Felix**, with whom I could always have useful scientific discussions, as well as share a joke or two. Mio, thank you also for your help with the design of my thesis cover. **Martin** and **Michiel**, thank you for the scientific discussions and for teaching me many optics-related things. **Henriette**, thank you for dealing with all the administrative things. **Kier**, thank you for teaching me countless interesting things about electronics and signal processing, as well as many research-unrelated things. I enjoyed our conversations during coffee breaks very much. **Godwill**, thank you for keeping our workplace clean and for welcoming me every day with a big and contagious smile.

My PhD journey was full of challenging moments, and I couldn't have made it without the support and encouragement of many friends. Hereby, I would like to thank you all, and in particular, **Luca**, **Melissa**, **Leonardo**, **Claudia**, and **Laura**.

Finally, I would like to thank the people who encouraged and inspired me to pursue a scientific career. In particular, my parents, **Antonella** and **Antonino**, for instilling in me a curiosity and passion for experiments from a young age, as well as for their unwavering support. My secondary-school science teacher, **Angela**, for fostering my curiosity and sense of wonder towards nature. And my high-school physics teacher **Claudio**, for passing on to me a love for physics.

